Direct numerical simulation of turbulent channel flow with condensation

Dissertation

zur Erlangung des akademischen Grades

Doktoringenieur
(Dr.-Ing.)

vorgelegt der
Fakultät für Maschinenbau
der Technischen Universität Ilmenau

von Herrn

Philipp Bahavar, M. Sc.
geboren am 20.12.1990
in Bad Nauheim

1. Gutachter: Prof. Dr.-Ing. habil. Claus Wagner
2. Gutachter: Prof. Dr. rer. nat. habil. Jörg Schumacher
3. Gutachter: Dr.-Ing. Thomas Hüttl

Tag der Einreichung: 14.10.2022
Tag der wissenschaftlichen Aussprache: 27.04.2023

DOI: 10.22032/dbt.57712
URN: urn:nbn:de:gbv:ilm1-2023000183

This work is licensed under a Creative Commons
Attribution-ShareAlike 4.0 International License

Philipp Bahavar

DNS of turbulent channel flow with condensation

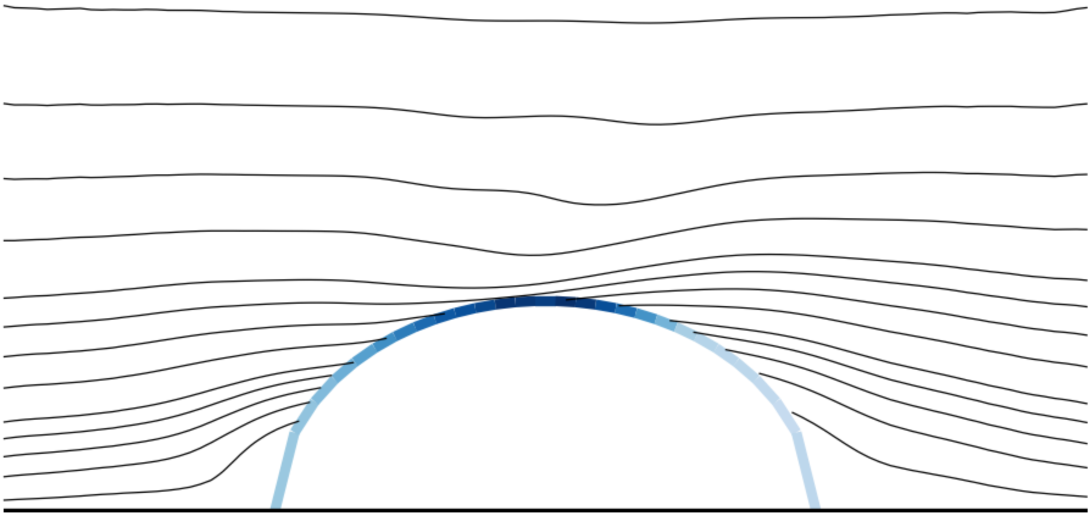

Acknowledgements

No one has played a greater role in making this work possible than my daily companions, Miriam and Yuri. I hope to thank you every day in turn.

I wrote this dissertation based on my research at the DLR Institute of Aerodynamics and Flow Technology in Göttingen. Here, Claus Wagner took on the role of my advisor and helped me with his experience and expertise at countless points along the way. Thank you for the support and opportunities.

Each one of my colleagues in the department, past and present, made my work easier or more pleasant at one point or another. I want to thank all of you for the great working environment.

I will specifically mention Christian Brückner and Michael Mommert, who I could always count on for help, distraction, and lunch. Thank you for all the good times, at work and otherwise.

As part of the examining committee, I would like to thank Professor Schumacher and Dr. Hüttl for their thorough review of this thesis and the engaging discussion during the defense, Professor Witte and Professor Bergmann for the fascinating insights into their fields, and Professor Zentner for chairing the proceedings.

While writing this thesis, I drew frequent inspiration from the works of Edward Tufte and Jean-luc Doumont. I recommend their books to anyone curious about the effective communication of ideas and relationships in text and graphics.

Abstract

This thesis presents direct numerical simulations of turbulent humid air flow through a cooled vertical channel at atmospheric conditions.

The combination of humidity, temperature and mixed convection is relevant to the ventilation of car interiors, where condensation on critical surfaces such as windows and windshield poses a problem to its immediate or long-term usability.

The interaction between buoyancy, convective transport, and phase transitions creates a complex multi-physics problem at the intersection of thermodynamics and fluid dynamics.

For the specific range of flow parameters relevant to automotive ventilation, the influence of the liquid phase dynamics is negligible compared to the flow of the gas phase. Leveraging this fact, the single-phase simulation approach uses direct numerical simulations for the solution of the flow fields for the gas phase, including the effect of the phase transition on the velocity, temperature, and vapor concentration of the humid air. It disregards the dynamics within the liquid phase, either neglecting the liquid completely or modeling condensate droplets as static, solid wall deformations.

Simulations with and without phase transitions and with and without wall deformations serve to isolate the specific effect of the different influence factors.

The combination of direct buoyancy from the cooling and drying of the humid air near the cooled channel wall and the opposing buoyancy contribution from the released latent heat damps the overall influence of the cooled surface on the flow fields compared to cooled channel flow without condensation.

In simulations including wall deformations mimicking condensate droplets, the flow across these obstacles create a positive feed-back loop for condensation, increasing the rates at existing droplets.

Zusammenfassung

Diese Arbeit präsentiert direkte numerische Simulationen von turbulenter Strömung feuchter Luft durch einen gekühlte, vertikalen Kanal.

Die Kombination von Feuchtigkeit, Temperatur und Mischkonvektion tritt in der Belüftung von Fahrgasträumen auf. In dieser Anwendung stellt unerwünschte Kondensation an kühlen Oberflächen wie Fenstern und Windschutzscheibe ein Problem dar, das die Nutzung des Fahrzeugs kurz- oder langfristig beeinträchtigt.

Die Wechselwirkung zwischen Auftrieb, Konvektion und Phasenübergängen berührt gleichermaßen die Thermodynamik und die Fluidmechanik.

Für die Rahmenbedingungen, die für die Belüftung in Automobilen relevant sind, kann die Strömung von flüssigem Wasser vernachlässigt werden. Die direkte numerische Simulation betrachtet deshalb nur die Gasphase und modelliert den Einfluss des Phasenübergangs nur im Hinblick auf die feuchte Luft. Flüssiges Wasser wird entweder komplett vernachlässigt oder als Kondensattropfen nachempfundene Wandverformung behandelt.

Mithilfe von Simulationen mit und ohne Phasenübergang und mit und ohne Wandverformung wird der Einfluss der unterschiedlichen Faktoren voneinander getrennt untersucht.

Die entgegengesetzte Wirkung von Auftrieb, der direkt aus dem Abkühlen und Trocknen der feuchten Luft an der Wand resultiert, und dem Auftrieb, der durch die freiwerdende Kondensationswärme zustande kommt, dämpft den Einfluss der gekühlten Wand auf die Strömung im Vergleich zu gekühlter Kanalströmung ohne Kondensation.

In den Simulationen mit Wandverformung durch angelagertes Kondensat verursachen diese Verformungen einen positiven Feedback-Loop, der die Kondensationsraten an der Oberfläche von bereits existierenden Tropfen verstärkt.

Contents

1 *Condensation at atmospheric conditions* 17
  The thermodynamics of humid air 18
  Objectives and organization 23

2 *Turbulence and direct numerical simulation* 27
  Transport in fluid flows 28
  Turbulent flow 34
  Direct numerical simulation 39

3 *Active scalar phase change modeling* 49
  Single-phase formulation of phase transition 50
  Implementation in OpenFOAM 54
  Validation 62
  Summary and perspective 68

4 *Interactions between turbulence and condensation* 71
  Channel flow in an inlet–outlet configuration 72
  Turbulent transport and condensation 78
  Conclusions 100

5 *Implications for condensation predictions* 103
  Application of the active scalar model 104
  Interactions between condensation and turbulence 106
  Condensation control 115

List of Publications

The following peer-reviewed publications, co-authored with Claus Wagner, are connected to the research and results presented in this thesis:

2017	Direct numerical simulation of convective channel flow with temperature and concentration gradients, *Notes on Numerical Fluid Mechanics and Multidisciplinary Design,* Vol. 36 doi: 10.1007/978-3-319-64519-3_40
2019	Direct numerical simulation of convective turbulent channel flow of fluid mixtures, *Direct and Large Eddy Simulations XI ERCOFTAC Series*, Vol. 25, doi: 10.1007/978-3-030-04915-7_38
2020	Condensation-induced flow structure modifications in turbulent channel flow investigated in direct numerical simulations, *Physics of Fluids*, Vol. 32, No. 1, doi: 10.1063/1.5128976
2020	Direct numerical simulation of turbulent channel flow with condensation using a cluster-based droplet deposition model, *Direct and Large Eddy Simulations XII ERCOFTAC Series*, Vol. 27, doi: 10.1007/978-3-030-42822-8_15
2022	Sessile condensate droplets as quasi-static wall deformations in direct numerical simulations of channel flow with condensation, *in preparation,* doi: 10.48550/arXiv.2206.13890

List of Figures

1.1 The phase diagram of water 18
1.2 The saturation curve for water vapor in air 19
1.3 Schlieren image of natural convection above a candle flame 20
1.4 Hydrophilic, hydrophobic, and superhydrophobic droplets 22

2.1 Velocity fluctuations in isothermal channel flow 38
2.2 Schematic overview of a control volume in the finite volume method 43

3.1 Schematic overview of the leapfrog time stepping 57
3.2 Phase space trajectory during condensation 59
3.3 The grid-based droplet distribution algorithm 61
3.4 Setup for differentially heated vertical channel flow 63
3.5 Velocity and temperature profiles in differentially heated vertical channel flow 64
3.6 Velocity and temperature fluctuations in differentially heated vertical channel flow 64
3.7 Setup for cyclic channel flow with evaporation and condensation 65
3.8 Temperature profiles for cyclic channel flow with condensation and evaporation 66

4.1 Instantaneous vapor concentration in turbulent channel flow 72
4.2 Setup for condensation in an inlet-outlet channel 72
4.3 Coupled setup of the precursor simulation and the investigation domain 74
4.4 Distribution of droplet radii and heights 76
4.5 The Wendland function W2 77
4.6 Streamwise evolution of mean temperature and concentration 78
4.7 Streamwise evolution and transfer rate of total heat flux 80

4.8 Instantaneous condensation rates at the cooled wall 81
4.9 Instantaneous friction velocity at the cooled wall 81
4.10 One-point cross-correlation of condensation rate and friction velocity 82
4.11 Cross-correlation of the spanwise variation of the condensation rate and friction velocity 83
4.12 Condensate accumulation at the cooled wall 83
4.13 Pattern of 1900 condensate droplets 84
4.14 Comparison of mean condensation rates with and without droplets 84
4.15 Voronoi decomposition of the wall surface 85
4.16 Polar coordinate system for droplet ensemble averaging 86
4.17 Ensemble-averaged condensation rates with and without droplets 86
4.18 Ensemble-averaged condensation rates at the droplet surface 87
4.19 Droplet coordinate system 87
4.20 Upstream and downstream velocity profiles at the droplet edges 88
4.21 Ensemble-averaged velocity field in the immediate vicinity of droplets 89
4.22 Ensemble-averaged temperature and vapor concentration in the immediate vicinity of droplets 89
4.23 Growth of the thermal boundary layer with and without condensation 90
4.24 Growth of the thermal boundary layer with and without droplets 90
4.25 Velocity profiles for channel flow with and without condensation and with and without droplets 91
4.26 Profiles of the velocity fluctuations for channel flow with and without condensation and with and without droplets 92
4.27 Velocity fluctuations in periodic channel flow with aiding and opposing buoyancy 93
4.28 Ensemble-averaged velocity fluctuations in the immediate vicinity of droplets 94
4.29 Thermal boundary layer growth, conditionally sampled for sweeps and ejections 94
4.30 Concentration boundary layer growth, conditionally sampled for sweeps and ejections 95
4.31 Conditionally sampled velocity profiles, pre- and post-interaction 97
4.32 Conditionally sampled velocity profiles with droplets, pre- and post-interaction 98

4.33 Pre-multiplied energy spectra for pre- and post-interaction fluid with and without condensation 99

5.1 Modification of post-interaction flow structures by the active scalar model 104
5.2 Discrepancies between active scalar condensation and multi-phase DNS 105
5.3 Temperature in laminar and turbulent channel flow 107
5.4 Instantaneous condensation rates at the cooled wall 108
5.5 Correlation between friction velocity and condensation rate 108
5.6 Richardson-dependence of the mean velocity and fluctuations in aiding/opposing flow. 109
5.7 Difference in mean velocity and fluctuations between nPT and PT 110
5.8 Theoretical and simulated droplet size distributions 112
5.9 The velocity shift due to surface roughness 112
5.10 The concentration gradients around condensate droplets 113

1

Condensation at atmospheric conditions

At any given moment, our atmosphere contains $1.4 \cdot 10^{16}$ kg water vapor, equivalent to an average density of $2.33\,\mathrm{g/m^3}$.[1]

This water flows between liquid reservoirs on the ground, rises as vapor from near the surface to high above, moves with the wind, and then returns to a liquid, first in the clouds and then as rain to the ground. The water cycle illustrates all the phenomena and transport mechanisms that apply to humid air in general: *evaporation, natural* and *forced convection*, and *condensation*.

The permanent presence of water vapor in the air means these processes are a feature of everyday life. Fogging windshields, droplets on beverages,[2] the vapor cloud from exhaling on a cold day, or the streets drying after a summer rain — all these are examples of the interaction between evaporation or condensation and the surrounding air.

The focus of this chapter lies on the thermodynamics of water and its transport across the liquid–vapor phase boundary.

[1] Chahine, *The hydrological cycle and its influence on climate*, 1992.

[2] Jorge et al., *Heat and mass transfer during the warming of a bottle of beer*, 2010.

The thermodynamics of humid air

A *phase transition* is the change of a substance from one thermodynamic state to another — such as the transition from liquid water to vapor and vice versa. The thermodynamic state describes an equilibrium of the internal parameters: temperature, pressure, and chemical potential.[3]

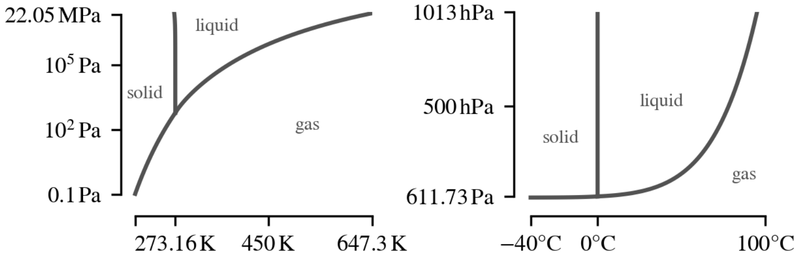

Figure 1.1: Temperature and pressure determine the state of water. Note the logarithmic pressure scale for the overview on the left, compared to the detailed view at atmospheric conditions on the right.

In a system consisting only of a constant amount of pure water, temperature and pressure uniquely determine its phase state. The *phase diagram* in figure 1.1 shows the state of water at a given temperature and pressure. The right panel focusses on conditions that might be encountered in nature, while the left panel gives an overview of a much larger range of temperatures and pressures.

Along the coexistence lines, both adjacent states exist. At the *triple point*, at 273.16 K and 611.73 Pa, solid, liquid, and gaseous water are in equilibrium. The endpoint of the liquid–solid coexistence curve is the *critical point* at 647.3 K and 22.05 MPa. Here, the difference between vapor and liquid disappears. Both phases have equal density with no distinct transition between them.

The *Clapeyron equation*[4] gives the slope of the coexistence curves

$$\frac{\mathrm{d}p}{\mathrm{d}T} = \frac{h}{T\Delta v}. \tag{1.1}$$

Here, Δv is the discontinuity of the molar volume between the two phases and h is the *latent heat* of the transition.

The latent heat is the amount of energy required to overcome the attractive intermolecular forces of one state of matter to transition to a more loosely bound state. For the solid–liquid transition, h_m is the *latent heat of melting*, and for the liquid–gas transition, h_v is the *latent heat of vaporization* or *vaporization enthalpy*. During condensation, the process is reversed. The matter transitions to a more tightly bound state and the binding energy in form of the latent heat of vaporization is released again as sensible heat.

[3] Callen, *Thermodynamics and an introduction to thermostatistics*, 1985, p. 133.

[4] Callen, *Thermodynamics and an introduction to thermostatistics*, 1985, p. 230.

Latent heat inseparably links the transfer of mass across the phase boundary to an associated energy transfer between sensible and latent heat. Considering again the global water cycle, 38 mg of water transition to vapor each second over every square meter of the oceans. With $h_v = 2454\,\mathrm{kJ/kg}$,[5] the accompanying energy flux is $93\,\mathrm{W/m^2}$.[6] Compared to the global horizontal irradiance of $1120\,\mathrm{W/m^2}$,[7] latent heat is a significant part of the energy balance at the surface of the planet.

When discussing evaporation of water in the presence of air, the interpretation of the coexistence curves changes slightly. For humid air, they now represent the maximum partial pressure of water vapor in the gas mixture. This pressure is the *saturation pressure* for a given temperature. If the system contains liquid water and dry air, water will evaporate until the mixture is saturated. At this point, the gas phase of the water is in equilibrium with the liquid phase. Conversely, *oversaturation* will result in condensation to restore the equilibrium.

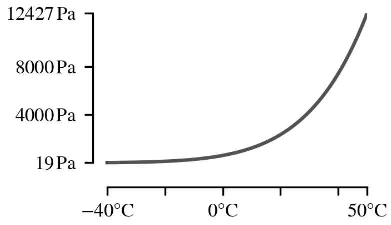

Figure 1.2: Warm air can hold more vapor than cold air, since the saturation pressure increases exponentially with the temperature.

Due to the relevance to meteorology and climatology, specific approximations to the solution of the Clapeyron equation (1.1) exist for the saturation pressure of water in humid air. Over a temperature range from $-40\,^\circ\mathrm{C}$ to $50\,^\circ\mathrm{C}$, the most accurate expression is[8]

$$p_{sat}(p,T) = 1.00071 \exp\left(4.5 \cdot 10^{-8} p\right) \cdot 610.94\,\mathrm{Pa} \exp\left(\frac{17.625T}{243.04+T}\right), \tag{1.2}$$

with the temperature in degrees Celsius and a correction factor accounting for the overall barometric pressure p. Figure 1.2 shows the exponential dependence of the saturation pressure on air temperature at $p = 101325\,\mathrm{Pa}$, as given by equation (1.2).

Absolute humidity is the vapor content of humid air given by the partial pressure of the vapor. An equivalent quantity is the *dew point*, which is defined as the temperature at which the given vapor pressure would be equal to the saturation pressure. *Relative humidity* is then the ratio between the absolute humidity and the saturation pressure at the given temperature.

[5] Engineering ToolBox, *Water - Heat of Vaporization.* 2010.

[6] Charette and W. Smith, *The Volume of Earth's Ocean*, 2010.

[7] Newport Corporation, *Introduction to Solar Radiation*, 2020.

[8] Alduchov and Eskridge, *Improved Magnus Form Approximation of Saturation Vapor Pressure*, 1996.

Natural convection

Humidity differences cause density differences in humid air. Since the molecular weight of pure vapor, $M_{H_2O} \simeq 18\,\mathrm{g/mol}$ is lower than that of air at $M_{air} \simeq 29\,\mathrm{g/mol}$, the combined density of the mixture becomes less dense with increasing vapor content.

A packet of humid air with density ρ_h will rise through surrounding dry air with density ρ driven by a buoyancy force per unit volume of

$$f_b = -\left(\rho - \rho_h\right) g, \tag{1.3}$$

as dictated by Archimedes' principle.

Movement resulting from forces originating from within the air itself is *natural* or *free convection.*

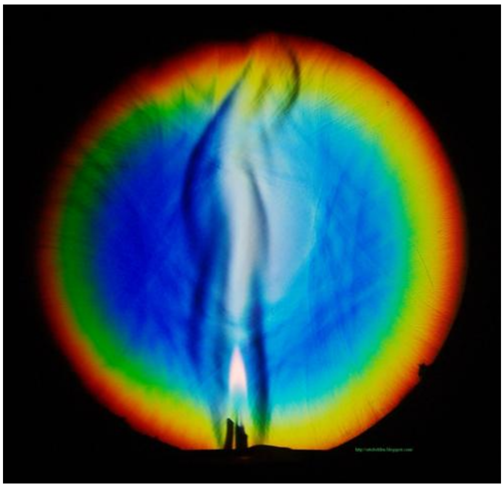

Figure 1.3: Schlieren imaging reveals the natural convection of hot air above a candle flame
Belden, *Schlieren Photo of a Candle Burning*, 2010

Next to temperature, humidity is one of the main driving forces for natural convection in the atmosphere. Concerning evaporation, both contributions work in tandem. Increased temperature lowers the density of the gas and favors evaporation, which then increases the humidity.

Natural convection transports water vapor from surface evaporation up into the atmosphere. There, *forced convection* by the wind redistributes the humid air across the globe. Chapter 2 will discuss both types of convective transport of humidity in more detail.

Vapor then condenses into clouds and the water returns to the surface as rain, snow, hail, or similar forms of precipitation. Over land and sea surfaces combined, $5 \cdot 10^{17}$ kg of water go through the complete water cycle every year.

Evaporation and condensation are both the cause and the result of the large amount of water in the atmosphere. The permanent presence of humidity in the air means that depending on the temperature and the pressure, the investigation of air flow might need to consider phase transitions to obtain a complete picture of the flow.

Passenger ventilation

One application where condensation and evaporation play an important role is the ventilation of occupied spaces inside vehicles.

The air inside of a car, a train compartment, an aircraft cabin or similar contains water vapor. For a non-sealed space, the connection to the humid atmosphere outside is the obvious vapor source. Additionally, the respiration of the occupants releases humidity into the air.

Independent of temperature and humidity of inhaled air, exhaled air is slightly below body temperature and is close to saturated with vapor, with a relative humidity of $> 90\,\%$.[9] At an interior temperature of $21\,^{\circ}\mathrm{C}$, a resting person adds $10.62\,\mathrm{g/h}$ of vapor to the air.[10]

Condensation at the walls or windows of the passenger compartment becomes possible due to the potentially large temperature difference between the comfortably heated interior and a cold exterior, as experienced by a car in winter or by a plane at cruising altitude. With limited thermal isolation of the exterior walls, the temperature of an interior surface can drop below the dew point. At this point, vapor condenses on the surface in question.

Depending on the specific location and the amount of condensation, this presents a problem to the continued use of the compartment. In airplanes, condensation in the space between the interior cabin panels and the exterior hull of the aircraft leads to the accumulation of water inside the thermal isolation, causing mold and increasing the weight of the airframe over its lifetime.[11] In a car, fogging of the windshield inhibits the vision of the driver and is a safety concern. For electric cars, the energy required to defog the windshield directly impacts the range of the vehicle.[12]

Especially in view of energy efficiency, preventing condensation at critical locations is preferable to removing the condensate by heating or other means. However, it is impossible to remove the potential for condensation. Both temperature and humidity inside the vehicle are important comfort parameters. The connection between respiration and humidity causes increased dehydration when the surrounding air is very dry, leading to an uncomfortable, dry sensation when breathing.[13] A relative humidity between 30 % and 65 % is recommended for continuously occupied spaces.[14]

---

[9] Ferrus et al., *Respiratory water loss as a function of ventilatory or environmental factors*, 1984.

[10] Zuurbier et al., *Minute ventilation of cyclists, car and bus passengers: an experimental study*, 2009.

[11] Zhang Tengfei et al., *Insulation of commercial aircraft with an air stream barrier along fuselage*, 2012.

[12] Lorenz, *Reduction of heating loads and interior window fogging in vehicles*, 2015.

Likewise, comfort requirements constrain the possible interior temperature, while the temperature outside changes with the weather or overall seasons such that large temperature differences can be unavoidable.

In light of this, one possible solution to limit condensation in a specific area is the modification of the surface in question. Chemical coatings or nano-structuring create a *superhydrophobic* surface, inhibiting the formation and accumulation of condensate.[15] However, such special preparation of the surface is expensive and subject to degradation over time.

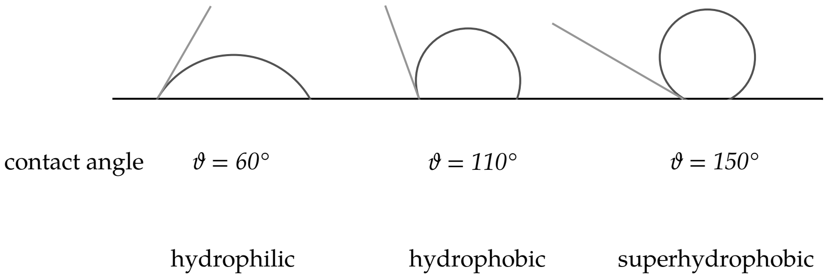

Figure 1.4: A contact angle of 90° marks the limit between hydrophilic and hydrophobic surfaces. Above 150°, the surface is superhydrophobic.
Wang Shutao and Lei Jiang, *Definition of Superhydrophobic States*, 2007

A different approach arises from considering condensation inside passenger compartments from the perspective of fluid dynamics over taking a purely thermodynamic view.

Heating elements and body heat cause thermal convection with air rising towards the ceiling, while next to cooled surfaces, the increased density of the cold air creates a downdraft. The active ventilation systems of the passenger compartment introduce a controllable element of forced convection. Both natural and forced convection, combined into *mixed convection*, alongside with diffusion through the air, continuously re-distribute heat and humidity throughout the interior volume.

Understanding the interplay between flow, transport, and phase transition is the first step to create flow conditions that discourage condensation on critical surfaces.

[13] Reinikainen et al., *The effect of air humidification on different symptoms in office workers — An epidemiologic study*, 1991.

[14] *DIN EN 1946-2:1999-04, Wärmetechnisches Verhalten von Bauprodukten und Bauteilen*, 1999.

[15] Oberli et al., *Condensation and freezing of droplets on superhydrophobic surfaces*, 2014.

Objectives and organization

This thesis presents a numerical investigation of the interplay between condensation and turbulent flow.

The investigation setup encompasses similar thermodynamic conditions as found in interior ventilation. The working fluid is humid air at ambient conditions. Standard pressure is 101325 Pa, and temperatures are between 0 °C and 30 °C, biased towards a central European climate. Consequently, the temperature differences considered are of the order 10 K – 30 K. This limits the difference between minimum temperature and the dew point, the *subcooling,* to a similar range.

The flow contains contributions from forced and natural convection, where both temperature and humidity contribute to the buoyancy.

While these general conditions mirror those found inside a car, the investigation geometry is far from an interior car geometry. Here, a generic channel geometry provides insights on the fundamental interaction between flow and phase transition, without confounding factors from the specific layouts or ventilation concepts.

The specific objectives of this thesis are:

- Creating an efficient and versatile approach to include phase transitions on top of a high-precision flow simulation,
- Identifying the leading transport mechanisms driving condensation on a cooled surface,
- Analyzing the effect of condensation on the overall flow,

and finally,

- Investigating positive and negative feed-back between flow and condensation.

Chapter 2 provides the fundamental fluid dynamics for flow setups of this kind. Informed by the limits on the thermodynamic and fluid dynamic parameters outlined above, it introduces the appropriate formulation of the Navier–Stokes equation and for the transport equations in general.

The chapter continues to discuss turbulence in a general sense, establishing a baseline for the flow phenomena that are subject to change under the influence of phase transitions.

Based on this understanding of the underlying dynamics and the resulting flow structures, direct numerical simulation is introduced as the research tool used for the numerical investigation.

Building on this, chapter 3 outlines the specific implementation of the numerical simulation in OpenFOAM and formulates the active scalar phase-change model. This model utilizes the specific range of flow and thermodynamic parameters to create a simple but powerful approach to investigate the interaction between turbulence and condensation.

Chapter 4 then presents the results obtained from numerical simulations using the active scalar approach. The discussion centers on the coupling between fluid flow, buoyancy, and humidity. It shows how the release of latent heat during condensation damps effects associated with cooled flow without condensation. The analysis of the flow in the vicinity of condensate droplets reveals advantageous conditions for further condensation at the droplet surface.

Finally, chapter 5 calls back to the objectives formulated above. It discusses and evaluates the results of the investigation as they relate to these overall goals.

2

Turbulence and direct numerical simulation

Condensation in humid air is a fluid dynamics problem on top of being a thermodynamic problem.

The previous chapter discussed the thermodynamic properties of humid air at ambient conditions, as well as the prerequisites for condensation. Now, the focus shifts to the transport of the thermodynamic variables by the flow and features of the flow itself, including both the governing equations as well as the resulting flow phenomena.

The formulation of the governing equations in both dimensional and dimensionless form shows the concurrent transport mechanisms and the balance between them. The characteristic numbers resulting from the dimensionless formulation allow the discussion of turbulence in general, independent of a specific flow configuration.

The flow features identified in this general case inform requirements for the numerical methods to simulate turbulent flow. In direct numerical simulations, this leads to unavoidable high computational costs, for the benefit of fully resolved results that are free from model assumptions and therefore uniquely suited for research purposes.

A short overview of the possible implementations of such simulations, as well as the various ways to treat multi-phase flows, leads directly to the next chapter, which introduces the specific simulation methods for this work.

Transport in fluid flows

Convective flows play a large role in the transport of water vapor in humid air. At the largest scales as part of the atmospheric water cycle, or on smaller scales inside an air-conditioned train compartment, the movement of the air itself carries the humidity along.

Interactions with external boundaries and within the fluid itself determine the behavior of the flow. The mathematical formulation of these interactions yield the system of equations that govern the dynamics of the flow.

Starting from isothermal flow and the transport of momentum, the complexity of the problem increases as additional forces act on the fluid. Temperature differences and fluids comprised of different components necessitate equations describing the transport of heat and of the individual species, which are coupled to the momentum equation to include effects such as natural convection from thermal buoyancy.

Counteracting this increasing complexity are approximations reflecting the specific flow situation of interest. Assuming for example constant density or small temperature differences results in simplified expressions for the dynamics.

Finally, the dimensionless groups arising from these governing equations define the characteristic dimensionless numbers for the given flow configuration. They generalize the results obtained for a specific setup to flows at different scales, identified as similar by the dimensionless numbers.

Transport equations

The governing equations of fluid dynamics describe the evolution of the flow variables through space and time. At their core, they contain the conservation laws for mass, energy, and momentum in a closed system.

Conservation of mass leads to the *continuity equation*.[1] The flow of a fluid with density ρ can transport mass into and out of an arbitrary volume element. The mass flux through a surface ΔA of this volume is $\rho u_{\perp} \Delta A$, with $u_{\perp}$ the component of the flow velocity perpendicular to the surface.

[1] Bird et al., *Introductory Transport Phenomena*, 2014, p. 83.

Summing these flux contributions over the complete closed surface of the volume element and dividing by the volume then gives the change in density in the form of the continuity equation,

$$\frac{\partial \rho}{\partial t} = -\nabla \cdot (\rho \boldsymbol{u}). \tag{2.1}$$

Already at this point, certain flows allow a fundamental simplification. For liquids and for gases flowing much slower than their speed of sound, the density is approximately constant. For such *incompressible* flows, the continuity equation becomes

$$\nabla \cdot \boldsymbol{u} = 0. \tag{2.2}$$

Analogous to the mass flux, a momentum flux ϕ_i transports the i component of momentum $u_i \cdot m$ into and out of a volume element. Again, summing the flux contributions over the surface gives the net change of the component of momentum. Summing all spatial components yields[2]

$$\frac{\partial}{\partial t}(\rho \boldsymbol{u}) = -\nabla \cdot \underline{\underline{\boldsymbol{\Phi}}}, \tag{2.3}$$

with $\underline{\underline{\boldsymbol{\Phi}}}$ a second-order tensor for the momentum flux.

The momentum flux tensor collects the different mechanisms for momentum transport. The first contribution is the convective transport of momentum with the flow. Multiplying the momentum per unit volume by the volume flow rate gives the convective momentum flux tensor,

$$\underline{\underline{\pi}} = \rho \boldsymbol{u}\boldsymbol{u}. \tag{2.4}$$

A second source of momentum flux are the molecular interactions within the fluid. As one fluid element flows past another with some relative velocity, the *dynamic viscosity* μ of the fluid transfers momentum along the direction perpendicular to the relative flow vector. The entries of this *shear stress* tensor[3] are

$$\tau_{ij} = -\mu \left(\frac{\partial u_i}{\partial x_j} + \frac{\partial u_j}{\partial x_i} \right), \quad i \neq j, \tag{2.5}$$

$$\tau_{ii} = -2\mu \frac{\partial u_i}{\partial x_i} + \left(\frac{2}{3}\mu - \mu_\mathrm{b} \right) \left(\frac{\partial u_i}{\partial x_i} + \frac{\partial u_j}{\partial x_j} + \frac{\partial u_k}{\partial x_k} \right). \tag{2.6}$$

The *bulk viscosity* μ_b of the fluid quantifies the friction while experiencing expansion or compression.

[2] Bird et al., *Introductory Transport Phenomena*, 2014, p. 86.

[3] Bird et al., *Introductory Transport Phenomena*, 2014, p. 22.

Combining the convective and the molecular momentum flux and expressing the pressure contribution using the unit tensor $\underline{\underline{\delta}}$ yields the total momentum flux tensor,

$$\underline{\underline{\boldsymbol{\Phi}}} = \underline{\underline{\boldsymbol{\pi}}} + p\underline{\underline{\delta}} + \underline{\underline{\boldsymbol{\tau}}}. \tag{2.7}$$

Substituting this expression in the equation for the momentum change (2.3) and allowing an external force $\boldsymbol{f}$ to act on the fluid gives

$$\frac{\partial}{\partial t}(\rho \boldsymbol{u}) = -(\nabla \cdot \rho \boldsymbol{u}\boldsymbol{u}) - (\nabla \cdot \underline{\underline{\boldsymbol{\tau}}}) - \nabla p + \rho \boldsymbol{f}. \tag{2.8}$$

Restricting the application to incompressible flows again simplifies the governing equation. Since the velocity is divergence-free, the terms containing the bulk viscosity vanish from the diagonal elements of the shear stress tensor (2.6). Further assuming a *Newtonian fluid* where μ is constant allows

$$\begin{aligned}\left(\nabla \cdot \underline{\underline{\boldsymbol{\tau}}}\right)_i &= -\mu \frac{\partial}{\partial x_i}\left(\frac{\partial u_i}{\partial x_i} + \frac{\partial u_j}{\partial x_j} + \frac{\partial u_k}{\partial x_k}\right) - \mu\left(\frac{\partial^2 u_i}{\partial x_i^2} + \frac{\partial^2 u_j}{\partial x_j^2} + \frac{\partial^2 u_k}{\partial x_k^2}\right) \\ &= \left(-\mu \nabla^2 \boldsymbol{u}\right)_i \end{aligned} \tag{2.9}$$

by applying the continuity equation to the first term.

Using the *kinematic viscosity* $\nu = \mu/\rho$, the momentum equation is the *Navier–Stokes* equation:[4]

$$\frac{\partial \boldsymbol{u}}{\partial t} + (\boldsymbol{u} \cdot \nabla)\boldsymbol{u} = -\frac{1}{\rho}\nabla p + \nu \nabla^2 \boldsymbol{u} + \boldsymbol{f}. \tag{2.10}$$

The set formed by the continuity equation (2.2) and the Navier–Stokes equation (2.10) fully describes the dynamics of incompressible, isothermal flow of a Newtonian fluid.

The discussion of the momentum fluxes shows that in general, two transport mechanisms contribute to the total flux. Convective transport with the overall flow carrying the quantity in question along, and molecular transport, where internal interactions are responsible. A quantity is *passive* if it does not influence these two transport mechanisms by changing the fluid properties.

The general transport equation[5] for a passive scalar s is the convection–diffusion equation,

$$\frac{\partial s}{\partial t} = \Gamma \nabla^2 s - (\boldsymbol{u} \cdot \nabla)s \tag{2.11}$$

with constant diffusivity Γ. The first term on the right-hand side represents the molecular transport processes via diffusion, while the convective term has the same structure as in the momentum equation.

---

[4] Pope, *Turbulent flows*, 2000, p. 17.

[5] Pope, *Turbulent flows*, 2000, p. 21.

The transport of trace amounts of water vapor in humid air can be described by such a convection–diffusion equation. In this case, the diffusivity is the binary diffusion coefficient D of the specific mixture.

The same argument applies to the transport of heat. If heating from viscous dissipation,[6]

$$\mu\phi_v = \frac{1}{2}\mu\sum_{i,j}\left(\frac{\partial u_j}{\partial x_i} + \frac{\partial u_i}{\partial x_j}\right)^2, \tag{2.12}$$

is small, as is the case if neither the velocity gradients nor the viscosity are very large, the internal energy and consequently the temperature of the flow behave as a passive scalars. The transport equation for the temperature T then becomes

$$\frac{\partial T}{\partial t} = \kappa\nabla^2 T - (\boldsymbol{u}\cdot\nabla)T, \tag{2.13}$$

with the thermal diffusivity κ.

A central aspect of non-isothermal flows is natural convection, caused by the temperature dependence of the fluid density and the resulting buoyancy. With the *Boussinesq approximation*,[7] it is possible to recover this effect while retaining the simplified formulations of the momentum and energy equations.

The approximation still considers all fluid properties as constant, but uses the external force term

$$\boldsymbol{f} = -\beta_{T,ref}(T - T_{ref})\boldsymbol{g}, \tag{2.14}$$

with the gravitational acceleration $\boldsymbol{g}$ and the thermal expansion coefficient

$$\beta_{T,ref} = \left(\frac{1}{\rho}\frac{\partial\rho}{\partial T}\right)_{T_{ref}}. \tag{2.15}$$

This corresponds to a linear approximation of the function $\rho(T)$ with respect to a chosen reference temperature T_{ref}. The approach is valid as long as the considered temperature range is small enough to justify this linearized dependence. Additionally, the temperature-related changes in the other fluid parameters that are assumed as constant need to be small as well. Customary, a variation by no more than 10 % defines the validity range of the Boussinesq approximation. The full equation of motion in this case is

$$\frac{\partial\boldsymbol{u}}{\partial t} + (\boldsymbol{u}\cdot\nabla)\boldsymbol{u} = -\frac{1}{\rho_{ref}}\nabla p + \nu\nabla^2\boldsymbol{u} - \beta_{T,ref}(T - T_{ref})\boldsymbol{g}. \tag{2.16}$$

[6] Bird et al., *Introductory Transport Phenomena*, 2014, p. 87.

[7] Gray and Giorgini, *The Validity of the Boussinesq Approximation for Liquids and Gases*, 1976.

The temperature now acts as an *active scalar* again, influencing the flow field via the force term in the velocity equation.

Non-dimensional formulation

The transport equations discussed above determine the change of the variable in question caused by the various mechanisms and forces. As such, they naturally contain the balance between the different contributions. Normalizing with the characteristic scales of the problem allows a non-dimensional formulation of the equations. There, specific dimensionless groups arise that express the balance between the different mechanisms at play.[8]

Starting with the Navier–Stokes equation (2.10), the scales relevant to incompressible, isothermal flow are a characteristic length l_0 and a velocity u_0. Derived from these are a pressure $p_0 = \rho u_0^2$ and a time scale $t_0 = l_0/u_0$. Normalizing with these characteristic scales and substituting the new, non-dimensional variables into (2.10) yields

$$\frac{u_0^2}{l_0}\frac{\partial \boldsymbol{u}}{\partial t} + \frac{u_0^2}{l_0}(\boldsymbol{u}\cdot\nabla)\boldsymbol{u} = -\frac{u_0^2}{l_0}\nabla p + \frac{u_0 \nu}{l_0^2}\nabla^2 \boldsymbol{u}, \qquad (2.17)$$

where $\boldsymbol{u}$, p, t, and the differentiation operators are now in their dimensionless forms. Dividing both sides by u_0^2/l_0 results in

$$\frac{\partial \boldsymbol{u}}{\partial t} + (\boldsymbol{u}\cdot\nabla)\boldsymbol{u} = -\nabla p + \frac{\nu}{u_0 l_0}\nabla^2 \boldsymbol{u}. \qquad (2.18)$$

Here, all remaining dimensional quantities are combined into one expression, defined as the *Reynolds number,*

$$Re = \frac{u_0 l_0}{\nu}. \qquad (2.19)$$

This number gives the balance between convective and molecular transport of momentum or equivalently the balance of inertial and viscous forces.

The structure of the dimensionless Navier–Stokes equation (2.18) shows that the Reynolds number alone governs the evolution of the velocity. Flows at vastly different length scales and velocities or of fluids with different viscosities will still behave similarly if the combination of all three results in a similar Reynolds number.

[8] Bird et al., *Introductory Transport Phenomena*, 2014, p. 147.

Applying this approach to the temperature equation (2.13), with a temperature scale given by a range ΔT and reference point T_0, $\theta = (T - T_0)/\Delta T$, in addition to the normalization employed above gives[9]

$$\begin{aligned} \frac{u_0 \Delta T}{l_0} \frac{\partial \theta}{\partial t} + \frac{u_0 \Delta T}{l_0} (\boldsymbol{u} \cdot \nabla)\theta &= \frac{\kappa \Delta T}{l_0^2} \nabla^2 \theta \\ \Leftrightarrow \frac{\partial \theta}{\partial t} + (\boldsymbol{u} \cdot \nabla)\theta &= \frac{\kappa}{u_0 l_0} \nabla^2 \theta. \end{aligned} \tag{2.20}$$

Again, the expression collecting all the remaining dimensional quantities defines a characteristic dimensionless number,

$$\frac{\kappa}{u_0 l_0} = \frac{\nu}{u_0 l_0} \frac{\kappa}{\nu} = \frac{1}{RePr}. \tag{2.21}$$

The *Prandtl number* $Pr = \nu / \kappa$ is the ratio of momentum diffusion to thermal diffusion. The combination with the Reynolds number as in the dimensionless temperature equation (2.20) expresses the balance between convective and conductive heat transport.

The analogue quantity exists for any variable governed by a convection–diffusion equation (2.11). For mass diffusion, the equivalent is the *Schmidt number* $Sc = \nu / D$.

Similar dimensionless numbers arise for all kinds of additional transport mechanisms. Considering the buoyancy term from the Boussinesq approximation of the Navier–Stokes equation (2.16), the dimensionless formulation (2.18) gets an additional term,

$$\frac{g \beta_{T,ref} \Delta T l_0}{u_0^2} = \frac{g \beta_{T,ref} \Delta T l_0^3}{\nu^2} \frac{\nu^2}{u_0^2 l_0^2} = \frac{Gr}{Re^2} = Ri. \tag{2.22}$$

The *Grashof number* Gr compares buoyant and viscous forces, and the *Richardson number* Ri in turn gives the relative importance of natural and forced convection.

The *Buckingham* Π*-theorem*[10] formalizes the construction of the dimensionless groups for the non-dimensional transport equations. If a problem contains q quantities with d dimensions between them, sets of $q - d$ dimensionless groups exist for the system.

[9] Bird et al., *Introductory Transport Phenomena*, 2014, p. 379.

[10] Buckingham, *On Physically Similar Systems; Illustrations of the Use of Dimensional Equations*, 1914.

As a final example, adding a source term

$$S_{PT} = \frac{h_v}{\rho c_p} \frac{\partial \rho_v}{\partial t} \tag{2.23}$$

to the temperature equation, representing the temperature change in a fluid with the specific heat coefficient c_p due to latent heat associated with a phase change rate $\partial \rho_v / \partial t$ and the specific heat of vaporization h_v, yields the *Jakob number*,

$$Ja = \frac{c_p \Delta T}{h_v}, \tag{2.24}$$

describing the ratio between sensible heat, and latent heat for problems with phase transitions.

Applying the conservation laws of a system to the continuum yields the equations describing the evolution of the flow fields in space and time. These mathematical expressions for the transport of mass, momentum, energy, and additional quantities in the flow encode the fundamental physics of fluid dynamics.

Given the governing equations, discussing the phenomena arising from the underlying dynamics is the natural next step. The dimensionless numbers characterizing general flow regimes provide a solid basis upon which the discussion of flow phenomena can build on.

Turbulent flow

The equations of motions derived in the previous section describe the fundamental dynamics of fluid flow. Flows in nature and in experiments provide a look into the consequences of these dynamics. Observation of inertial flows shows two distinct modes of flow.

In *laminar* flow, fluid moves along smooth trajectories.[11] The flow can be two- or three-dimensional, but there is little exchange between the velocity components.

Above a system-specific critical value of the Reynolds number, the flow becomes unstable and transitions from the laminar to the *turbulent* mode.

In contrast to laminar flow, turbulent flow is always three-dimensional, with vortical structures across a broad range of scales.[12] It is unsteady and irregular, exhibiting fluctuations in both space and time.

Turbulence is very effective in mixing quantities such as momentum, heat, or humidity, with transport rates far exceeding those of

[11] Ferziger et al., *Computational Methods for Fluid Dynamics*, 2020, p. 2.

[12] Ferziger et al., *Computational Methods for Fluid Dynamics*, 2020, p. 347.

molecular diffusion.[13] As a consequence of the momentum mixing, turbulent flows are dissipative. The work due to the viscous shear stresses reducing velocity gradients irreversibly converts kinetic energy to thermal energy.[14]

This dissipation together with the rotational character of the flow separates turbulence from random waves, which have negligible viscous losses and vorticity.[15] The apparent unpredictability of turbulent flows comes not from stochastic processes, but from a high sensitivity to perturbations. Small changes to the initial conditions lead to exponentially growing differences in the flow fields as they evolve in time, similar to chaotic systems.[16]

Despite this chaos, certain features of turbulence are universal across a wide variety of flow geometries and Reynolds numbers. They are connected to the transfer of energy across the different length and time scales, from the macroscopic scales given by the overall geometry down to the smallest scales, at the boundary to molecular processes.

Discussing these features, in particular with respect to turbulent channel flow, allows the identification of critical aspects of the flow that shape the approaches to numerical flow simulations.

The Kolmogorov scale

The motion of fluid in turbulent flow spans a wide range of length scales. Coherent structures within the flow continuously form and break up, transporting energy from the largest to smaller and smaller scales. Finally, a size is reached where inertia can no longer sustain the structures against the viscous forces and they dissipate and vanish.

This final length scale, where dissipation overwhelms inertia, is central to turbulent flow.

The rate at which dissipation removes energy at the smaller scales is directly related to the largest scales. As large structures break up, they transfer energy from their original length scale down to the scale of the smaller structures emerging from the breakup. In an equilibrium state, this cascade of energy is in balance: the energy removed by viscous dissipation is equal to the energy injected into the flow at the largest scale l_0.[17]

At that scale, structures with velocity u_0 have energy proportional to u_0^2. With the associated time scale l_0/u_0, the rate of energy transfer is proportional to u_0^3/l_0 at the top of the cascade.

---

[13] Tennekes and Lumley, *A First Course in Turbulence*, 1972, p. 8.

[14] Ferziger et al., *Computational Methods for Fluid Dynamics*, 2020, p. 347.

[15] Tennekes and Lumley, *A First Course in Turbulence*, 1972, p. 3.

[16] Pope, *Turbulent flows*, 2000, p. 35.

[17] Tennekes and Lumley, *A First Course in Turbulence*, 1972, p. 68.

Consequently, in equlibrium, the dissipation is

$$\epsilon \sim \frac{u_0^3}{l_0}. \tag{2.25}$$

Since the viscosity ν is responsible for the dissipation of this energy flux ϵ at the bottom of the cascade, the smallest scale is determined by both these quantities. By choosing combinations with the appropriate dimensions, the length scale becomes

$$\eta = \left(\frac{\nu^3}{\epsilon}\right)^{1/4}, \tag{2.26}$$

along with the velocity scale u_η and time scale τ,

$$u_\eta = (\epsilon\nu)^{1/4}, \quad \tau = (\nu/\epsilon)^{1/2}. \tag{2.27}$$

These three expressions describe the *Kolmogorov scale*[18] of the flow.

Evaluating the Reynolds number at the Kolmogorov scale yields $Re_\eta = 1$, signifying that below this scale, the inertia of the flow is outweighed by the viscosity of the fluid. This corresponds exactly to the end of eddy break-up at the bottom of the energy cascade.

The arguments leading to the construction of the Kolmogorov scale apply to any kind of turbulent flow. Consequently, on sufficiently small scales, the turbulent velocity fields of different flows are statistically identical when expressed in terms of η, u_η, and τ.[19] The range where this property of turbulent flow applies is the *universal equilibrium range.* It itself consists of the *inertial subrange,* across which the continuous eddy formation and break-up transports the turbulent energy down to the *dissipation range.*

Scales of turbulent channel flow

The scales introduced above exist in every turbulent flow, regardless of the external geometry. Considering now wall-bounded flows, and channel flow in particular, the solid boundary of the wall introduces additional scales and ranges.

A channel consists of two parallel walls with distance 2δ between them. y denotes the wall-normal direction, and x the main flow direction. The spanwise coordinate is z.

In numerical investigations, these walls are the only solid boundaries, and periodic boundaries extend the other to directions to infinity. Experimentally, a rectangular duct with large aspect ratio L_z/L_y provides a similar flow geometry[20] for large x, where effects from the

[18] Pope, *Turbulent flows*, 2000, p. 185.

[19] Pope, *Turbulent flows*, 2000, p. 186f.

[20] Vinuesa et al., *Aspect ratio effects in turbulent duct flows studied through direct numerical simulation*, 2014.

entry into the channel have died down.

At the walls, the molecular interaction between the fluid and the solid surface causes a no-slip boundary condition, where the velocity field goes to zero.

In fully developed channel flow, the mean velocity is independent of x, since the flow is invariant under translation along the channel. From further symmetry arguments, $\langle u_y \rangle = \langle u_z \rangle = 0$, such that the mean velocity field depends only on y.

The channel half-width δ is the natural length scale for channel flow. Together with the bulk velocity

$$u_b = \frac{1}{2\delta} \int u_x \, \mathrm{d}y, \tag{2.28}$$

the Reynolds number for channel flow is $Re = u_b \delta / \nu$. For values of $Re > 900$, the flow is fully turbulent.[21]

The combination of the no-slip boundary condition at the walls and the prescribed bulk velocity u_b implies a mean velocity profile $u(y)$. Directly at the wall, this causes the wall shear stress[22]

$$\tau_w = \mu \left. \frac{\partial \langle u_x \rangle}{\partial y} \right|_w . \tag{2.29}$$

Near the wall, velocities are necessarily small, and, consequently, the viscous forces dominate. The wall shear stress τ_w and the viscosity ν construct the scale for this region, with the *friction velocity*

$$u_\tau = \sqrt{\frac{\tau_w}{\rho}} = \sqrt{\nu \left. \frac{\partial \langle u_x \rangle}{\partial y} \right|_w} \tag{2.30}$$

and the *viscous length scale* $\delta_v = \nu / u_\tau$.

As before with the Kolmogorov scale, the Reynolds number at this scale is $Re_{\delta_v} = 1$. At the same time, it defines the *friction Reynolds number* $Re_\tau = u_\tau \delta / \nu$.

The viscous length scale δ_v defines the *wall units* or *plus units*. These are a dimensionless measure of distance, denoted by a superscript plus sign. The distance from the wall is $y^+ = y/\delta_v = y u_\tau / \nu$, similar to the local Reynolds number.[23] Analogously, the dimensionless velocity becomes $u^+ = u / u_\tau$.

Expressing the mean velocity profile via $\langle u^+ \rangle (y^+)$ reveals that in the *inner layer* of flow near the wall ($y/\delta < 0.1$), the behavior of turbulent channel flow is universal, independent of the Reynolds number.

[21] Pope, *Turbulent flows*, 2000, p. 260.

[22] Pope, *Turbulent flows*, 2000, p. 269.

[23] Pope, *Turbulent flows*, 2000, p. 270.

In the immediate vicinity of the wall, for $y^+ < 5$, the velocity is a linear function of the wall distance: $u^+ = y^+$. This region is the *viscous sublayer*, where the viscosity dominates the flow dynamics.

A second functional dependence between the wall distance and the velocity exists for $y^+ > 30$. Here,

$$u^+ = \frac{1}{\kappa_{vK}} \log y^+ + B, \tag{2.31}$$

with the *von Kármán constant* $\kappa_{vK} = 0.41$ and $B = 5.2$.[24] This logarithmic dependence provides the name for the *log-law region.* In this region, turbulent dynamics dominate the flow.

In between both regions, $5 < y^+ < 30$ lies the *buffer region*, where the behavior of the velocity changes smoothly between both functional descriptions.

Complementing the inner layer that encompasses the three regions discussed above is the *outer layer.* There, the direct influence of the viscosity on the mean velocity profile becomes negligible, and the bulk velocity u_b and channel length scale δ take over as the determining factors for the velocity profile.

The universal behavior of the flow as a function of wall-distance in plus units extends beyond the mean velocity profile. Looking at the fluctuations instead, figure 2.1 shows the peak of the root-mean-square velocity fluctuations,

$$u_{rms} = \sqrt{\left\langle (u - \langle u \rangle)^2 \right\rangle}, \tag{2.32}$$

at $y^+ = 15$. This peak coincides with the peak in production of turbulent kinetic energy.[25] The production peak is well in excess of the dissipation rate. Convection moves the turbulent energy both towards the wall and into the bulk region, while the viscous transport is unidirectional towards the wall, where the dissipation reaches its maximum and the removes the kinetic energy.

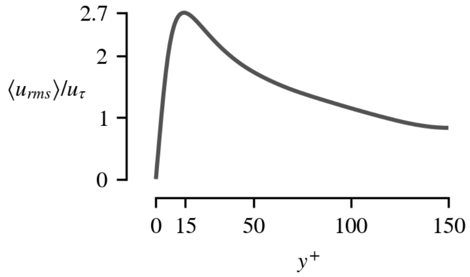

Figure 2.1: The fluctuations of the streamwise velocity in channel flow peak at $y^+ = 15$.

---

[24] Pope, *Turbulent flows*, 2000, p. 274.

[25] J. Kim et al., *Turbulence statistics in fully developed channel flow at low Reynolds number*, 1987.

Concentrating further on this region of maximum turbulent activity shows the existence of certain flow structures. Of particular interest are turbulent *streaks*, *sweeps*, and *ejections*.

Streaks are bands of slow-moving fluid near the wall. They are oriented along the main flow direction, reaching lengths over $\lambda_x^+ = 1000$. In the spanwise direction, the low-velocity streaks alternate with fast-moving fluid, with spacing between $\lambda_z^+ = 80$ – 120.[26,27] This alternating pattern of fast and slow flow directly increases and decreases the velocity gradient near the wall, leading to a similar pattern in the wall shear stress and the friction velocity.

Fluid moving in these streaks is not captured in the wall-near region, but gets ejected from the wall in a macroscopic flow structure with considerable wall-normal velocity. In turn, fluid from the faster-moving flow in-between the streaks moves towards the wall in a sweep.[28]

As large transient flow events, sweeps and ejections are major structures associated with wall-normal, turbulent transport.[29]

Experiments are one way to discover, observe, and investigate turbulent flow and its statistics and structures. Another way are numerical simulations. Knowledge of the governing equation allows computational approaches for simulating flows. The procedures for such simulations are informed by the properties of turbulent flow. They determine the resolution requirements, suitable integration schemes, and overall validity of the various numerical approaches to different flow situations.

Direct numerical simulation

Based on the governing transport equations, it is only natural to try and find theoretical solutions for the variables of turbulent flow. However, the question if a general solution to the Navier–Stokes equation even *exists* is unanswered to date.[30] As such, numerical simulations on a discrete computational grid remain as a method to solve the flow equations.

Numerical flow simulations allow the investigation of flows that might be inaccessible for measurements or difficult to prepare or contain in an experiment. In fact, simulations can provide even impossible flow situations by selectively including and excluding specific forces or transport mechanisms on the fundamental level of the transport equations.[31]

[26] J. Kim et al., *Turbulence statistics in fully developed channel flow at low Reynolds number*, 1987.

[27] C. R. Smith and Metzler, *The characteristics of low-speed streaks in the near-wall region of a turbulent boundary layer*, 1983.

[28] Robinson, *Coherent Motions in the Turbulent Boundary Layer*, 1991.

[29] Wagner and Friedrich, *On the turbulence structure in solid and permeable pipes*, 1998.

[30] Fefferman, *Existence and smoothness of the Navier–Stokes equation*, 2006.

[31] Versteeg and Malalasekera, *An Introduction to Computational Fluid Dynamics*, 2007, p. 111.

Application-oriented simulations employ *Reynolds-averaged Navier–Stokes* (RANS) simulations and increasingly *large-eddy simulations* (LES).

RANS simulations solve averaged flow equations. For steady flows, solving the time-averaged equations yields the mean flow fields, whereas for flows with changing boundary conditions, averaging over ensembles results in an unsteady RANS (URANS) simulation that retains the time-dependence.[32] During averaging, higher order statistical moments arise as additional terms in the equations, making a closed solution impossible. Instead, external models provide expressions for these terms, thereby including the effects of turbulence on the flow in the simulations.

LES in contrast are time-dependent simulations using the original governing equations for the flow. Spatial filtering cuts off the smallest, computationally intensive scales, and only the large, geometry-dependent flow is simulated. The resolved scales still contain the majority of the turbulent kinetic energy, and thus accurately capture the geometry-specific features of the turbulent flow. A sub-grid model then adds back the additional contributions of the filtered small scales, which are easier to describe in a general approach than the effects of turbulence across all scales and in different geometries.[33]

Both RANS and LES use models to describe at least some of the effects of turbulence on the overall flow, especially at the smallest scales, where viscous forces dominate.

Here, the focus will instead be on a model-free approach. *Direct numerical simulations* (DNS) are fully resolved simulations of turbulent flow. They provide a valuable tool for turbulence research, and results obtained by DNS feed forward to improve the models used in RANS and LES.

DNS describes the process of simulating turbulent flow by numerically integrating the partial differential equations that govern the fluid dynamics. The key aspect is the resolution of all relevant scales. This requirement loops back to the discussion of the intrinsic scales of turbulent flow.

Since at the fundamental level, turbulence is the consequence of viscosity, the scales where viscous forces dominate must be resolved in order to get the correct flow behavior. Consequently, the spatial resolution of the DNS needs to be on the order of the Kolmogorov length scale η (2.26).

[32] Ferziger et al., *Computational Methods for Fluid Dynamics*, 2020, p. 364.

[33] Versteeg and Malalasekera, *An Introduction to Computational Fluid Dynamics*, 2007, p. 66.

This resolution requirement is the central disadvantage of DNS. In a system with characteristic length l_0, the number of points to cover this range is $l_0/\eta \sim Re^{3/4}$. The cost of a three-dimensional computation is therefore proportional to $Re^{9/4}$ from the number of grid points alone. Adding the required temporal resolution leads to an overall computational cost of $\mathcal{O}(Re^3)$.[34] This limits DNS to Reynolds numbers much lower than those achievable in LES or RANS.

The largest DNS to date contextualize the meaning of *low* Reynolds number. For channel flow, the highest friction Reynolds number achieved in DNS is $Re_\tau = 10\,000$.[35] In terms of grid points, the record stands at $1.8 \cdot 10^{18}$, simulating turbulence with $Re_\lambda = 1300$ based on the Taylor microscale.[36]

The finite-volume method

Different methods exist for numerically solving the Navier–Stokes equation. For DNS, most prominently used are *(pseudo-) spectral* methods and *finite-volume* methods.

In spectral methods,[37] a linear combination of global basis functions ψ_n form the velocity field,

$$\boldsymbol{u}(x,y,z,t)_M = \sum_m \alpha_m(t)\boldsymbol{\psi}_m(x,y,z). \tag{2.33}$$

The choice of the basis depends on the desired boundary condition. Chebychev and Jacobi polynomials serve well for wall-bounded flows, while a Fourier representation best accommodates periodic boundaries.

Replacing the velocity $\boldsymbol{u}$ with the series representation $\boldsymbol{u}_M$ from equation (2.33) leads to an optimization problem, where the residual arising from the finite M is minimized. This results in a system of $M \times M$ ordinary differential equations for the time development coefficients $\boldsymbol{\alpha}(t) = (\alpha_1, \dots, \alpha_M)$. Solving for $\boldsymbol{\alpha}$ using the convection term at $N > M$ collocation points in the domain then immediately returns the approximation for the velocity field, with its evolution obtained by advancing $\boldsymbol{\alpha}$ in time.

The spectral approach allows very efficient computations using fast transforms for the calculation of the convection term, the coefficients $\boldsymbol{\alpha}$, and the velocity $\boldsymbol{u}_M$. Further, the method converges superpolynomially to the true solution when increasing the number of basis functions M, resulting in low errors at reasonable computational cost.

---

[34] Coleman and Sandberg, *A Primer on Direct Numerical Simulation of Turbulence – Methods, Procedures and Guidelines*, 2010.

[35] Oberlack et al., *Turbulence Statistics of Arbitrary Moments of Wall-Bounded Shear Flows: A Symmetry Approach*, 2022.

[36] Buaria et al., *Self-attenuation of extreme events in Navier–Stokes turbulence*, 2020.

[37] Coleman and Sandberg, *A Primer on Direct Numerical Simulation of Turbulence – Methods, Procedures and Guidelines*, 2010.

However, the required global basis functions cannot adequately describe any but the simplest flow geometries and increase the difficulty when treating inlet–outlet boundaries.

The finite volume method[38] does not have these limitations, for the costs of less computational efficiency and worse convergence behavior. In this approach, the domain is made up from small *control volumes* or *cells.* Evaluation of the field values happens typically at the center of the cell. Finite-volume DNS have successfully reproduced experimental measurements of turbulent flows with accuracy comparable to spectral DNS.[39]

The key aspect of the finite volume method is using the conservation laws contained within the integral form of the flow equations.

Considering the general convection–diffusion equation (2.11) to illustrate the approach, integrating over a small control volume *cv* gives

$$\int_{cv} \frac{\partial s}{\partial t} \, \mathrm{d}V + \int_{cv} \nabla \cdot (\boldsymbol{u} s) \, \mathrm{d}V = \int_{cv} \nabla \cdot (\Gamma \nabla s) \, \mathrm{d}V. \tag{2.34}$$

Now, applying Gauß' divergence theorem to the integrals over divergences results in integrals over the boundary of the control volume instead:

$$\int_{cv} \frac{\partial s}{\partial t} \, \mathrm{d}V + \int_{A} \boldsymbol{u} s \, \mathrm{d}\boldsymbol{A} = \int_{A} \Gamma \nabla s \, \mathrm{d}\boldsymbol{A}, \tag{2.35}$$

with $\boldsymbol{A}$ the surface-normal vector scaled with surface area A. Considering only one dimension for clarity, the control volume boundaries are *faces* at $w = x - \Delta x$ and $e = x + \Delta x$, leading to the *discretized* formulation,

$$\frac{\partial s}{\partial t} V + \left(us|_e A - us|_w A \right) = \left(\Gamma \left. \frac{\mathrm{d}s}{\mathrm{d}x} \right|_e A - \Gamma \left. \frac{\mathrm{d}s}{\mathrm{d}x} \right|_w A \right). \tag{2.36}$$

Here, identifying the remaining volume integrals with the average over the control volume $\langle s \rangle_{cv}$ consequently gives the value assigned to the cell center s. Figure 2.2 shows a schematic overview of this setup.

This result describes the balance equation for s: the change within the volume is equal to the net convective flux plus the net diffusive flux through the faces of the volume.

Since neighboring control volumes share a face where the flux out of one volume must equal the flux into the next, performing the integration over all control volumes leads to a system of algebraic equations. Incorporating the boundary conditions $s(x_0)$ and $s(x_1)$ at the limits of the domain allows solving for s.

[38] Versteeg and Malalasekera, *An Introduction to Computational Fluid Dynamics*, 2007, p. 115.

[39] Eggels et al., *Fully developed turbulent pipe flow: a comparison between direct numerical simulation and experiment*, 1994.

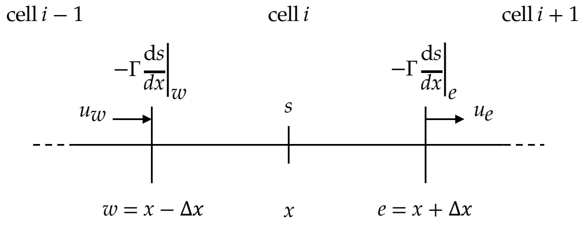

Figure 2.2: The value s at the cell center i changes with the flux of s through the boundaries to the neighboring cells.

Calculating the fluxes through the faces to all neighboring cells results in the same kind of system of connected equations as illustrated in figure 2.2 above for one dimension. Extending the approach to three dimensions is straight-forward.

A time-marching scheme then advances this solution to the next time step $t + \Delta t$. Chapter 3 will discuss the specifics of the time integration as well as the role of pressure for the integration of the Navier–Stokes equation (2.10) based on the actual approach employed for this investigation.

The solution of (2.36) requires the values of s at the face boundaries in addition to the values at the cell center. Calculating the spatial derivatives on the finite grid poses a similar problem. Interpolation between the center values of neighboring cells provides the value on the shared boundary face. The choice of the interpolation scheme directly impacts the convergence of the calculation with increasing grid resolution. Various stencils exist that incorporate macroscopic features of the specific simulated flow into the interpolation.

DNS places specific demands on the discretization scheme. The simulation must accurately calculate the viscous dissipation at the smallest scales to obtain the correct overall flow results. Therefore, the discretization scheme must be accurate, conserve energy, and not introduce additional *numerical dissipation*.

This excludes all upwind schemes, which are commonly used in simulations of stationary flows. There, the combination of biasing the interpolation to reflect the flow direction increases the convergence to the result, while the numerical dissipation stabilizes the calculation.[40]

DNS instead requires an unbiased, *central differencing* scheme with high accuracy.

[40] Ferziger et al., *Computational Methods for Fluid Dynamics*, 2020, p. 354.

In the simplest central scheme, the values of s at the centers i and $i+1$ of two neighboring cells of a uniform grid both contribute to the face value,

$$s_{i,i+1} = \frac{s_i + s_{i+1}}{2}. \tag{2.37}$$

On a non-uniform grid, the contributions are weighted with the ratio of the distance between face and center compared to the distance between the centers themselves.

The difference of the Taylor series expansions of $s_{i\pm1}$ yields the spatial derivative in cell i via

$$\frac{\partial s}{\partial x} = \frac{s_{i+1} - s_{i-1}}{2\Delta x} - \underbrace{\frac{1}{6}\Delta x^2 \frac{\partial^3 s}{\partial x^3}}_{\mathcal{O}(\Delta x^2)} + \mathcal{O}(\Delta x^4). \tag{2.38}$$

Expressing the derivative as

$$\frac{\partial s}{\partial x} \approx \frac{s_{i+1} - s_{i-1}}{2\Delta x} \tag{2.39}$$

is therefore second-order accurate in Δx, that is, the *discretization error* behaves as $\mathcal{O}(\Delta x^2)$.

On a non-uniform grid with step sizes h_i, h_k, equation (2.38) becomes

$$\frac{\partial s}{\partial x} = \frac{s_{i+1} - s_{i-1}}{h_i + h_k} - \underbrace{\frac{1}{2}(h_i - h_k)\frac{\partial^2 s}{\partial x^2}}_{\mathcal{O}(\Delta h)} + \mathcal{O}(h^2) \tag{2.40}$$

because of the incomplete cancellation of the first-order terms.[41] On such grids, gradual variation of the step size is necessary to preserve the accuracy of the scheme by ensuring that $\Delta h = \mathcal{O}(h^2)$.

Higher order schemes, taking into account neighbor-of-neighbor cells, lead to better accuracy for equal resolution, but demand knowledge of the specific, predetermined structure of the computational grid. As such, they are generally not available for unstructured grids as employed for complex flow geometries.[42]

Specific to the application in flow simulations are the consequences of the discretization error. In a convective flow, both *diffusion*, resulting in an artificial decay in the field amplitude from numerical dissipation, and *dispersion*, causing phase error, arise from the original discretization error. For second-order central differences, both again behave as $\mathcal{O}(\Delta x^2)$.

DNS ties together the mathematical formulation of the fluid dynamics and the structure found in turbulent flows. Without

[41] Sundqvist and Veronis, *A simple finite-difference grid with non-constant intervals*, 1970.

[42] Tu et al., *Computational Fluid Dynamics A Practical Approach*, 2018, p. 136.

additional turbulence modeling, the correct flow behavior arises directly from the governing equations. Understanding the relevant scales of all turbulent flows informs the resolution requirements for the simulation, as well as the demands placed on the numerical schemes used to solve the equations. In turn, DNS produces high-quality data on turbulence, including quantities that are virtually inaccessible in experiments, thereby providing new insights into turbulent flow structures.

Starting from the baseline of single-phase flow, the study of flows with phase transition naturally considers multi-phase flows. Again, DNS allows simulation of such flows to investigate the modifications of the flow caused by the additional phases and the transition between them.

DNS of multi-phase flow

The specific kind of multi-phase flow relevant to condensation in humid air flow is *dispersed* multi-phase flow.[43] Here, the continuous gas phase carries along discrete droplets of liquid water.

In the most general case, there is a four-way coupling of the flow constituents. Momentum exchange happens between the carrier phase and the droplets in both directions, and in elastic and inelastic collisions of droplets with other droplets. If the volume occupied by the droplets is small compared to the overall flow volume, the probability of collisions becomes negligible. Then, only the two-way coupling between the droplets and the air remains.

Treating the droplets as point particles, the velocity $\boldsymbol{v}_i$ of single droplet is then influenced by the velocity field of the gas phase $\boldsymbol{u}$,[44]

$$\frac{\mathrm{d}\boldsymbol{v}_i}{\mathrm{d}t} = (\boldsymbol{u} - \boldsymbol{v}_i)\frac{r}{\tau_p}, \tag{2.41}$$

where r is a drag factor and

$$\tau_p = \frac{\rho_d}{\rho}\frac{d_i^2}{18\nu} \tag{2.42}$$

is the characteristic time scale of a droplet with density ρ_d and diameter d_i.

From the conservation of momentum, the momentum change of the carrier phase has to be equal and opposite to the summed momentum change of all droplets. This results in a force term,

$$F_d = -\sum_i m_i \frac{\mathrm{d}\boldsymbol{v}_i}{\mathrm{d}t}\delta(\boldsymbol{x} - \boldsymbol{x}_i), \tag{2.43}$$

[43] Balachandar and Eaton, *Turbulent Dispersed Multiphase Flow*, 2010.

[44] Russo et al., *Water droplet condensation and evaporation in turbulent channel flow*, 2014.

with the Dirac delta function to localize the force at the positions of the respective particles. A DNS solves equation (2.41) once for every droplet in the flow to obtain the complete flow fields.

The ratio of the droplet time scale and the Kolmogorov time scale gives the *Stokes number*,[45] $St = \tau_p / \tau$. It expresses the ability of a particle to follow the surrounding flow. In the limit of $St \to 0$, the equation of motion (2.41) shows that, in the absence of an external force, $\boldsymbol{v}_i = \boldsymbol{u}$ after an arbitrarily short time. Consequently, no further momentum is exchanged between gas and droplets. Effectively, there remains a one-way coupling between the continuous and the dispersed phase. The velocity of the droplets is completely determined by the air, and the flow of the air is the same as it would be in the single-phase case.

If a statistical description of the droplet concentration replaces tracking the discrete droplet positions, the resulting approach treats the multi-phase flow as a *dusty gas*.[46] Here, single-phase flow transports the droplet concentration as a scalar field.

These different coupling regimes form the basis for multi-phase DNS. Depending on the application or the focus of the investigation, choosing full four-way coupling, two-way coupling, or one-way coupling is appropriate. The accuracy of the simulation and its computational costs counterbalance each other.

For an even closer representation of the behavior of flows carrying particles, DNS can resolve the moving boundaries of the particles instead of assuming point particles.[47] Calculating force and torque across the whole surface then describes both the translational and rotational degrees of freedom for every particle as precisely as possible.

The next chapter will instead explore a different approach, resembling most closely the dusty-gas model. By formulating the concentration field as an active scalar and re-introducing coupling terms from the dispersed phase towards the carrier, the DNS can simulate phase transition effects and their influence on the underlying turbulent flow, while preserving the low cost and ease of handling of the simplified treatment of the dispersed particles.

[45] Prosperetti and Tryggvason, *Computational Methods for Multiphase Flow*, 2007, p. 17.

[46] Balachandar and Eaton, *Turbulent Dispersed Multiphase Flow*, 2010.

[47] Uhlmann, *Interface-resolved direct numerical simulation of vertical particulate channel flow in the turbulent regime*, 2008.

3

Active scalar phase change modeling

All the various approaches of multi-phase DNS briefly outlined in the previous chapter can simulate the effects of phase transition on the overall flow.

In humid air flow at ambient conditions, the influence of liquid water on the flow of the gas phase is negligible under certain circumstan–ces. Effects of the condensation and evaporation, however, can still affect the flow of the humid air. A method including phase transition, while not requiring simulation of all involved phases, would allow investigations of these flows at reduced computational costs.

To this end, the *active scalar phase change model* characterizes humid air via the concentration of water vapor and does not calculate the flow equations for liquid water. This concentration field is transported by convection and diffusion, analogous to the temperature field. Modifying the temperature based on changes in the concentration field and vice versa models the phase transition.

For moderate subcooling of $\simeq 10\,\mathrm{K}$, this approach captures the influence of phase transition on humid air flow. The computational costs incurred by the addition of the concentration field and the calculation of the coupling terms are far lower than those of a multi-phase DNS.

Using the active scalar phase change model allows the simulation of humid air flow including phase transition effects in situations where employing a multi-phase DNS would be prohibitively expensive, especially given that the flow of the liquid phase might not be relevant at all.

As long as the phase transition effects can be formulated in terms of a single phase, they can be added to the approach without losing the advantage of simulating this phase alone.

Single-phase formulation of phase transition

By formulating phase transition in terms of the effects on one of the phases, these can then be included in a single-phase simulation.

A source term describing the heating and cooling of the fluid from the release and absorption of latent heat is added to the temperature equation. Conversely, the source term responsible for generation and removal of vapor concentration depends on the temperature field via a saturation condition. Additionally, concentration differences introduce solutal buoyant forces to the velocity equation.

In this way, the approach yields a system of equations describing the flow of humid air as a single phase, while simultaneously including phase transition effects.

The following sections discuss the underlying assumptions of the active scalar phase change model and specify the construction of the vapor concentration field and its coupling to the temperature and velocity evolution.

Model assumptions

The central assumption of the active scalar phase change model is the irrelevance of the flow of the liquid phase with respect to the gas phase.

Since any interaction between the two phases happens at the gas-liquid interface, this assumption implies that there are no interface dynamics originating in the liquid phase that significantly influence the gas phase.

The first effect to consider is the density change from ρ_l and ρ_g during the transition between liquid and gas. Phase transition of a fluid mass m_{PT} causes a change in fluid volume,

$$\Delta V = m_{PT} \left(\frac{1}{\rho_g} - \frac{1}{\rho_l} \right) . \tag{3.1}$$

The resulting velocity divergence within a volume V_{ref} containing the interface surface A_{ref} is then[1]

$$\nabla \cdot \boldsymbol{u} = \frac{A_{ref}}{V_{ref}} \phi_{PT} \left(\frac{1}{\rho_g} - \frac{1}{\rho_l} \right) . \tag{3.2}$$

[1] Tryggvason et al., *Direct numerical simulations of flows with phase change*, 2005.

The phase transition mass flux ϕ_{PT} is given by the Hertz–Knudsen–Schrage equation,[2]

$$\phi_{PT} = \frac{2}{2-\xi_c}\sqrt{\frac{M}{2\pi R}}\left(\xi_c \frac{p_v}{\sqrt{T_v}} - \xi_e \frac{p_l}{\sqrt{T_l}}\right), \tag{3.3}$$

where M is the molar mass of the vapor, R is the universal gas constant, p_v and p_l are the vapor pressure in the gas phase and of the liquid respectively, along with the corresponding temperatures T_v and T_l. The condensation and evaporation coefficients ξ_c and ξ_e describe the probability of a molecule remaining in the opposite phase after collision with the interface if the thermodynamic conditions for the respective phase change process are met.

If ϕ_{PT} is small compared to the convective mass flux of the flow, the velocity modification caused by the non-zero source term in equation (3.2) becomes negligible compared to the overall motion of the fluid. This is the case when the difference between p_v and p_l is small, in other words: when subcooling or superheating are small. Under these circumstances, neglecting the velocity change from expansion or compression of the fluid at the interface is justified.

Secondly, external forces acting on the liquid can move the interface, thereby exchanging momentum with the flow. For example, condensate droplets might be pushed across a substrate by the aerodynamic forces of the flow, or pulled down by gravity. In this case, evaluation of the *Bond* and *Weber number* is necessary to decide if the assumption of a static interface is valid. The Bond number (also *Eötvös number*) is the ratio of gravitational to capillary forces,[3]

$$Bo = \frac{\rho_l g r^2}{\sigma}, \tag{3.4}$$

with droplet radius r and the surface tension σ. Similarly, the Weber number is[4]

$$We = \frac{r \rho u_b^2}{\sigma}. \tag{3.5}$$

For small droplets as characterized by $We, Bo < 1$, the effect of external forces on the droplets is small and approximating the interface as static is valid.

Vapor concentration as an active scalar

Humid air is a homogeneous mixture of dry air and water vapor. In addition to the usual dependence on the thermodynamic variables, the properties of the fluid as a whole are determined by the mixing ratio of both components.

[2] Marek and Straub, *Analysis of the evaporation coeffcient and the condensation coeffcient of water*, 2001.

[3] Prosperetti and Tryggvason, *Computational Methods for Multiphase Flow*, 2007, p. 16.

[4] Bird et al., *Introductory Transport Phenomena*, 2014, p. 148.

Since humid air at ambient conditions contains only trace amounts of vapor, the mixing ratio is expressed here as the molar vapor fraction[5] carried by the dry air,

$$c = \frac{n_{vap}}{n_{total}} = \frac{p_v}{p_{total}}, \tag{3.6}$$

where n_{vap} is the molar amount of vapor and n_{total} the total amount of the combined mixture.

A convection–diffusion equation describes the transport of this quantity,

$$\frac{\partial c}{\partial t} = D\nabla^2 c - \boldsymbol{u} \cdot \nabla c + S_c. \tag{3.7}$$

The source term S_c contains the change in the vapor fraction due to condensation and evaporation. Formulating the Hertz–Knudsen–Schrage equation (3.3) in terms of c, the concentration change in reference to a volume V_{ref} with interface area A_{ref} is

$$S_c = -\frac{2\xi_c}{2-\xi_c}\frac{A_{ref}}{V_{ref}}\sqrt{\frac{R}{2\pi M}}\left(c\sqrt{T_v} - c_l\sqrt{T_l}\right), \tag{3.8}$$

using the ideal gas law, $pV = nRT$, as the equation of state.

With this source term, equation (3.7) describes the transport of the vapor fraction as a passive scalar. Its evolution is fully determined by the temperature and velocity of the fluid, but there is no interaction in the reverse direction.

Modifying the equations for the evolution of the velocity and the temperature to include effects due to changing vapor fraction completes the inclusion of water vapor as an active scalar.

As discussed earlier, condensation and evaporation cause the release and absorption of latent heat proportional to the mass flux across the phase boundary. Adding a source term of the form

$$S_T = -\frac{h_v}{c_p}S_c \tag{3.9}$$

to the temperature equation reflects this heating or cooling effect.

The coupling between the velocity field and the vapor concentration is realized via the buoyant forces.[6] Analogous to the treatment of thermal buoyancy in the Boussinesq approximation, the changing vapor concentration causes a change in the density of the humid air with respect to a reference value ρ_{ref}. With a solutal expansion coefficient

$$\beta_c = -\frac{1}{\rho_{ref}}\left.\frac{\partial \rho}{\partial c}\right|_{c_{ref}} \tag{3.10}$$

[5] Bird et al., *Introductory Transport Phenomena*, 2014, p. 491.

[6] Bahavar and Wagner, *Direct Numerical Simulation of Convective Channel Flow with Temperature and Concentration Gradients*, 2017.

the linearized contribution to the buoyant force is

$$\boldsymbol{B}_c = \beta_c (c - c_{ref}) \boldsymbol{g}. \tag{3.11}$$

Summing the solutal and the thermal buoyancy yields the total buoyant force[7,8] acting on the fluid as a result of variations in temperature and vapor fraction.

Including the solutal buoyancy completes the mutual coupling between the flow fields: For the temperature and the vapor fraction, the source terms S_c and S_T depend on both fields simultaneously. The velocity field determines the convective transport of both temperature and vapor fraction, and in turn, these act as active scalars by influencing the velocity field via buoyancy.

The full set of governing equations for the active scalar phase change model consists of the continuity equation (2.2), the convection–diffusion equations for both temperature and vapor concentration including the phase change source terms,

$$\frac{\partial T}{\partial t} = \kappa \nabla^2 T - \boldsymbol{u} \cdot \nabla c + S_T, \tag{3.12}$$

$$\frac{\partial c}{\partial t} = D \nabla^2 c - \boldsymbol{u} \cdot \nabla c + S_c, \tag{3.13}$$

and the velocity equation including thermal and solutal buoyancy,

$$\frac{\partial \boldsymbol{u}}{\partial t} + (\boldsymbol{u} \cdot \nabla) \boldsymbol{u} = -\frac{1}{\rho_{ref}} \nabla p + \nu \nabla^2 \boldsymbol{u} - (\boldsymbol{B}_T + \boldsymbol{B}_c) \,. \tag{3.14}$$

Condensate droplets

Discarding the liquid phase instead of calculating its dynamics is central to the single-phase formulation. However, as the rates of condensation and evaporation are calculated to obtain the appropriate source terms for the active scalars, the accumulated amount of liquid can be tracked under the assumption that the liquid remains static.

This is useful when investigating condensate forming on surfaces, where the mobility of the liquid is reduced by surface tension. By further restricting the topology of the accumulated condensate, for example requiring a continuous film to form, the boundary conditions of the solid surface in question can be modified to reflect the effects of the static liquid layer.

[7] Hammou et al., *Laminar mixed convection of humid air in a vertical channel with evaporation or condensation at the wall*, 2004.

[8] Kimura and Smyth, *Direct numerical simulation of salt sheets and turbulence in a double-diffusive shear layer*, 2007.

Implementation in OpenFOAM

The preceding section describes the mathematical formulation of the active scalar phase change model. The mutually coupled transport equations for temperature, vapor fraction, and velocity describe phase transition effects in a single-phase formulation.

This formulation is adapted to a specific use case: flow of humid air at ambient conditions through a vertical channel with a cooled wall. In particular, the limited range of temperature and vapor concentration and the resulting low phase transition mass flux lead to a simplified formulation of the source terms for the active scalars, in effect treating phase transition as an instantaneous phenomenon.

The underlying flow simulation is implemented in OpenFOAM,[9] utilizing the library's capabilities for customizable flow simulations to create a state-of-the-art finite-volume DNS solver, which works in conjunction with the active scalar phase change model.

Channel flow with temperature and humidity

Channel flow is one of the canonical configurations for the study of turbulent flows. Results from experimental[10] as well as numerical investigations[11] provide a wealth of knowledge upon which investigations of additional effects can expand.

For numerical simulations, channel flow is understood as flow between two parallel planes, the channel walls, with periodic boundaries along the direction of the mean flow as well as in the remaining spanwise direction. In such a configuration, the only characteristic dimension is the distance between the channel walls, given as two times the channel half-width δ. Of interest for this investigation are flows around $Re_\tau \approx 150$, at the lower end of the Reynolds number range sufficient to sustain turbulent flow.

Starting from isothermal channel flow, the first modification of this baseline is the existence of a temperature difference between the channel walls. In the presence of gravity, the resulting temperature gradients within the fluid give rise to buoyancy, as discussed previously.

In a vertical channel, the mean flow is (anti-)parallel to the direction of gravity. Thus, the buoyant forces act to aid or oppose the flow along the channel, accelerating or decelerating the fluid.

Such a differentially heated, vertical channel provides the base configuration for this investigation.

[9] The OpenFOAM Foundation, *www.openfoam.org*, 2021.

[10] Hussain and Reynolds, *Measurements in Fully Developed Turbulent Channel Flow*, 1975.

[11] J. Kim et al., *Turbulence statistics in fully developed channel flow at low Reynolds number*, 1987.

Given the focus on air flow at ambient conditions, the temperature differences encountered are $\Delta T \leq 30\,\mathrm{K}$, meaning the fluid properties—apart from density—can be considered constant, and the changes in density fall within the range of validity of the Boussinesq approximation.

The imposed forced convection is set to be large compared to the contribution from natural convection, with Richardson number $Ri \ll 0.1$. This preserves comparability to the canonical, isothermal case.

Expanding upon this differentially heated flow setup, the presence of humidity in the air flow introduces the potential for phase transition.

Again, the parameter range is constrained by the use case. At ambient conditions, the vapor fraction of humid air is small enough as to not influence the fluid properties beyond the scope of the Boussinesq approximation. At a reference temperature of 293 K, the vapor fraction is $c = 0.023$ for saturated humid air. Together with the limited temperature range discussed above, this limits the need to account for large subcooling or superheating. Allowing for a temperature difference of 10 K is sufficient for these conditions. Consequently, the heat and mass fluxes at the phase boundary are small compared to the convective fluxes through the channel. This allows the use of the active scalar phase change model.

In such a flow setup, the large-scale dynamics are those of forced convection. However, on smaller scales, the effects of temperature and humidity modify the flow with respect to the canonical case. This provides an opportunity to isolate the influence of adding temperature, humidity, and phase transition on turbulent channel flow.

Direct numerical simulation in OpenFOAM

The OpenFOAM library provides the general tools for flow simulations with the finite-volume method. Spatial interpolation and differentiation use the built-in second-order accurate central differencing schemes.

On top of the standard library, several custom functionalities address the specific needs of DNS in general and the active scalar phase change model in particular.

The first of these is an explicit time integration scheme. Mirroring the requirements for the spatial discretization scheme, the fully resolved nature of DNS necessitates high accuracy of the time integration.

Implicit schemes trade accuracy and computational costs per time step for unconditional stability. They are well-suited for the solution of numerically stiff flow equations,[12] allowing large time steps which lead to faster convergence when simulating stationary flows.

In DNS, the requirement to resolve the smallest turbulent time scales precludes using large time steps. This favors explicit schemes with high accuracy and lower computational costs per time step.[13,14,15]

In this implementation, the Euler-leapfrog integration scheme provides second-order accurate results for the evolution of the velocity field. For more efficient calculation, the acceleration term

$$\boldsymbol{a} = \underbrace{\nu \nabla^2 \boldsymbol{u}}_{\boldsymbol{D}} \quad \underbrace{-(\boldsymbol{u} \cdot \nabla)\boldsymbol{u}}_{\boldsymbol{C}} \quad \underbrace{-1/\rho \, \nabla p_{global}}_{\boldsymbol{P}} \tag{3.15}$$

includes only the global pressure gradient term $\boldsymbol{P}$ next to the diffusive term $\boldsymbol{D}$ and convective term $\boldsymbol{C}$. The fluctuating pressure contributions are added afterwards in a correction step.

The initial integration uses a first-order Euler step to obtain the field $\boldsymbol{u}^*_{t+1}$ at time $t + 1 \;=\; t + \Delta t$ from the current velocity $\boldsymbol{u}_t$ and acceleration $\boldsymbol{a}_t$,

$$\boldsymbol{u}^*_{t+1} = \boldsymbol{u}_t + \Delta t \,(\boldsymbol{D}_t + \boldsymbol{C}_t + \boldsymbol{P}_t). \tag{3.16}$$

After this initial step, the leapfrog algorithm calculates the future value by staggering the evaluation of the velocity and the acceleration term:

$$\boldsymbol{u}^*_{t+1} = \boldsymbol{u}_{t-1} + 2\Delta t \,(\boldsymbol{D}_{t-1} + \boldsymbol{C}_t + \boldsymbol{P}_t). \tag{3.17}$$

Using the time-lagged diffusive term $\boldsymbol{D}_{t-1}$ addresses the slight instability of the scheme when calculating both convection and diffusion.[16]

The structure of the time derivative in the scheme (3.17) is the same as for the spatial derivative in the central differencing scheme (2.39), with the same second-order accuracy of the approximation.

A special averaging step to attenuate oscillations replaces the leapfrog integration step every 50 time steps. In this case, the updated value is

$$\boldsymbol{u}^*_{t+1} = \frac{1}{2}\,(\boldsymbol{u}_{t-1} + \boldsymbol{u}_t) + \frac{3}{2}\Delta t \,(\boldsymbol{D}_{t-1} + \boldsymbol{C}_t + \boldsymbol{P}_t). \tag{3.18}$$

Figure 3.1 shows a schematic overview of the three different time integration schemes for the Euler step (3.16), the leapfrog step (3.17), and the averaging step (3.18).

[12] Coleman and Sandberg, *A Primer on Direct Numerical Simulation of Turbulence – Methods, Procedures and Guidelines*, 2010.

[13] Ferziger et al., *Computational Methods for Fluid Dynamics*, 2020, p. 352.

[14] Versteeg and Malalasekera, *An Introduction to Computational Fluid Dynamics*, 2007, p. 112.

[15] Ketcheson et al., *More efficient time integration for Fourier pseudospectral DNS of incompressible turbulence*, 2019.

[16] Manhart, *A zonal grid algorithm for DNS of turbulent boundary layers*, 2004.

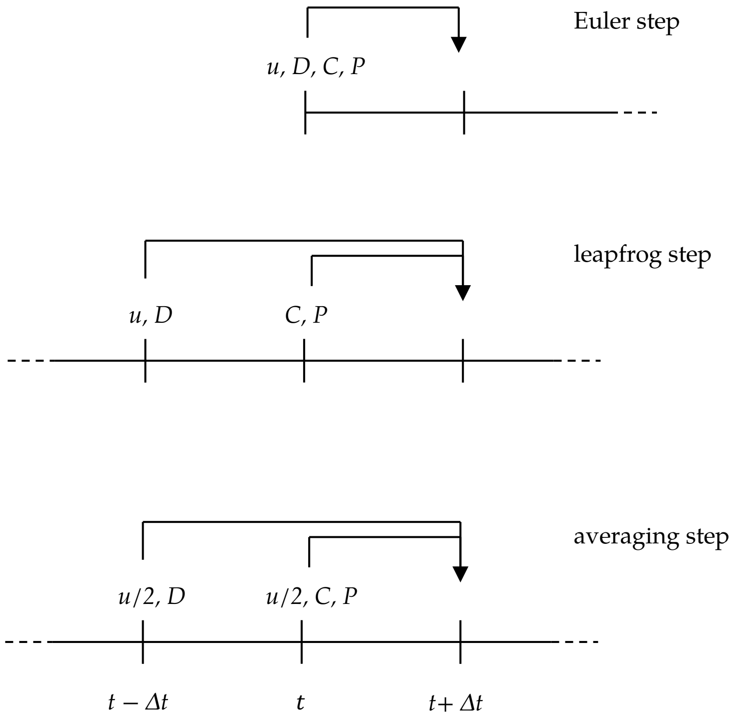

Figure 3.1: The initial Euler step feeds into the leapfrog time integration, interrupted by the averaging step every 50 time steps.

The projection method now adds the contribution of the pressure fluctuations[17].[18] It ensures a divergence-free velocity field by correcting the initial result for the velocity field $\boldsymbol{u}^*_{t+1}$.

The difference between the estimated value $\boldsymbol{u}^*_{t+1}$ and the correct solution $\boldsymbol{u}_{t+1}$ must be due to the neglected contribution of the pressure field. Based on equation (3.17), this difference is

$$\boldsymbol{u}_{t+1} - \boldsymbol{u}^*_{t+1} = 2\Delta t \left(-\frac{1}{\rho} \nabla p \right). \tag{3.19}$$

Taking the divergence of both sides yields

$$\nabla \cdot \boldsymbol{u}_{t+1} - \nabla \cdot \boldsymbol{u}^*_{t+1} = -\frac{2\Delta t}{\rho} \nabla^2 p. \tag{3.20}$$

To satisfy the continuity equation, the divergence of the correct solution must vanish, $\nabla \cdot \boldsymbol{u}_{t+1} = 0$. The remaining parts of equation (3.19) form a Poisson equation for the pressure field,

$$\nabla^2 p = \frac{\rho}{2\Delta t} \nabla \cdot \boldsymbol{u}^*_{t+1}. \tag{3.21}$$

[17] Chorin, *Numerical solution of the Navier–Stokes equations*, 1968.

[18] Kath and Wagner, *Highly Resolved Simulations of Turbulent Mixed Convection in a Vertical Plane Channel*, 2016.

Solving for p results in the pressure field that corrects the initial guess for the velocity, such that the physical solution is

$$\boldsymbol{u}_{t+1} = \boldsymbol{u}^*_{t+1} - 2\Delta t \, \frac{1}{\rho} \nabla p, \tag{3.22}$$

which is divergence-free by construction.

This combination of second-order central differences, the second-order leapfrog integration scheme, and the projection method is itself second-order accurate in time and exactly conserves energy for the convection problem.[19]

The stability of the explicit time integration scheme imposes an additional upper limit on the size of the time step. In a convection–diffusion problem, the second-order accurate scheme is stable if[20]

$$\Delta t \leq \left(\sum_i \frac{|u_b|}{\Delta x_i} + \sum_i \frac{4D}{\Delta x_i^2} \right)^{-1}. \tag{3.23}$$

Here, i indexes the three spatial coordinates, and D is the largest relevant diffusion coefficient of the transport problem.

With this restriction of the simulation time step, it is useful to consider the hierarchy of the different time scales of the problem before discussing the implementation of the phase transition source term for the active scalar model.

Using the fact that the simulation is tailored towards a specific setup as outlined before, consider channel flow at $Re = 2000$.

The convective time scale $t_c = \delta / u_b$ sets the macroscopic scale. Using this as the reference, the viscous time scale $t^+ = \delta / u_\tau = 14.75 \, t_c$ characterizes the evolution of the near-wall turbulent flow structures. Next, the Kolmogorov micro-scale $\tau = \sqrt{\nu\delta \, / u_b^3} = 0.022 \, t_c$ is the scale of the smallest structures that need to be resolved in DNS. Framing now the maximum simulation time step obtained from the stability criterion of equation (3.23) in the same way shows that $\Delta t = 0.014 \, t_c$ for a spatial resolution Δx sufficient for DNS. Since this value is smaller than the Kolmogorov scale, an efficient simulation chooses the time step close to the maximum stable value.

From the condensation rate given in equation (3.8), a time scale for the phase transition emerges as

$$t_{PT} = \Delta x \sqrt{\frac{2\pi M}{RT}} = 0.0003 \, t_c = 0.02 \Delta t. \tag{3.24}$$

Critically, the phase transition is very fast even compared to the simulation time step. Consequently, it is valid to treat the process

[19] Manhart, *A zonal grid algorithm for DNS of turbulent boundary layers*, 2004.

[20] Shishkina and Wagner, *Stability conditions for the Leapfrog-Euler scheme with central spatial discretization of any order*, 2004.

as instantaneous in the context of the overall simulation by simply restoring the phase equilibrium during every time step.

Restoring the equilibrium by condensation or evaporation is equivalent to moving along a linear trajectory in the T–c phase space. The trajectory originates at the initial values T_1 and c_1 and proceeds with slope $-c_p/h_v$ until it intersects the saturation curve at T_2, c_2, illustrated in figure 3.2 This reflects the release of latent heat during the phase transition.

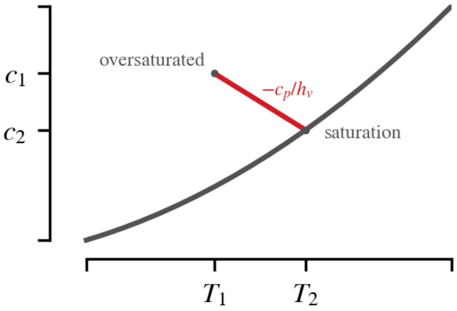

Figure 3.2: During condensation, the evolution of concentration and temperature follows a linear trajectory through the phase space, until it reaches equilibrium as it intersects the saturation curve.

A quadratic polynomial approximates the saturation curve well over the relevant temperature range for ambient conditions:

$$c_{sat} \simeq 3.923 \cdot 10^{-5}\,\mathrm{K}^{-2}\,T^2 - 0.022\,\mathrm{K}^{-1}\,T + 2.96, \tag{3.25}$$

with a maximum error of less than 1 % compared to the exponential reference formulation (1.2). With this quadratic formulation, the analytical solution for the intersection with the phase change trajectory is available for maximum computational efficiency.

Implemented in this way, the active scalar phase change model enables the DNS of humid air flow with condensation and evaporation with only minimal additional computational costs compared to a simulation without phase transition.

In a final step, the single-phase approach can include the accumulation or evaporation of sessile droplets at the channel wall. While the active scalar model disregards the liquid phase, using a scalar field analogous to the vapor concentration field allows tracking the condensate mass on the channel walls.

Since the DNS calculates the phase change mass flux at every time step of the simulation, the microscopic dynamics of accumulation or disappearance of condensate are readily available. However, the growth of condensate is a slow process compared to the time scales of turbulent flow.

For a uniform condensate film growing at the channel wall, the supply of excess vapor Δc in the bulk flow with respect to saturation at the wall,

$$\phi_c = \Delta c \rho_v u_b, \tag{3.26}$$

presents the upper limit to the condensation rate ϕ_{PT} and in turn to the growth velocity u_f. Assuming complete condensation of all vapor Δc that exceeds the saturation concentration at the wall,

$$u_f = \frac{1}{\rho_l}\phi_{PT} < \Delta c \frac{\rho_v}{\rho_l} u_b, \tag{3.27}$$

where ρ_v and ρ_l are the density of pure vapor and the liquid condensate, respectively. Because both this density ratio and the oversaturation at ambient conditions are small, $u_f \ll u_b$ and, consequently, the time scale of condensate growth t_l is longer than the convective time scale t_c by a factor of $\sim 10^4$.

DNS of the turbulent channel flow for such long times would not only be prohibitively expensive, but also unnecessary: Since the time scales for the dynamics of the flow are much shorter than t_l, the accumulation dynamics are only governed by the average flow. Obtaining these average values of the flow fields over $\sim 100 t_c$ and then extrapolating to t_l therefore provides a reliable prediction for the distribution of condensate mass at the walls.

This spatially resolved distribution of liquid mass allows the creation of a plausible droplet pattern.

The condensate droplets grow directly from condensation adding water to the individual droplet, and from coalescing with neighboring droplets. This leads to a self-similar growth pattern, with new droplets forming between larger, agglomerated droplets. In this combined growth regime, the mean droplet radius grows linearly with time.[21]

Since the droplet size depends on the amount of locally available condensate, the size of the largest droplets depends directly on the accumulation time. Because this time span is extrapolated, its exact length is a matter of choice, and the droplet size becomes a free parameter of the final droplet pattern.

The algorithm to create a plausible droplet pattern based on the extrapolated accumulated mass is as follows: Choosing a maximum droplet radius R, the wall surface is divided into a grid with spacing $s \cdot R$, where $s > 2$ is a parameter determining the droplet spacing,

$$\text{center–to–center: } s \cdot R, \tag{3.28}$$

$$\text{edge–to–edge: } (s-2) \cdot R. \tag{3.29}$$

[21] Medici et al., *Edge effects on water droplet condensation*, 2014.

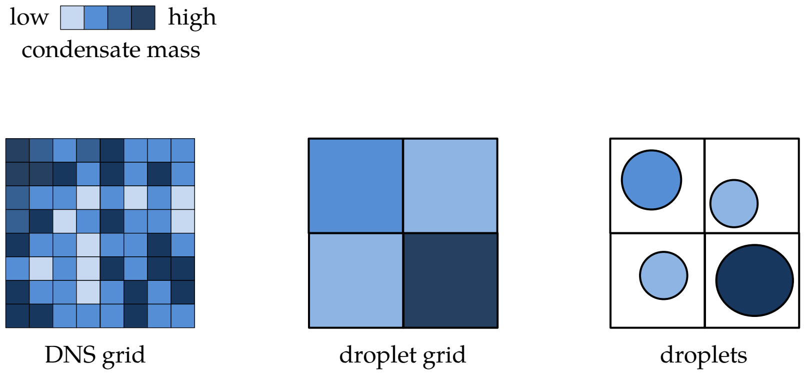

Figure 3.3: The grid-based approach operates on the coarser droplet grid, which conserves the condensate mass of the underlying DNS grid. The droplet size within each cell depends on the available mass.

Within each of these grid cells, the available liquid mass is consolidated into a droplet with radius $R' \leq R$ and contact angle ϑ. This ensures that the relative size between droplets across the whole surface reflects the underlying structure of the phase transition mass fluxes.

The droplets are then placed randomly within their respective cell to break the artificial regularity of the original grid. Figure 3.3 illustrates this process.

This approach conserves condensate mass on the grid level. As droplet mobility is restricted by the surface forces, condensate mass stays localized and transport across the wall is negligible. The process of microscopic droplets growing into each other and the self-similar dynamics lead to a large droplet that dominates the interaction with the flow. This is mimicked by considering only one droplet concentrating all available mass within itself.

The resulting droplet pattern is not a direct result of the DNS. It is, however, a plausible distribution that is consistent with the local phase change mass fluxes obtained by the DNS, as well as with the known, real dynamics of droplet growth.

Larger droplets will have a larger influence on the flow of the humid air. This is especially true if only the largest droplets reach out of the viscous sublayer of the flow.

To investigate the influence of the droplet pattern on the turbulent flow, the channel wall itself is deformed, creating in effect solid representations of the liquid droplets.

As these droplets are static and have no internal dynamics, the single-phase character of the active scalar phase change model is preserved, but with an added one-way coupling from the droplets to the flow fields. The pattern remains fixed, with no droplets appearing or disappearing during simulations following the initial placement.[22]

Validation

To ensure that the DNS implementation as detailed above generates reliable results, simulations of two different configurations of turbulent channel flow are compared to results from the literature.

The first configuration is a differentially heated vertical channel with aiding and opposing buoyancy at the heated and cooled walls, respectively.[23,24]

The comparison between the finite-volume DNS in OpenFOAM and a spectral DNS shows good agreement for the mean flow fields as well as for the average fluctuations near the walls, while slightly underestimating them in the bulk.

A simulation of a channel without buoyant forces, but with condensation and evaporation serves to evaluate the active scalar phase change model. The comparison is drawn to a simulation employing a multi-phase DNS with two-way coupling between the liquid and the gaseous phase.[25]

The model captures the effects of the phase transition on the flow fields. Effects caused by interactions between the droplets and the fluid are lost, as expected from the single-phase approach.

Combined, the results from both comparisons confirm both the implementation of the DNS in OpenFOAM and the active scalar condensation model as valid tools for investigating humid air flow at ambient conditions. Here, droplet loading of the flow is small and can safely be neglected.

Differentially heated vertical channel

Comparison of the results obtained by the OpenFOAM DNS to those of a spectral DNS[26] serves to evaluate the reliability of the finite-volume DNS for channel flows with buoyancy.[27]

The flow configuration for this investigation is a differentially heated vertical channel as shown in figure 3.4. The fluid flows against the direction of gravity, resulting in aiding buoyant forces at the heated

[22] Maschkio, *CFD-Simulation der Be- und Enttauungsprozesse in Kfz-Scheinwerfern*, 2006, p. 82.

[23] Kasagi and Nishimura, *Direct numerical simulation of combined forced and natural turbulent convection in a vertical plane channel*, 1997.

[24] Wetzel and Wagner, *Buoyancy-induced effects on large-scale motions in differentially heated vertical channel flows studied in direct numerical simulations*, 2019.

[25] Russo et al., *Water droplet condensation and evaporation in turbulent channel flow*, 2014.

[26] Kasagi and Nishimura, *Direct numerical simulation of combined forced and natural turbulent convection in a vertical plane channel*, 1997.

[27] Kath and Wagner, *Highly Resolved Simulations of Turbulent Mixed Convection in a Vertical Plane Channel*, 2016.

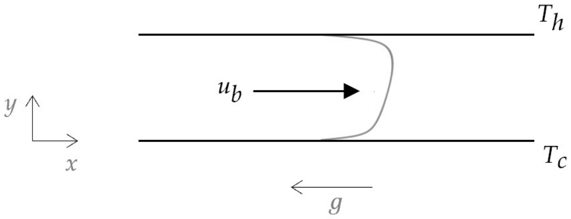

Figure 3.4: The buoyant forces in the differentially heated setup lead to an asymmetric velocity profile.

wall, while the flow is opposed at the cooled wall. The thermal diffusivity is consistent with that of air, with $Pr = 0.71$.

The channel dimensions are $5\pi\delta \times 2\delta \times 2\pi\delta$ along the streamwise (x), wall-normal (y), and spanwise (z) direction, with both streamwise and spanwise periodicity. It is discretized into $392 \times 180 \times 316$ hexahedral cells to satisfy the resolution requirements of the DNS.[28] Along the periodic directions, the grid is uniform with spacing $\Delta x^+ = 6$ and $\Delta z^+ = 3$.

A hyperbolic tangent distribution increases the resolution near the walls to a maximum of $\Delta y^+ = 0.2$ to better capture the large gradients of the flow fields. The minimum resolution at the centerline of the channel is $\Delta y^+ = 3.7$. The hyperbolic tangent distribution is optimal with respect to numerical errors from the stretching ratio between cells in non-uniform meshes.[29]

Critically, the size difference of two adjacent cells,

$$\Delta h \sim 2h^2 \sinh(y)\cosh(y) = \mathcal{O}(h^2), \tag{3.30}$$

preserves the second-order accuracy of the central differencing scheme according to equation (2.40).

At the channel walls, no-slip and impermeability boundary conditions are applied, simulating the flow conditions found at physical walls. Additionally, constant temperatures are imposed, $T = T_h$ at $y/\delta = 1$ and $T = T_c$ at $y/\delta = -1$. The buoyancy arising from the temperature difference $\Delta T = T_h - T_c$ is quantified via the Grashof number,

$$Gr = \frac{g\beta_T \Delta T \delta^3}{\nu^2} = 1.2 \cdot 10^5. \tag{3.31}$$

A self-correcting pressure gradient Δp drives the flow with a prescribed bulk velocity u_b through the channel.

[28] Grötzbach, *Spatial resolution requirements for direct numerical simulation of the Rayleigh-Bénard convection*, 1983.

[29] Vinokur, *On One-Dimensional Stretching Functions for Finite-Difference Calculations*, 1983.

Based on the bulk velocity, the Reynolds number is

$$Re = \frac{u_b \delta}{\nu} = 2280, \tag{3.32}$$

and $Re_\tau = 150$.

Adding vortical structures consistent with this Re_τ to the initial velocity field aids the transition to fully developed turbulence.[30]

The ratio $Ri = Gr/Re^2 = 0.023$ characterizes the overall flow as mixed convection. Contributions from both forced and natural convection shape the resulting flow fields.

Figures 3.5 and 3.6 show averages and root-mean-square fluctuations of these flow fields as obtained by the spectral DNS[31] and the OpenFOAM implementation.

The angled brackets $\langle \cdot \rangle$ denote averaging in time as well as along both periodic directions, such that the wall-normal coordinate is the remaining independent variable of the profiles.

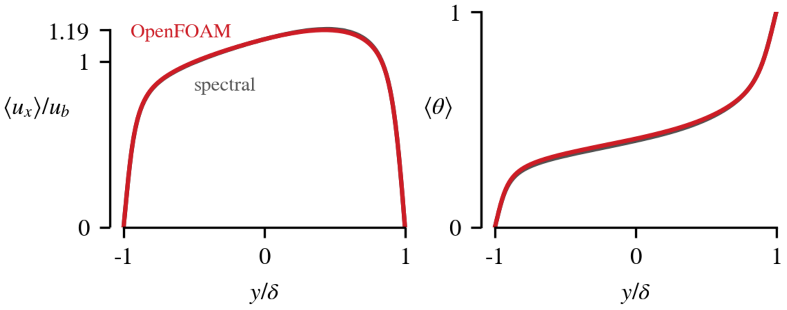

Figure 3.5: The mean profiles of the streamwise velocity (left) and the temperature (right) are in agreement between the spectral DNS and the implementation in OpenFOAM.

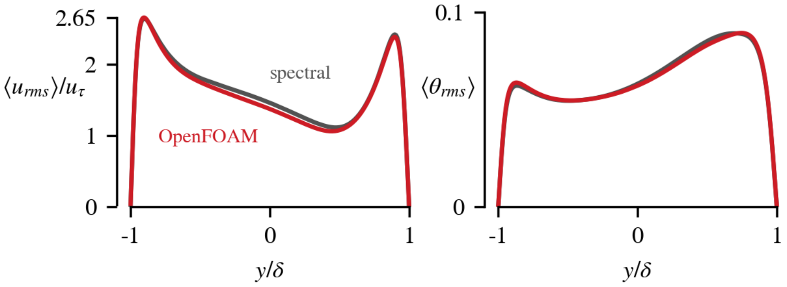

Figure 3.6: The OpenFOAM implementation underestimates the fluctuations of the streamwise velocity in the bulk compared to the spectral DNS (left). Temperature fluctuations, however, are in good agreement between both methods (right).

Figure 3.5 shows the mean streamwise velocity, normalized with the bulk velocity, and the mean dimensionless temperature, with

$$\theta = \frac{T - T_c}{\Delta T}. \tag{3.33}$$

[30] de Villiers, *The Potential of Large Eddy Simulation for the Modelling of Wall Bounded Flows*, 2006, p. 164.

[31] Kasagi and Nishimura, *Direct numerical simulation of combined forced and natural turbulent convection in a vertical plane channel*, 1997.

Both simulations are in agreement across the complete channel height.

Agreement is also good for the temperature fluctuations, shown in the right panel of figure 3.6. In contrast, the comparison in the left panel shows that the OpenFOAM DNS underestimates the fluctuations of the streamwise velocity compared to the spectral DNS in the bulk. Results at the peaks near both walls are again similar between both simulations.

The comparison between results of a spectral DNS and the OpenFOAM implementation of a finite-volume DNS underlines that the latter is a reliable tool for investigating channel flow with aiding and opposing buoyancy. Slight deviations for the velocity fluctuations in the bulk are not a sign of deficiency of the implementation, but result from the fundamental difference between spectral and finite-volume methods.

Condensation and evaporation in channel flow

A second simulation shows the capability of the active scalar approach to model phase change effects. Here, the basis for comparison is a state-of-the-art two-way coupled multi-phase DNS of humid air flow with water droplets, along with simulations of the same flow with inert particles instead of droplets.[32]

Again, the investigated geometry is a channel with periodic boundaries in the streamwise (x) and spanwise (z) directions. The size of the domain is $4\pi\delta \times 2\delta \times 2\pi\delta$. Reflecting the shorter channel length at equal Reynolds number, a mesh with $314 \times 180 \times 316$ cells provides the same resolution as in the previous validation case.

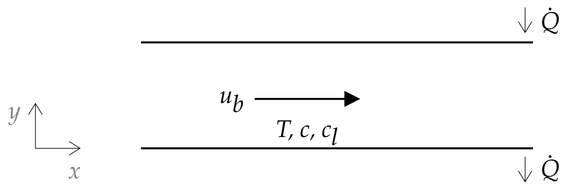

Figure 3.7: The channel is heated and cooled with constant heat flux $\dot{Q}$ at the walls, driving the evolution of temperature T, vapor fraction c, and liquid fraction c_l.

Instead of a isothermally heated and cooled walls, the boundary condition at the channel walls is a constant heat flux with opposing signs. Consequently, the wall temperature is a result of the heat transfer through the fluid. Figure 3.7 shows a schematic overview of the flow setup.

[32] Russo et al., *Water droplet condensation and evaporation in turbulent channel flow*, 2014.

The initial vapor concentration is set equal to the saturation concentration at the initial fluid temperature. Throughout the simulation, evaporation and condensation occur to retain the equilibrium.

The multi-phase simulation seeds 2 million droplets homogeneously throughout the domain, for a total volume fraction of $2.2 \cdot 10^{-4}$. The flow of the fluid transports these droplets along the channel, where they act as reservoirs for the phase transition mass transfer to and from the fluid.

For the single-phase approach of the active scalar model, this reservoir is realized as an auxiliary scalar field that tracks the amount of available liquid water. It is expressed as a concentration c_l, compatible to the treatment of the vapor fraction c. The field is transported by convection only,

$$\frac{\partial c_l}{\partial t} = -\boldsymbol{u} \cdot \nabla c_l + S_l. \tag{3.34}$$

The phase transition source term is the complement to the vapor concentration source, $S_l = -S_c$. Initially, the field is homogeneous within the channel, and its integral magnitude is equal to that of the 2 million droplets of the multi-phase simulation combined, with the same overall volume fraction.

With the active scalar model and without buoyancy, the phase transition only modifies the temperature field via the release and absorption of latent heat. Therefore, the comparison between temperature profiles obtained with the single-phase approach and the multi-phase DNS serves as the benchmark for the performance of the active scalar model for phase transition.

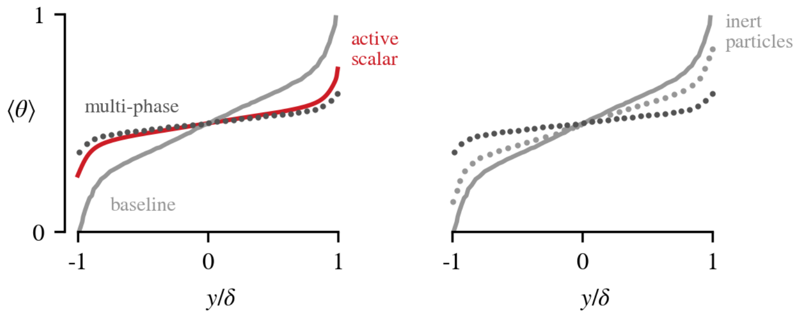

Figure 3.8: The single-phase approach is able to capture the majority of the phase transition effects included in the multi-phase DNS with liquid droplets (left).In particular, this approach gives a better approximation than a simulation including particles but without phase change (right).

The left panel of figure 3.8 shows the profiles of the average normalized temperature

$$\theta = \frac{T - T_{ref}}{\Delta T_{ref}}, \qquad (3.35)$$

where the reference values refer to the case of a differentially heated channel without phase transition.[33] Compared to this baseline, the additional heat transfer due to condensation and evaporation reduces the temperature difference between the walls. The multi-phase simulation accounts for the full magnitude of this temperature change, while the single-phase approach captures $\geq$ 77 % of the effect, depending on y. Since the active scalar model neglects the interaction between the water droplets and the air flow, the highest deviation from the multi-phase DNS occurs directly at the walls, where turbophoresis increases the droplet concentration.

The effect of the particles alone is shown in the right panel of figure 3.8. Neglecting phase transition effects, inert particles with non-zero heat capacity increase the heat transfer by providing an additonal transport mechanism on top of the convective transport of heat with the fluid. This effect accounts for only 41 % of the temperature change observed directly at the walls in the multi-phase simulation. Overall, the temperature profile remains far closer to the baseline, with steeper gradients across the complete channel compared to both the multi-phase DNS and the active scalar model results.

The comparison to the two-way coupled multi-phase simulation shows that the active scalar model provides a very close approximation of the full impact of the phase transition for large parts of the temperature profile. In particular, including the latent heat effects, but neglecting the droplets in the flow yields a far better approximation to the full picture than the complementary approach of simulating inert particles.

[33] Bahavar and Wagner, *Condensation-induced flow structure modifications in turbulent channel flow investigated in direct numerical simulations*, 2020.

Summary and perspective

The formulation and subsequent implementation of the active scalar phase change model on top of a single-phase DNS provides a reliable way for simulating humid air flow with phase transition.

It includes the primary thermodynamic effect of the phase change process by using both temperature and vapor concentration as active scalars. Their coupling via the source terms reflects the heating and cooling of the fluid from the release and absorption of latent heat during condensation and evaporation.

Additionally, the approach creates a plausible pattern of sessile droplets, satisfying local mass conservation based on the microscopic phase change mass flux. Extrapolating based on averaged fields and mimicking the agglomeration process in a grid-based approach allows the placement of droplets as a result of the condensation process.

The comparison to state-of-the-art DNS both with and without phase transition shows the reliability of the numerical implementation. For flows where the subcooling is small and condensation primarily occurs on the cooled surface, simulations using the single-phase approach are expected to yield valid results at negligible added computational costs.

Thus, the active scalar phase change model will be the tool used for investigating the interplay between condensation and turbulence.

4

Interactions between turbulence and condensation

Flow of humid air through a cooled channel is an extension of the canonical case of differentially heated channel flow. The flow in cooled channel flow with condensation is a perturbed version of the flow arising from the aiding and opposing buoyant forces in differentially heated setups.

In contrast to the periodic channels used for validation purposes, the primary investigation geometry from here on out is a channel in an inlet–outlet configuration. This setup allows the observation of the evolution of the thermal boundary layer along the channel, as well as the effect of the diminishing global temperature and vapor concentration differences between the wall and the bulk flow.

Simulations with and without phase transition isolate the influence of condensation on the overall flow through the channel. Performing calculations both in a smooth channel and with condensate droplets at the wall further separates the effects of the release of latent heat and associated buoyancy on the one hand from the flow modification caused by the surface roughness presented by the droplets on the other hand.

The investigation in the smooth channel builds upon previous investigations on the effects of condensation on turbulent flow structures. They show that buoyancy associated with the release of latent heat is the dominant consequence of condensation. Acting against the aiding buoyant force caused by the cooling of fluid at the wall, it opposes the damping of turbulence.[1] In the channel with condensate droplets, turbulence is enhanced by the wall roughness. The changed shape of the cooled surface causes a positive feed-back loop between droplets and phase transition. Condensation rates are higher at the surface of droplets compared to flat areas, leading to increased growth of already existing droplets.[2]

[1] Bahavar and Wagner, *Condensation-induced flow structure modifications in turbulent channel flow investigated in direct numerical simulations*, 2020.

[2] Bahavar and Wagner, *Sessile condensate droplets as quasi-static wall deformations in direct numerical simulations of channel flow with condensation*, 2022.

Channel flow in an inlet–outlet configuration

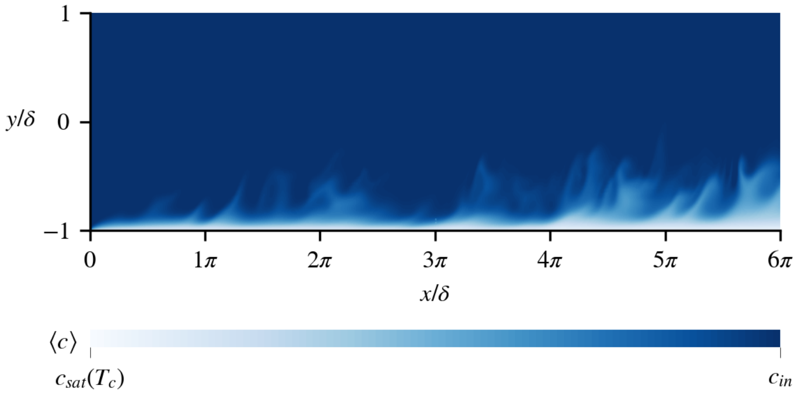

Figure 4.1: The instantaneous vapor concentration field in the xy-plane of the channel shows condensation near the cooled wall and the ejection of dried fluid back into the bulk.

Investigating the flow of humid air through a cooled channel with defined inlet and outlet boundaries yields results that are more readily comparable to experimental data and more easily applied to realistic flow configurations.

It allows the observation of boundary layer growth, as well as of effects due to the constantly diminishing amount of humidity available for condensation along the channel and the progressively stronger acceleration of the fluid near the cooled wall.

However, the channel remains periodic in the spanwise direction to reduce computational costs. These savings are twofold: First, the additional homogeneous flow direction allows spatial averaging and thus decreases time to statistical convergence of the flow variables. Second, the periodic boundary removes the need to resolve an extra boundary layer at the side walls.

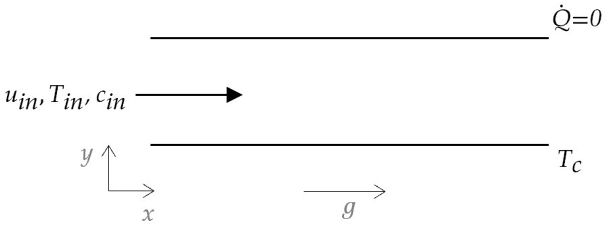

Figure 4.2: Humid air enters with defined temperature and vapor concentration and flows downwards through a vertical channel with a cooled wall.

Figure 4.2 shows the flow configuration. Fluid flows through the vertical channel along the direction of gravity. The fluid properties reflect those of humid air, with $Pr = 0.73$ and $Sc = 0.65$.

At the channel inlet, the fluid temperature and humidity are T_{in} and c_{in}. One channel wall is an adiabatic boundary, while the opposite wall is cooled with respect to the inflow temperature and kept isothermally at T_c. Critically, the temperature of the wall is below the saturation temperature, providing subcooling of $T_{sat}(c_{in}) - T_c = 10\,\mathrm{K}$, such that condensation occurs at this wall.

The temperature difference between the inlet and the wall ΔT causes an aiding buoyant force along the cooled wall, quantified by $Gr_T = 38\,000$. Similarly, condensation increases the fluid density, causing additional solutal buoyancy with $Gr_c = 1500$ in the same direction as the thermal contribution, obtained with $\Delta c = c_{in} - c_{sat}(T_c)$.

The phase transition ties together vapor concentration and temperature, with a Jakob number of $Ja = c_p \Delta T / h_v = 0.012$.

Von-Neumann boundary conditions apply to the concentration field at the walls and at the outlet to allow undisturbed evolution within the channel volume.

Both walls present no-slip and impermeability conditions for the velocity. To ensure fully developed turbulent flow throughout the complete investigation domain, a precursor simulation provides the velocity boundary condition at the inlet, together with a zero-gradient condition for the pressure.[3] Conversely, there is a combination of fixed pressure and zero velocity gradient boundaries at the outlet.

The precursor simulation consists of a channel with periodic boundaries in both the streamwise and spanwise directions. An isothermal DNS continuously calculates turbulent channel flow with the desired Reynolds number, $Re = 2000$. The corresponding friction Reynolds number is $Re_\tau = 135$. At the periodic boundary, the current velocity field propagates into the investigation domain.[4,5] Figure 4.3 shows this setup schematically.

The dimensions of the precursor domain are $4\pi\delta \times 2\delta \times 2\pi\delta$ in the streamwise (x), wall-normal (y), and spanwise direction, while the investigation domain is $6\pi\delta$ in length to allow for longer observation along the aperiodic streamwise direction.

Exact matching of the spatial discretization of both domains avoids disturbances at the interface.

[3] Wagner, *Direkte numerische Simulation turbulenter Strömungen in einer Rohrerweiterung*, 1996.

[4] Lund et al., *Generation of Turbulent Inflow Data for Spatially-Developing Boundary Layer Simulations*, 1998.

[5] Bellec et al., *Large Eddy Simulations of thermal boundary layer developments in a turbulent channel flow under asymmetrical heating*, 2017.

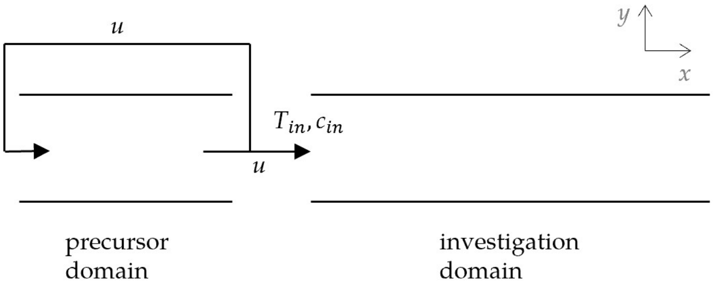

Figure 4.3: Direct mapping of the velocity from the periodic boundary of the precursor provides the inlet velocity field for the investigation domain.

For the smooth channel, the geometry is discretized with 800 × 180 × 316 hexahedral cells, with 320 streamwise cells in the generation domain and 480 in the investigation domain. This results in a resolution of $\Delta x^+ = 5.3$ and $\Delta z^+ = 2.7$, while a hyperbolic tangent distribution of the grid points in the wall-normal direction provides increased resolution near the channel walls with $\Delta y^+ = 0.18$, and reduced resolution in the bulk, where $\Delta y^+ = 3.2$.

Resolution requirements are higher in the case with condensate droplets at the cooled channel wall. To sufficiently resolve the curved surface of the droplets as well as to eliminate artificial anisotropy, the streamwise resolution in the investigation domain is increased to match the spanwise resolution, $\Delta x^+ = \Delta z^+ = 3$. As this increased resolution is not necessary in the precursor simulation, a second hyperbolic tangent distribution blends the meshes in both domains. At the periodic boundary of the generation domain, the streamwise resolution exactly matches that of the investigation domain with $\Delta x^+ = 3$, while the minimum resolution stays at $\Delta x^+ = 6$ in the center along the streamwise direction. The hyperbolic tangent distribution reduces the number of cells in the precursor domain by 36 % compared to a uniform resolution of $\Delta x^+ = 3$.

The resulting mesh consists of 1200 × 162 × 280 cells, with 360 streamwise cells in the precursor domain and 840 cells in the investigation domain.

Condensate droplets

Due to the extrapolating nature of the droplet generation method detailed in the preceding chapter, the maximum droplet size is a free parameter of the approach. The following considerations constrain this choice: First, the radius of the minimal thermodynamically viable droplet is[6]

$$R_{min} = \frac{2\sigma T_{sat}}{\rho_l h_v \Delta T}, \tag{4.1}$$

where σ is the surface tension of the liquid droplet with density ρ_l, and ΔT is the subcooling between the surface temperature and the saturation temperature T_{sat}. This lower bound arises from the Kelvin equation,[7] which governs the change in vapor pressure as a function of interface curvature. Below this radius, the change in the dew point temperature equivalent to this shift of the saturation pressure exceeds the subcooling, causing such a droplet to evaporate.

Conversely, the largest possible radius for a droplet on a vertical wall is given by Young's law,[8]

$$R_{max} = \sqrt{\frac{3\left(\cos\vartheta_R - \cos\vartheta_A\right)}{\rho_l g}}. \tag{4.2}$$

At this size, the weight of the droplet is exactly counterbalanced by the maximum adhesive force caused by the difference between the receding and advancing contact angles ϑ_R and ϑ_A.

For a water droplet on a typical metallic surface and for the subcooling specified above, the minimum and maximum radii are $R^+_{min} = 10^{-5}$ and $R^+_{max} = 14.5$.

Further, DNS of spheres packed at the wall of a channel shows that below a radius of $R^+ = 5$, the influence of these spheres on the first and second order statistical moments of the flow is negligible.[9]

If the largest droplets have a height $h^+ < 5$, they do not significantly alter the flow through the channel. Consequently, extrapolating the condensate accumulation using the condensation rates of the smooth channel is valid.

At some point during the condensate accumulation, the largest droplets will grow beyond this size and start to influence the flow. Still, the majority of the droplets is small, and the conditions for condensation stay similar to the smooth channel.

To obtain results on the effect of condensate droplets on the flow and the condensation rates, all modeled droplets should have the potential to influence the flow. Choosing a radius for the largest droplets such that the smallest droplets still reach the necessary height of $h^+ = 5$ satisfies this condition.

---

[6] Mei Maofei et al., *A fractal analysis of dropwise condensation heat transfer*, 2009.

[7] Rose, *Dropwise condensation theory and experiment: A review*, 2002.

[8] Dussan and Chow, *On the ability of drops or bubbles to stick to non-horizontal surfaces of solids*, 1983.

[9] Chan-Braun et al., *Force and torque acting on particles in a transitionally rough open-channel flow*, 2011.

At this extrapolated point in time, all droplets in the pattern contribute to flow modification, while the time for which some of the droplets already potentially have changed the condensation dynamics is minimal.

This choice justifies the assumption that the accumulation of condensate occurs according to the average condensation rates obtained for the smooth channel. A larger maximum radius would violate this assumption, while on the other hand a smaller radius would mean that the majority of the droplets does not influence the flow, rendering the investigation moot.

Based on these considerations, the maximum droplet radius is set to $R^+_{max} = 10$ for hemispherical droplets with contact angle $\vartheta_{max} = 90°$.

Respecting the local mass conservation of the droplet pattern, spherical caps with footprint radius R and height h form droplets with volumes below that of a complete hemisphere with radius R_{max}, while keeping the same curvature.

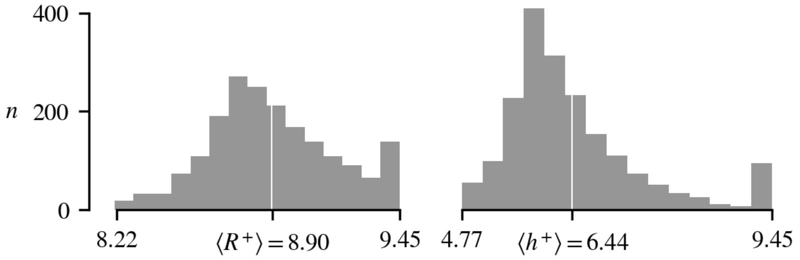

Figure 4.4: Conserving the local condensate mass during the grid-based generation of the droplet pattern results in slightly asymmetrical distributions for the droplet footprint radii (left) and heights (right).

The droplet pattern consists of 1900 droplets, based on a 76×25 grid on the cooled wall. Figure 4.4 shows the resulting distribution of the footprint radii and heights. The mean footprint radius and height are $\langle R^+ \rangle = 8.90$, and $\langle h^+ \rangle = 6.44$. Together, this gives a mean contact angle of $\langle \vartheta \rangle = 71°$. With a minimum droplet height of $h^+_{min} = 4.77$, all droplets have sufficient height to reach out of the viscous sublayer and influence the flow. The deformation due to this droplet pattern increases the wall surface area by 6.4 %.

The underlying mass transfer rates that determine the distribution and relative sizes of the droplets, which are obtained from simulations of the smooth channel, will be discussed in more detail later in this chapter.

The pattern explicitly contains only the largest droplets. In between, covering almost the whole surface, are droplets down to the minimum viable size.[10] These droplets, deep within the viscous

[10] S. Kim and K. J. Kim, *Dropwise Condensation Modeling Suitable for Superhydrophobic Surfaces*, 2011.

sublayer, are neglected here because of their negligible direct interaction with the turbulent flow.

The droplet pattern is included in the channel simulation by directly deforming the cooled wall to reflect the surface of the spherical caps representing the droplets. Since the Bond (3.4) and Weber numbers (3.5) of the droplet distribution are small with $Bo \leq 0.42$ and $We \leq 0.007$, these droplets are static and not influenced by the drag of the flowing air or by gravity.

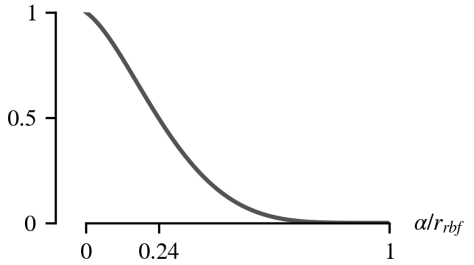

Figure 4.5: The mesh deformation at the wall propagates into the volume, weighted according to the distance from the original displacement via the radial base function W2.

To preserve the quality of the computational mesh above the droplets, the deformation of the wall d_0 propagates into the volume, weighted with a *radial base function* (RBF).[11] Here, the Wendland function

$$\mathrm{W2}(\alpha) = \left(1 - \frac{\alpha}{r_{rbf}}\right)^4 \left(1 + 4\frac{\alpha}{r_{rbf}}\right) \tag{4.3}$$

is used. The radius $r_{rbf}^{+} = 65$ determines the maximum distance α up to which a specific surface deformation affects the volume mesh. Figure 4.5 shows W2 as a function of α/r_{rbf}.

The additional difference in the sizes of adjacent cells caused by the deformation is

$$\Delta h \simeq h^2 d_0 \frac{\mathrm{d}^2}{\mathrm{d}\alpha} \mathrm{W2} = \mathcal{O}(h^2), \tag{4.4}$$

thus preserving the second-order accuracy of the central differencing scheme given by equation (2.40).

Comparisons between these two variants of the cooled channel configuration, one with a smooth wall and one with condensate droplets, quantify the effect of condensation on turbulent flow and vice versa.

[11] Köthe et al., *Shape optimization of aircraft cabin ventilation components using adjoint CFD*, 2014.

Turbulent transport and condensation

The question of condensation in turbulent channel flow is intrinsically a question of transport mechanisms. The conditions necessary for the liquid–vapor phase transition are clear, as are the flow phenomena in isothermal and even differentially cooled turbulent channel flow. Condensation from humid air as it flows through the cooled channel exists at the intersection of both.

Aside from diffusion, it is the convective transport of heat and vapor that determines where and how much condensation occurs, and it is again the transport via the turbulent flow that carries the changes in temperature and concentration from the phase transition further along the channel.

DNS of the channel with and without condensation, and with and without condensate droplets, provides fully resolved data on the velocity, temperature, and concentration for the different configurations. Averaging these flow fields for $\Delta t^+ = 30$ ensures fully converged first and second statistical moments, which form the basis for the analysis of the interplay between turbulence and condensation.

Condensation mass flux

The evolution of the temperature and vapor concentration along the channel is the most immediate observable for the cooled inlet–outlet configuration. The normalized temperature is $\theta = (T - T_c)/\Delta T$, with values between 1 at the inlet and 0 at the cooled wall. For the concentration, $\zeta = (c - c_{sat}(T_c))/\Delta c$ is the analogous quantity.

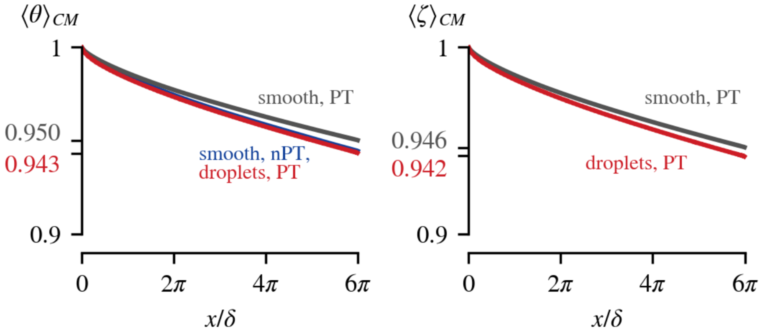

Figure 4.6: The fluid cools and dries as it passes through the cooled channel. The addition of droplets increases the heat and mass transfer compared to the smooth channel.

Figure 4.6 shows the progression of the *cup-mixing average* of θ in the left and of ζ in the right panel. The cup-mixing or *bulk average* along the streamwise direction is

$$\langle\theta\rangle_{CM} = \frac{\int \theta u_x \,\mathrm{d}y\mathrm{d}z}{\int u_x \,\mathrm{d}y\mathrm{d}z}, \tag{4.5}$$

for θ and identically defined for the dimensionless vapor concentration ζ.

As the warm, humid air passes through the channel, it transfers heat to the cooled wall. Simultaneously, condensation removes vapor from the fluid.

The temperature difference $\Delta\theta = 0.007$ between the smooth case with phase transition (PT) with an outlet value of $\langle\theta\rangle_{CM} = 0.943$ and without phase transition (nPT) with $\langle\theta\rangle_{CM} = 0.950$ corresponds to a decrease in the net transfer of sensible heat by 9 % for PT. This small difference shows that the isothermal surface very effectively removes the latent heat released during condensation.

The simulation with condensate droplets at the wall results in virtually identical outlet temperature compared to nPT, compensating the shift caused by the phase transition in the smooth channel.

The vapor concentration $\langle\zeta\rangle_{CM}$ exhibits the same increased transfer rate from the added droplets. The mean drying rate is 7.4 % higher compared to the smooth channel, increasing the deficit at the outlet from $1 - \langle\zeta\rangle_{CM} = 0.054$ to 0.058. This exceeds the increase of surface area of 6.4 % caused by the droplets, indicating an increase of the actual condensation mass flux.

The energy fluxes in the streamwise direction combine the contribution from sensible and latent heat. The sensible heat flux is

$$\phi_s = (T - T_c)\rho c_p u_b, \tag{4.6}$$

and the latent heat flux

$$\phi_l = (c - c_{sat})\rho_v h u_b, \tag{4.7}$$

where ρ_v is the density of pure vapor. Adding both contributions $\phi_s + \phi_l = \phi^*$ and normalizing analogous to the dimensionless temperature and concentration via

$$\phi = \frac{\phi^*(\theta,\zeta) - \phi^*(\theta = \zeta = 0)}{\phi^*(\theta = \zeta = 1) - \phi^*(\theta = \zeta = 0)} \tag{4.8}$$

gives the dimensionless total heat flux ϕ in the streamwise direction.

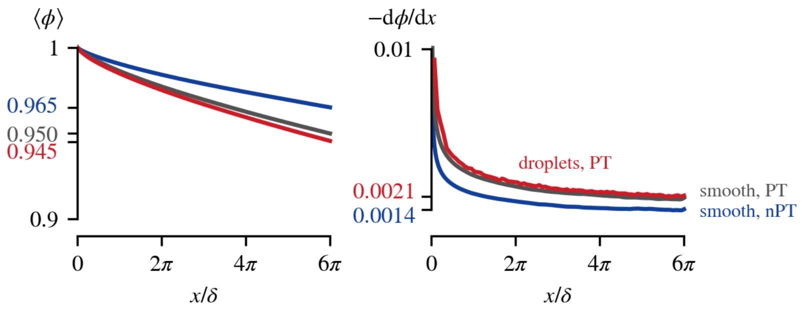

Figure 4.7: In cases with phase transition, 43% more energy is removed from the channel along its full length compared to nPT. The right panel shows the corresponding increase in the local transfer rate explicitly.

The left panel of figure 4.7 shows the evolution of ϕ along the channel.

As energy can either flow through the channel or the cooled wall, the deficit in the streamwise flux at a given downstream position compared to the inlet is equal to the integrated flux through the wall up to this location. The right panel shows the local energy transfer rate $-\mathrm{d}\phi/\mathrm{d}x$ directly.

Including condensation and thereby allowing the removal of latent heat from the flow increases the energy deficit at the outlet by 43 % from $1 - \langle\phi\rangle = 0.035$ to 0.050 compared to the case without phase transition. The presence of droplets at the cooled wall causes a further increase by 10 % over the smooth configuration, with 0.055 transferred through the wall in total.

The droplet effect is most pronounced near the inlet, where the droplets are largest. For all cases, the energy transfer through the wall is maximal at the inlet, drops rapidly along the first part of the channel and is almost constant near the outlet, at 20 % of the initial rate.

Inseparable from the energy transfer at the wall is the transfer of mass across the phase boundary. This mass transfer is the defining feature of humid air flow through a cooled channel. Figure 4.8 shows the instantaneous change in vapor concentration from condensation directly at the cooled wall.

Condensation rates are highest at the inlet, where the flow first encounters the cooled surface. After this initial region of high mass transfer, condensation continues along the full length of the channel. The spanwise direction exhibits inhomogeneous condensation rates as well, with a periodic pattern reminiscent of the streaks in the friction velocity caused by turbulent flow structures shown in figure 4.9.

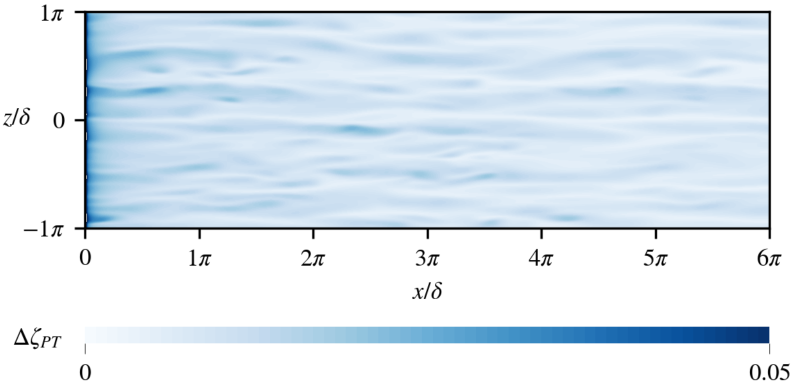

Figure 4.8: Condensation occurs across the complete cooled wall, but the transfer rate $\Delta\zeta_{PT}$ is inhomogeneous both along the streamwise and spanwise direction.

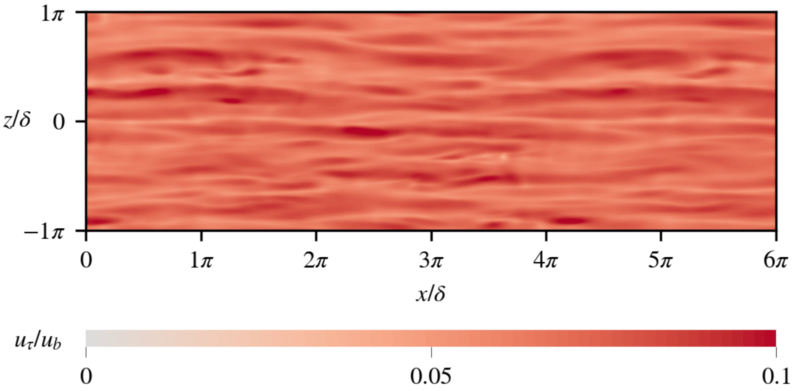

Figure 4.9: The instantaneous distribution of the friction velocity at the cooled wall shows patterns similar to the distribution of condensation rates.

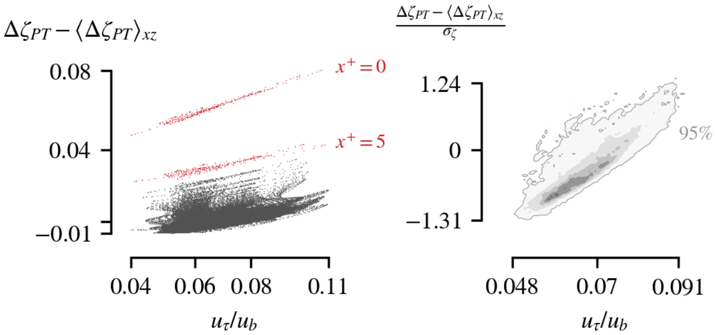

Figure 4.10: The bands within the raw data points in the left panel are the consequence of the global streamwise variation of the condensation rate. This influence masks the correlation with the friction velocity, shown in the two-dimensional histogram of the same data on the right.

Figure 4.10 illustrates the relationship between u_τ and the normalized mass transfer rate $\Delta\zeta_{PT}$ at the cooled wall. The condensation rates are centered with the average rate over the whole wall, $\langle\Delta\zeta_{PT}\rangle_{xz}$.

The right panel shows the correlation, quantified by the correlation coefficient $R = 0.47$, with

$$R_{xy} = \frac{\sum_i (x_i - \langle x\rangle)(y_i - \langle y\rangle)}{(n-1)s_x s_y}, \quad s_x,\, s_y \text{ standard deviations.} \tag{4.9}$$

The discrete bands visible in the visualization of all data points in the left panel are an artifact of the spatial discretization. Separate bands correspond to spanwise rows of grid cells at the wall. The first two bands, directly at the inlet and at $x^+ = 5$, are highlighted in red. The vertical separation of the bands results from the declining average condensation rate at increasing streamwise positions along the channel, as illustrated before in figure 4.6. As the overall vapor content decreases, the driving forces behind the condensation decrease as well, and the corresponding rates drop.

Due to the low Richardson number, $Ri = 0.01$, the velocity field does not reflect this streamwise progression of the scalar fields. Consequently, the correlation with the friction velocity cannot account for this effect either.

Centering the data with the spanwise average $\langle\Delta\zeta_{PT}\rangle_z$ instead of the global average $\langle\Delta\zeta_{PT}\rangle_{xz}$ removes the confounding effect of the declining condensation rates along the streamwise direction, leaving only the spanwise fluctuations. Figure 4.11 shows the collapse of the separate bands in the left panel and the resulting increased correlation of u_τ and $\Delta\zeta_{PT}$ on the right hand side. The correlation coefficient with respect to the spanwise variation alone is $R = 0.95$.

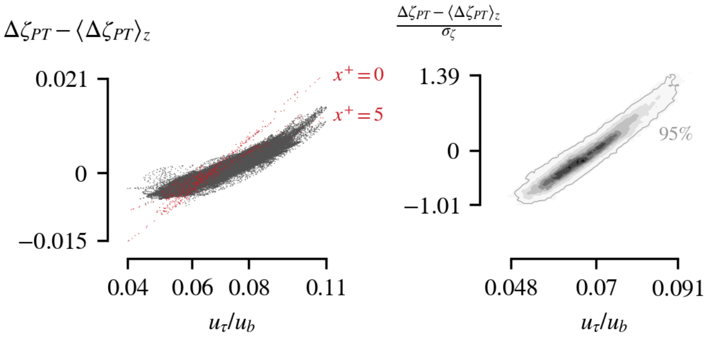

Figure 4.11: Compensating for the global streamwise variation collapses the bands present in the raw data and reveals the strong correlation between the friction velocity and the spanwise variation of the condensation rate.

This confirms a strong connection between the distribution of condensation at the wall and the underlying structure of the turbulent flow.

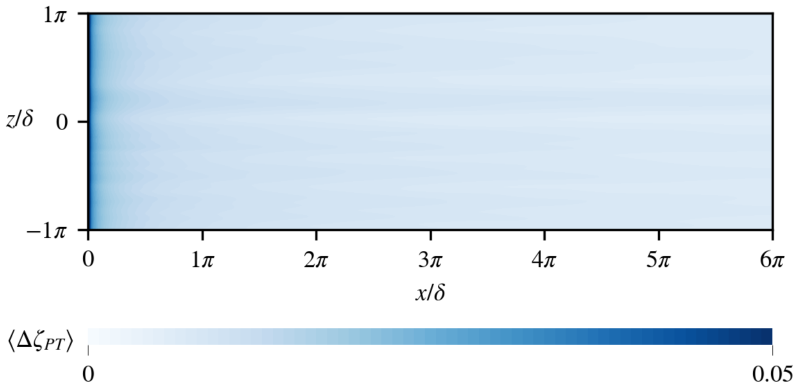

Figure 4.12: The accumulated condensate at the wall reflects the inhomogeneous condensation rates across the surface.

The distribution of condensate mass accumulated at the cooled wall reflects the spatial inhomogeneity of the instantaneous condensation rate. Figure 4.12 shows the time-averaged condensation rates that determine the accumulation over the long time scales associated with droplet growth. The periodic structure along the spanwise direction is less pronounced than in the instantaneous field, but still present.

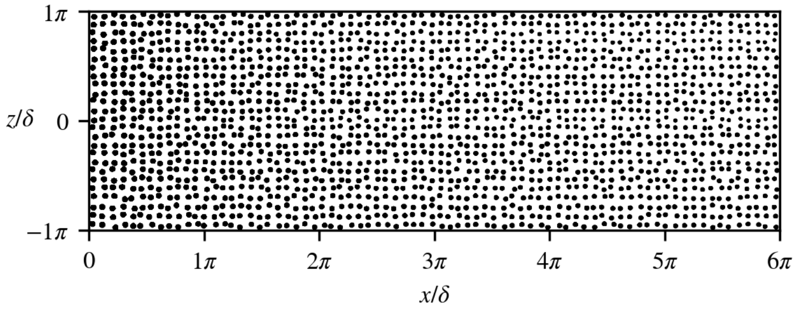

Figure 4.13: The pattern of 1900 droplets, placed according to the distribution of the average condensation rates found in the simulation of the smooth channel.

Figure 4.13 shows the droplet pattern resulting from this underlying pattern of the average condensation rate. Placing 1900 droplets across the channel wall, the relative droplet radii and heights reflect the locally available mass, as discussed in the previous chapter.

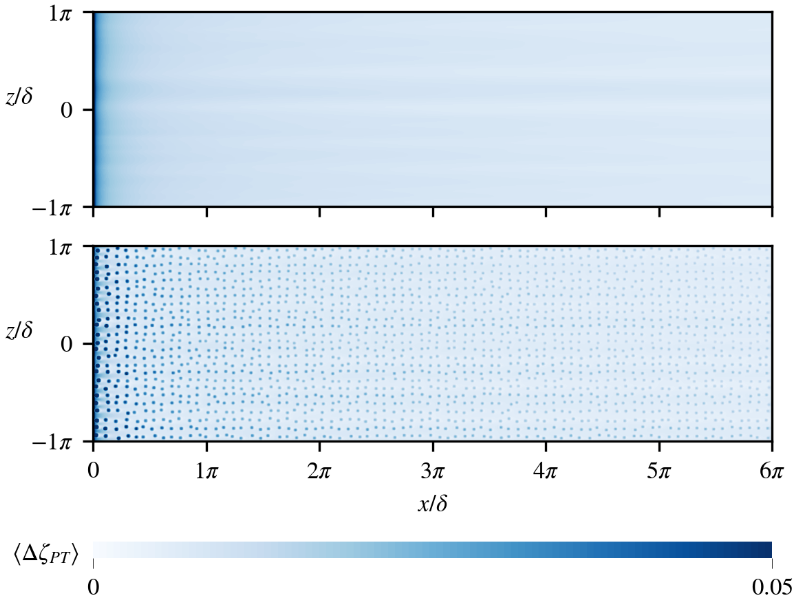

Figure 4.14: Comparison of the condensation rates for a smooth wall (top) and with droplets (bottom). The condensate droplets are favored sites for additional condensation.

The presence of these droplets significantly changes the distribution of the condensation rates at the cooled wall. Figure 4.14 shows the comparison with the smooth wall. Rates peak at the droplet sites along the whole channel. The spatial variation previously discussed for the smooth channel, with decreasing rates along the channel and periodic changes in the spanwise direction, is still visible, but the dominant effect comes from the increase of condensation directly at the droplets.

Droplet ensemble averaging

The existence of droplets at the cooled wall breaks the homogeneity of the channel geometry. In the vicinity of a droplet, the angle of the wall continuously changes with respect to the main flow direction, and the randomized pattern breaks the spanwise periodicity on length scales comparable to the droplet radii.

To investigate the mean flow fields in the direct vicinity of the droplets, averaging over the ensemble of all droplets removes the influence of the globally changing flow conditions from the cooling and drying of the air and retains the statistical advantage of spatial averaging on top of the temporal averages.

For this ensemble average, first, every surface point is assigned to its nearest droplet center. Figure 4.15 shows the resulting Voronoi diagram.[12] Every point within a Voronoi cell i is closer to the enclosed droplet center than to any of the surrounding droplet centers.

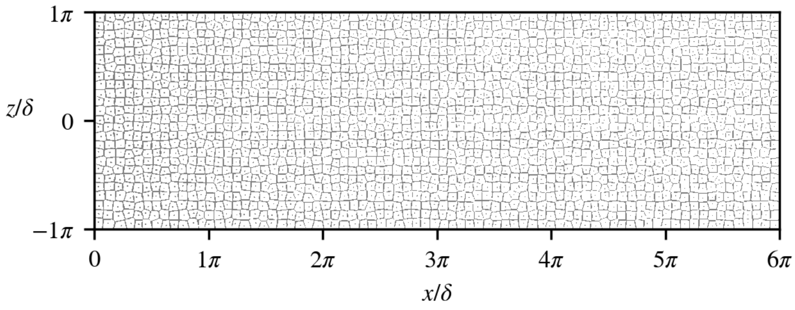

Figure 4.15: Each Voronoi cell contains all the surface points that are closer to the enclosed droplet center than to any other center.

The distance r_i from the droplet center and the angle φ_i with respect to the flow direction form a polar coordinate system within each cell i. In the immediate vicinity of the droplet, the droplet radius R_i provides a characteristic length scale. Scaling the distance r_i with this radius allows averaging of surface points across all Voronoi cells by mapping equivalent points to the same normalized coordinates.

[12] Aurenhammer and Klein, *Voronoi Diagrams*, 2000.

Figure 4.16 illustrates the construction and scaling of the polar coordinate system centered on the droplets.

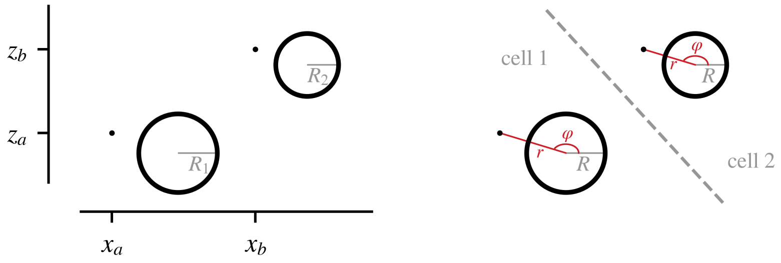

Figure 4.16: The polar coordinate system in the right panel describes the surface points *a* and *b* via the distance to the nearest droplet center and the angle with respect to the flow direction, compared to the cartesian coordinates *x* and *z* in the left panel. In this construction, the two points are at equivalent locations relative to their corresponding droplets.

Combined with the normalized measure for the condensation rates $\langle \Delta\zeta_{PT} \rangle$, this approach allows a detailed look into the microscopic effect of the droplets on the phase transition itself.

The ensemble average of the condensation rate over N droplets is

$$\langle \Delta\zeta_{PT} \rangle_N = \sum_N \langle \Delta\zeta_{PT} \rangle (r_i, \varphi_i). \tag{4.10}$$

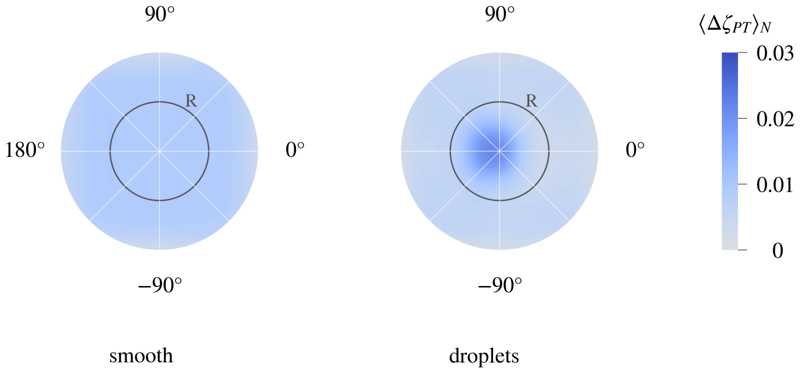

Figure 4.17: While condensation is homogeneous when looking at small regions of the smooth wall, the introduction of droplets causes a concentration of condensation on the droplets themselves.

Figure 4.17 shows these ensemble-averaged rates for the smooth channel on the left and with droplets on the right. The ensemble averaging for the smooth channel uses the same Voronoi decomposition obtained for the droplets for optimal comparability.

The circle at $r = R$ shows the droplet perimeter, and the flow direction is $\varphi = 0°$. For the small region with radius $2R$, condensation is homogeneous at the smooth wall. Including droplets leads to a shift of the condensation process onto the surface of the droplets themselves. The transfer rates are heightened directly on the droplet surface, particularly on the upwind flank, symmetrically around $\varphi = 180°$. In contrast, the lower downwind side with $r > R/2$ around $\varphi = 0°$ and the surrounding regions with $r > R$ show decreased condensation rates compared to the smooth wall. Figure 4.18 shows the difference between the condensation rates in the two panels of figure 4.17 explicitly.

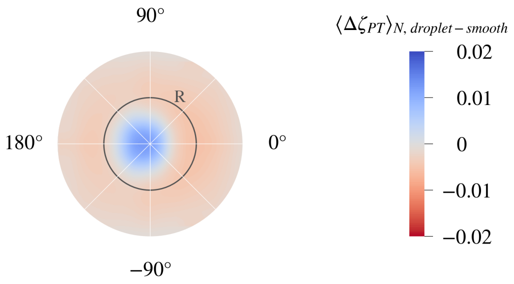

Figure 4.18: Averaged across all droplets, the deformation enhances condensation directly on the droplet surface, while reducing the transfer across the phase boundary in the surrounding regions.

The reason for this concentration of the condensation on the droplets is the modification of the flow fields in the vicinity of the droplets.

To perform ensemble averaging on these fields, the Voronoi decomposition is extended into the volume, and cylindrical coordinates replace the polar coordinates. Scaling the wall-normal coordinate y with the droplet height h_i again maps all droplet surfaces to same set of $(r_i,\, \varphi_i,\, y_{h,i})$. Consequently, equivalent points in the volume around a droplet are comparable for all droplets in the pattern. Figure 4.19 illustrates the new coordinate system in a wall-normal slice through two droplets with different radii and heights.

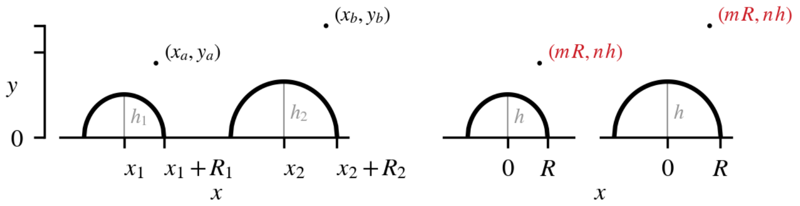

Figure 4.19: Two points in the volume surrounding different droplets become comparable when expressing their position with the appropriately scaled cylindrical coordinates.

Figure 4.21 shows the average streamwise and wall-normal velocity in the central xy-slice through the droplets. The color gradient of the droplet surface illustrates the distribution of the condensation rate, corresponding to a line from $\varphi = 180^\circ$ to $\varphi = 0^\circ$ in figure 4.17.

The droplets present obstacles to the flow, where the high streamwise velocity has a non-negligible component normal to the surface. The deflection of fluid at the droplet surface is clearly visible and coincides with the location of maximal condensation. Here, warm and humid fluid from the bulk impacts the droplet and supplies large amounts of vapor to the phase transition. Conversely, the mean flow is slower in the wake of the droplet, reducing the convective transport of humidity towards the wall.

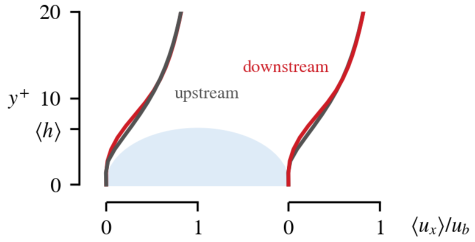

Figure 4.20: The flow obstacle presented by the droplet causes a velocity deficit on the downwind side.

Figure 4.20 shows the change of the ensemble-averaged streamwise velocity in the droplet wake more clearly by comparing the profiles at the upstream and downstream edge of the droplets. The mean velocity deficit integrated from the wall to $y^+ = 15$ is $\langle \Delta u_x \rangle_N / u_b = 0.023$, with a peak of 0.064 slightly above the mean crest height of the droplets at $y = 1.06 \langle h \rangle$.

This change of the convection in turn affects the temperature and vapor concentration around the droplets. The ensemble-averaged normalized temperature and velocity in figure 4.22 show how this modification of the flow diminishes the downstream transport of heat and humidity towards the wall, resulting in overall cooler and drier fluid. Thus, there is reduced potential for condensation, explaining the reduced rates shown in figure 4.17.

Condensation and turbulence directly interact in the wall-near region of the channel. Because of the importance of this region to the turbulent flow structures, they in turn propagate the effects into the overall flow of the channel.

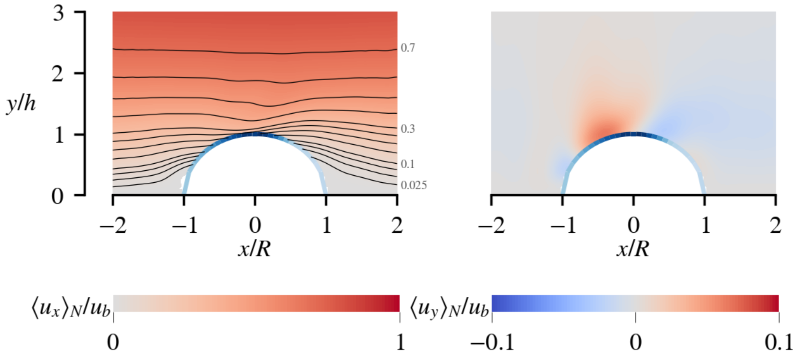

Figure 4.21: The streamwise (left panel) and wall-normal (right panel) ensemble-averaged velocity around the droplet shows fluid impacting on the upwind flank of the droplets, the subsequent deflection away from the wall, and the slow recovery of the flow in the wake region behind the droplet.

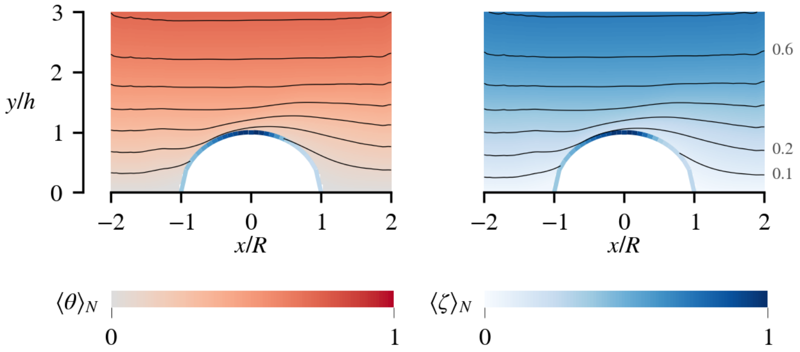

Figure 4.22: The ensemble-averaged temperature (left panel) and vapor concentration (right panel) show the depletion of warm and humid fluid in the lee of the droplet, reducing the potential for condensation.

Modifications of the overall flow fields

Condensation and the presence of droplets at the cooled wall affect the overall flow fields throughout the channel.

As convective transport of heat changes the temperature field, the changed buoyancy in turn modifies the the flow. With respect to the vapor concentration, the necessary conditions for condensation depend on the temperature, while the injection of latent heat into the fluid during the phase transition directly changes the temperature field at the condensation site.

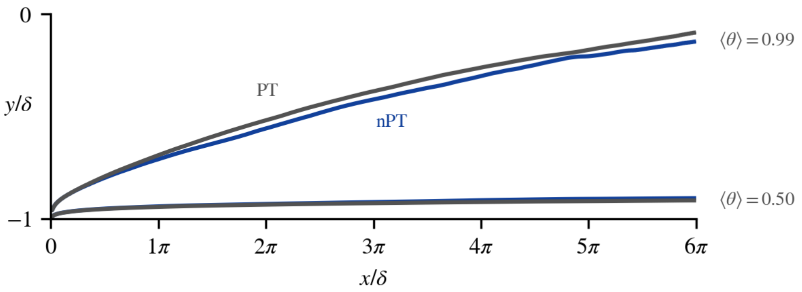

Figure 4.23: Condensation leads to increased thickness of the thermal boundary layer as described by the $\theta = 0.99$ isotherm.

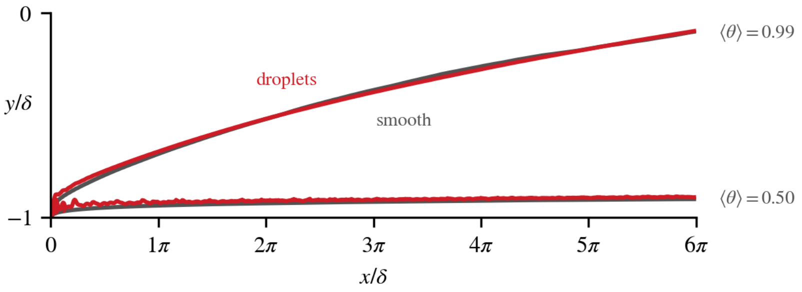

Figure 4.24: The presence of large condensate droplets near the inlet quickly broadens the thermal boundary layer, but the effect diminishes along the channel.

As such, the mean temperature field affords an initial look into the effects of condensation.

Figure 4.23 shows the isotherms of non-dimensional temperature for simulations with and without phase transition in the smooth channel, and figure 4.24 compares the results for channels with phase transition with and without droplets. $\langle\cdot\rangle$ denotes averaging in time as well as along the spanwise direction.

In both cases, the behavior near the cooled wall reflects the direct effect of condensation. The $\langle\theta\rangle = 0.50$ isotherm progresses closer to the wall for PT than for nPT, showing the steeper temperature gradient caused by the local heating of the fluid from the release of latent heat.

Similarly, the introduction of droplets into the flow lifts the $\langle\theta\rangle = 0.50$ isotherm away from the wall, a direct consequence of the small obstacles presented to the flow and the deformation of the temperature field around the droplets as shown in figure 4.22. The effect is particularly pronounced near the inlet, where the size of the droplets is large compared to the undisturbed thickness of the thermal boundary layer.

Further away from the wall, the temperature field shows the inverse behavior in the comparison between nPT and PT. Growing along the channel to almost the center of the channel, condensation increases the thickness of the thermal boundary layer given by the $\langle\theta\rangle = 0.99$ isotherm compared to nPT. Since this observation runs counter the direct effect of the heating of the fluid due to latent heat, it must instead be the result of a modification of the flow field changing the heat transfer in the channel.

As fluid cools down near the channel wall, an aiding buoyant force arises, accelerating the fluid along the main flow direction. In the case with phase transition, the drying of the fluid adds an additional solutal contribution to the buoyant force, acting in the same direction as the thermal buoyancy. However, the heating of the fluid from the release of latent heat opposes the cooling at the wall.

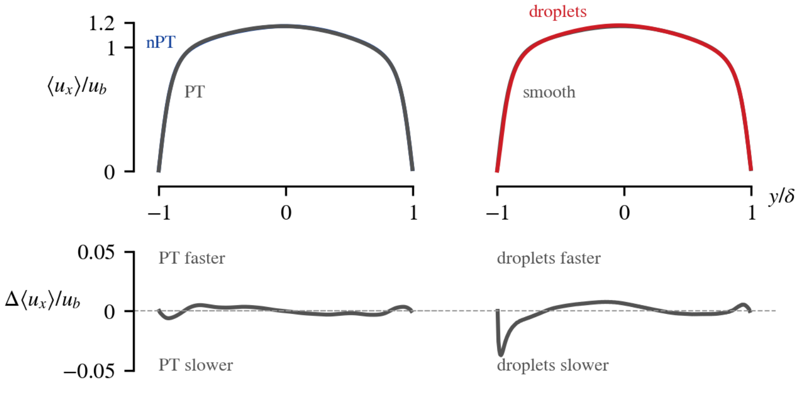

Figure 4.25: Condensation causes a slight reduction of the streamwise velocity near the cooled wall compared to nPT. Further adding condensate droplets has a much larger impact, slowing down the fluid considerably.

Figure 4.25 shows the wall-normal profiles of the mean streamwise velocity $\langle u_x\rangle$ at the outlet of the channel. Here, flow modifications due to buoyancy are most pronounced, as the fluid carries the effect of the buoyant forces accumulated along the whole channel.

Since the inertial forces far outweigh buoyancy at $Ri = 0.01$, the mean flow exhibits only small differences between the configurations, shown in the upper panels. The lower two panels of the figure show only the change between the cases on a more appropriate scale.

The comparison between nPT and PT in the left panels shows that condensation slows the fluid near the cooled wall. The added solutal buoyancy caused by a change in concentration $\Delta c'$ is $B_s = \beta_c \Delta c' g$, acting parallel to both gravity and the main flow direction. As the change in concentration is caused by condensation, an associated thermal buoyant force, $B_T = -\beta_T \Delta c' g h_v / c_p$, arises, acting in the opposite direction. The *leverage ratio*

$$L = B_T / B_s = -\frac{\beta_T}{\beta_c} \frac{h_v}{c_p} \tag{4.11}$$

between the solutal buoyancy from condensation and the thermal buoyancy from the released latent heat is an intrinsic property of the fluid. For humid air, this ratio is $L = -23$. This large and opposed leverage ratio means that the thermal buoyancy caused by the release of latent heat far outweighs the solutal contribution. Consequently, the net effect of condensation on the buoyant forces near the wall reduces the aiding force and therefore the overall acceleration of the fluid compared to nPT.

The opposing contribution of condensation to the aiding buoyant force causes only small changes to the mean flow profile, due to the small relative importance of the natural convection compared to the forced flow.

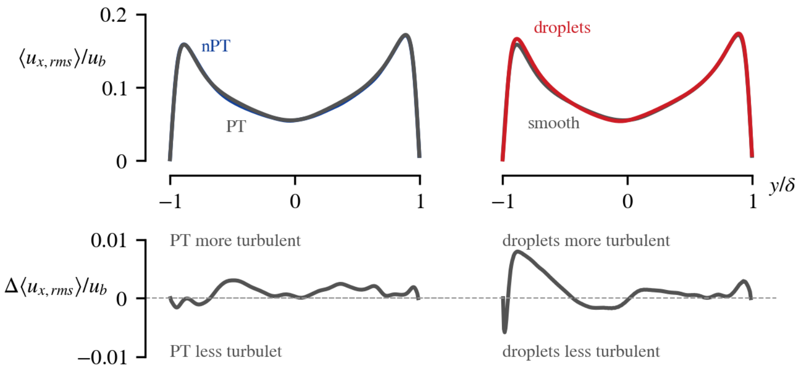

Figure 4.26: Condensation leads to an increase of the streamwise velocity fluctuations in the cooled half of the channel. The effect of condensate droplets is even stronger, with a dip in the immediate wake of the droplets and a significantly increased peak.

In contrast, the profiles of the root-mean-square of the velocity fluctuations in figure 4.26 show that condensation alone increases the fluctuations in the cooled half of the channel on the same order of magnitude as the addition of condensate droplets. The turbulent kinetic energy increases by 1.8 % due to the phase transition, and by 3.6 % from the addition of the droplets. The increased fluctuations in the smooth channel with condensation are a direct consequence of the decreased aiding buoyant force due to the leveraged thermal buoyancy. An accelerating force acting on the fluid damps turbulence. Compared to isothermal channel flow, the profile becomes asymmetric, with decreased velocity fluctuations near the aiding side. While the asymmetry is visible in figure 4.26, it is more readily visible in periodic channel flow such as shown in figure 3.6 for the differentially heated, periodic channel, reproduced here in figure 4.27.

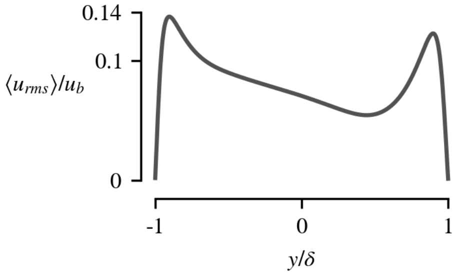

Figure 4.27: Aiding buoyancy at the channel wall at $y = -1$ reduces the intensity of the turbulence near that wall.

Since the net contribution of condensation to the buoyancy opposes the aiding buoyant force at the cooled wall, it effectively opposes the damping of turbulence as well. The increased turbulence intensity causes more mixing, carrying cool fluid further away from the wall and broadening the thermal boundary layer as seen in figure 4.23.

The right-hand panels of figure 4.25 show the effect of the condensate droplets on the mean streamwise velocity. Here, the change in $\langle u_x \rangle$ is a direct consequence of the rough wall. The fluid slows considerably near the rough wall, but the effect disappears towards the center of the channel. This is consistent with the wake region behind the droplets shown in figure 4.21.

The same is true for the effect of the droplets on the velocity fluctuations in the right-hand panels of figure 4.26. The effect of the droplets again comes from the direct interaction of the flow with the wall roughness. Figure 4.28 shows the ensemble-averaged velocity fluctuations around the droplets. The overall reduced flow velocities in the wake region cause a drop in the fluctuation intensity, while the interaction between turbulence and the upper parts of the droplets cause the subsequent peak.

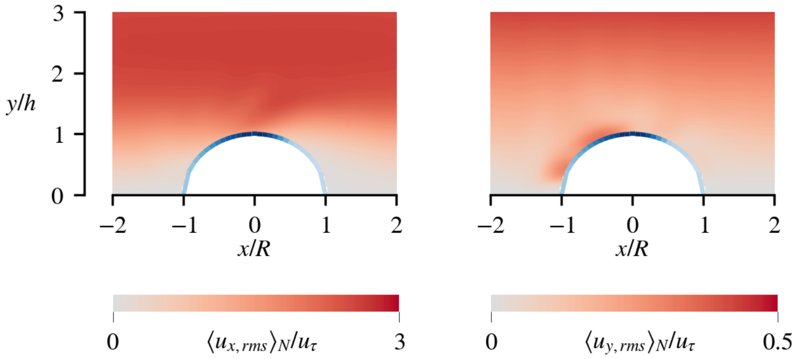

Figure 4.28: The flow across the curved droplet surface increases the fluctuations of both streamwise (left panel) and wall-normal velocity (right panel).

Conditional analysis based on fluid history

The sensitivity of the temperature field to changes of the velocity field visible both in the ensemble averages and in the global isotherms underlines the importance of convective transport processes concerning the redistribution of heat and humidity in the channel.

Selectively analyzing the transport processes towards and away from the cooled wall further illustrates the coupling between the velocity field and the active scalars.

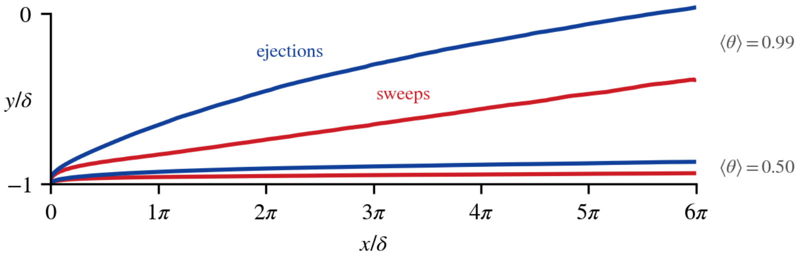

Figure 4.29: The conditionally averaged temperatures show that at a given wall distance, sweeps consist of warmer fluid compared to ejections.

Defining the criteria $u'_x = u_x - \langle u_x \rangle > 0$, $u_y < 0$ for a sweep and $u'_x < 0$, $u_y > 0$ for ejections and then sampling the temperature separately according to these conditions yields the average temperature of fluid transported within these turbulent flow structures.

Figure 4.29 shows the $\langle\theta\rangle = 0.50$ and 0.99 isocontours of the conditionally averaged temperature field in the smooth channel with condensation.

Sweeps move warm fluid from the bulk flow towards the wall. Heat transfer then happens by interaction of the fluid with the cooled wall, and ejections carry cooler fluid back towards the center of the channel.

The temperature difference between sweeps and ejections suggests that before interaction with the wall, the fluid temperature is equal or very close to the inlet temperature. Only after coming into close proximity to the cooled surface will the temperature drop significantly.

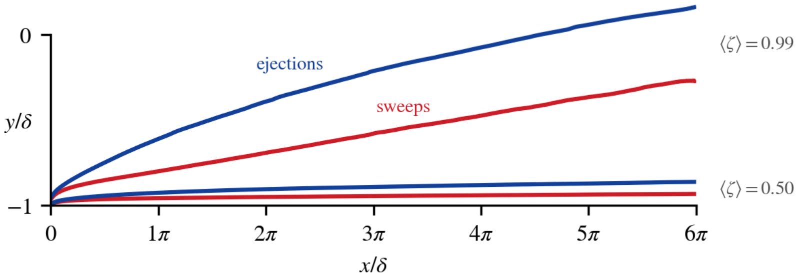

Figure 4.30: The average vapor content of sweeps is higher than that of ejections, similar to the result for the conditionally averaged temperature.

The same considerations apply to the vapor concentration field. The conditional sampling yields the average normalized vapor content in sweeps and ejections. Figure 4.30 again shows the isocontours of the conditionally averaged field in a smooth channel with condensation.

Significant changes in vapor content occur only after interaction with the cooled wall, where condensation reduces vapor from the humid air, and ejections subsequently carry dried fluid back into the bulk flow.

The overall behavior of the vapor concentration mirrors that of the temperature field. As $Sc = 0.65 \approx 0.73 = Pr$, diffusive transport of both quantities is similar, such that convective transport by the same flow results in almost identical distributions inside the channel.

This fundamental mechanism for the transport of the active scalar fields is driven by the intrinsic structure of the turbulent flow through the channel. The slight modifications of the fields result from the release of latent heat during condensation or the surface roughness due to condensate droplets. There is no additional effect visible in the conditionally averaged fields compared to those already discussed for the global temperature average.

Given these dynamics of cooling and drying of the humid air, the clear separation in both temperature and vapor content allows these scalars to serve as markers, distinguishing between fluid before and after interaction with the cooled wall. The global averages serve as the cut-off criteria:

$$\theta - \langle\theta\rangle \begin{cases} > \epsilon & \text{pre-interaction,} \\ < \epsilon & \text{post-interaction.} \end{cases} \tag{4.12}$$

for nPT and

$$\zeta - \langle\zeta\rangle \begin{cases} > \epsilon & \text{pre-interaction,} \\ < \epsilon & \text{post-interaction.} \end{cases} \tag{4.13}$$

for PT. Pre-interaction, θ and ζ will be close to the values prescribed at the channel inlet and above the global average, since the scalars are maximal at the inlet.

Conversely, as the global average reflects both pre- and post-interaction fluid, the values of temperature or vapor concentration in post-interaction fluid will necessarily be smaller. The threshold $\epsilon = 0.01$ improves the signal-to-noise ratio by removing small fluctuations around the average.

The coupling between temperature and vapor concentration via the release of latent heat means that while the temperature-based criterion (4.12) is appropriate in simulations without phase transition, it can not be used to distinguish between pre- and post-interaction fluid when condensation is possible. The temperature increase resulting from the injection of latent heat into the fluid creates a situation where the temperature of the fluid can momentarily increase during the interaction with the wall. Instead, ζ provides a clean probe in simulations with phase transition based on the criterion (4.13).

Separate averaging of the velocity of pre- and post-interaction fluid confirms the connection between sweeps and ejections and wall-normal transport of the scalar fields. Figure 4.31 shows profiles of the conditionally averaged streamwise and wall-normal velocity in a smooth channel with condensation.

From the construction of the criterion (4.13), the conditionally averaged velocity exists only inside the concentration boundary layer. Outside, the absence of humidity variation means that neither condition applies, while the definition of the boundary layer means that fluid further away from the wall is necessarily pre-interaction. Consequently, the profiles for pre-interaction fluid merge with the overall average velocity profiles at the $\zeta = 1 - \epsilon$ isocontour.

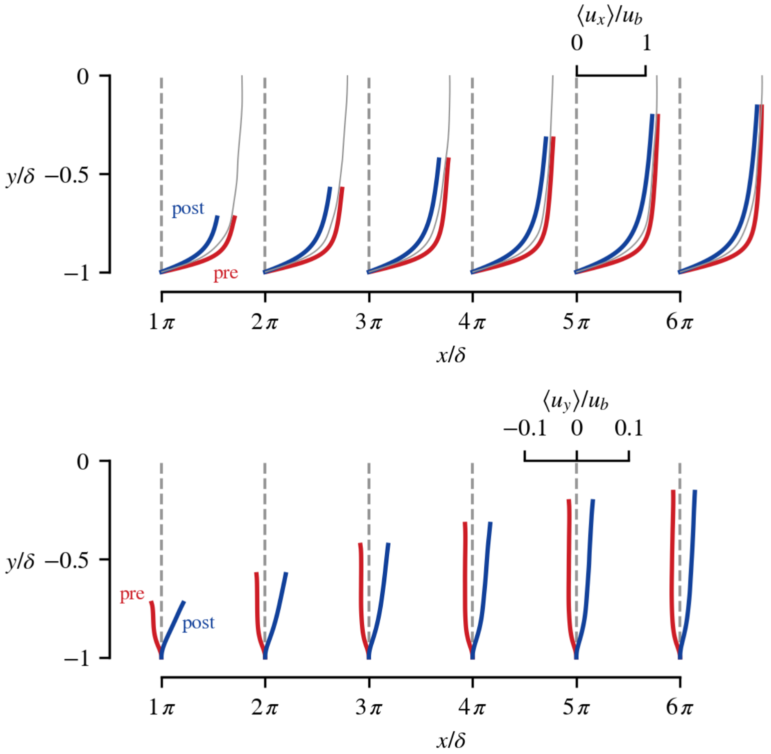

Figure 4.31: Pre-interaction fluid flows faster than the global average drawn in grey (top panel), and towards the wall (bottom panel), consistent with turbulent sweeps. After interaction with the wall, slower ejections transport the fluid back towards the centerline.

Pre-interaction fluid is faster than the overall average flow and directed towards the cooled wall, where it slows down and then returns to the bulk. This behavior exactly matches that of turbulent sweeps and ejections, complementing the conclusions from the sampling of temperature and vapor concentration specific to these structures discussed above.

Sweeps consist of pre-interaction fluid and are responsible for its transport towards the wall. In turn, ejections consist of post-interaction fluid and are responsible for propagating the cooling and drying effect of the wall further into the channel.

This connection between the sweeps and ejections and vapor transport is responsible for the spanwise pattern visible in the condensation rate at the cooled wall in figure 4.8. The structure of the turbulent flow imprints itself into the spatial structure of the phase transition via the transport of vapor to and from the wall.

The comparison between the conditionally averaged velocity profiles and the overall average shows the changing make-up of fluid inside the boundary layer. Near the inlet, pre-interaction fluid dominates the global average and both profiles are close together.

As the residence time of the fluid in the channel increases, the interaction probability increases alongside, and the global average near the wall tends more and more towards the profile for post-interaction fluid.

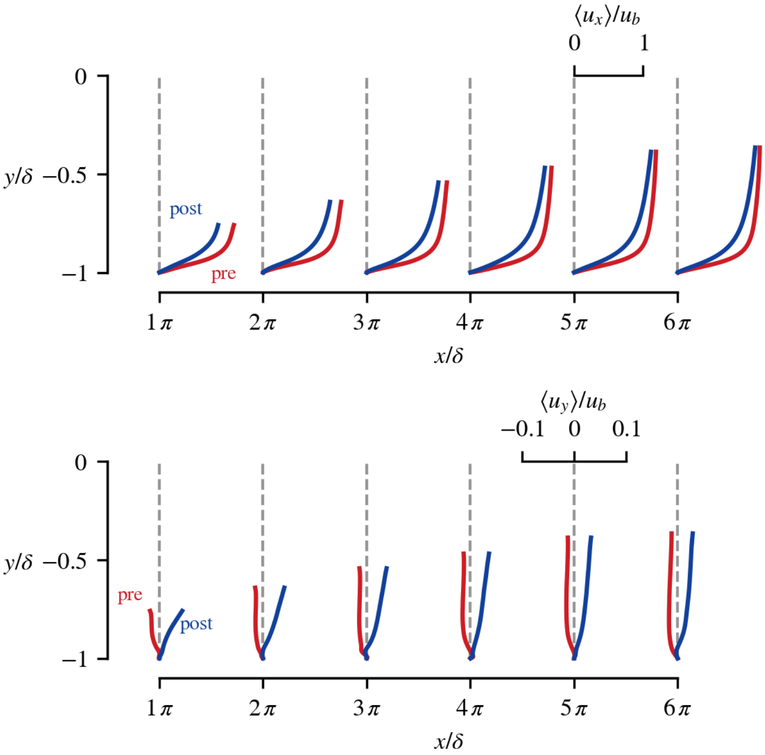

Figure 4.32: The conditionally averaged velocity profiles in simulations with condensate droplets show the exact same behavior as for the smooth wall.

The presence of condensate droplets leaves the connection between the wall-normal transport of humidity and the turbulent sweeps and ejections unchanged. Figure 4.32 shows identical behavior in the profiles for both the conditionally averaged streamwise and wall-normal velocity components as figure 4.31. This is consistent with the fact that the underlying mechanism of the sweeps and ejections does not change in the presence of a rough wall.[13]

Since effects from condensation only appear in post-interaction fluid, separate analysis can extract further results free from the masking influence of pre-interaction fluid.

[13] Grass, *Structural features of turbulent flow over smooth and rough boundaries*, 1971.

Sampling the fluctuations of the streamwise velocity in post-interaction fluid according to (4.13) allows the calculation of the turbulent energy spectrum as a function of the wavenumber $\boldsymbol{k}$ via

$$E_{xx}(\boldsymbol{k}) = \mathcal{F}(u'_x)\mathcal{F}^*(u'_x), \tag{4.14}$$

where $\mathcal{F}$ refers to the Fourier transform and the asterisk denotes the complex conjugate.

Pre-multiplying the spectrum with the dimensionless wavenumber $\boldsymbol{k}\delta$ and normalizing with the total energy,

$$E^*_{xx}(\boldsymbol{k}) = \frac{E_{xx}(\boldsymbol{k})}{\int E_{xx}(\boldsymbol{k})\,\mathrm{d}\boldsymbol{k}} \tag{4.15}$$

then yields the normalized energy content at a given wave number.

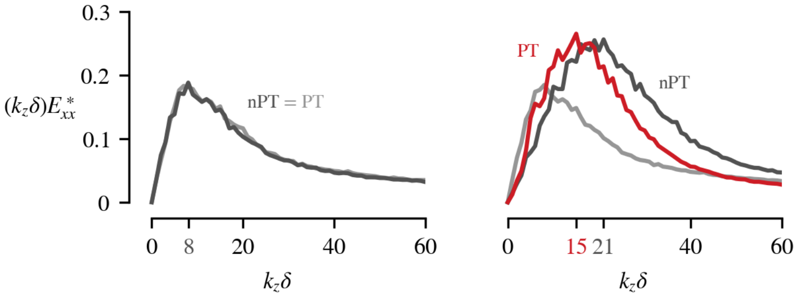

Figure 4.33: The pre-multiplied energy spectrum shifts towards higher spanwise wavenumbers between pre-interaction (left panel) and post-interaction fluid (right panel). Condensation reduces this shift, resulting in a peak at lower $k_z\delta$ compared to nPT.

Figure 4.33 shows these pre-multiplied spectra as a function of spanwise wave number for a wall-parallel plane at $y^+ = 15$. The spectra for pre-interaction fluid are identical between PT and nPT, with a peak at $k_z\delta = 8$ corresponding to a streak spacing of $\lambda_z^+ = 106$. After the interaction with the cooled wall, the peak of the spectra shift to higher wavenumbers, but the change $\Delta k_z\delta = 7$ for PT is only about half that of the change in nPT, $\Delta k_z\delta = 13$.

The reduced shift in the presence of condensation provides a clearer view on the resistance against the cooling of the fluid caused by the release of latent heat that was discussed above in the context of the velocity fluctuations of the whole fluid. As the interaction with the cooled wall shifts the spectrum to higher wavenumbers, the additional heat provided by the phase transition opposes the effect.

Conclusions

The results presented above show a close relationship between condensation and the wall-normal transport processes of the turbulent flow. Sweeps of warm and humid air impinging on the cooled wall determine the intensity of condensation at the surface, shown by the strong correlation between condensation rates and the footprint of the turbulent streaks. Selective sampling of ejections reveals their responsibility for carrying fluid back to the bulk after interaction with the walls.

Directly at the wall, the condensation rate determines the growth rate of condensate droplets. In turn, the changed wall topology influences the condensation rate. Averaged over the ensemble of droplets, condensation favors the droplet surface, leading to a positive feedback loop, where large droplets grow larger at a higher rate than small droplets.

The results show that a good understanding of the turbulent flow is necessary to predict condensation in the channel. For a sufficient set of predictors, only the effects feeding back from condensation to the turbulent flow have to be added. Here, the primary mechanism is the opposition of the leveraged thermal buoyancy caused by the release of latent heat during the phase transition. Acting against the primary influence of the cooled wall, it damps the effects compared to single-phase flow with differential cooling. Both the direct observation of the velocity fluctuations and the analysis of the post-interaction streak spacing show this resistance to the changes expected for a simple cooled wall.

Taken together, the results for both the dependence of condensation on the turbulent transport and the modification of this transport due to phase transition form a complete picture of the mutual interaction of turbulence and condensation.

5

Implications for condensation predictions

The objectives from chapter 1 guide the discussion of the results from the previous chapter. To recapitulate, these goals are:

- Creating an efficient and versatile approach to include phase transitions on top of a high-precision flow simulation,
- Identifying the primary transport mechanisms driving condensation on a cooled surface,
- Analyzing the effect of condensation on the overall flow, and
- Investigating positive and negative feed-back between flow and condensation.

The comparisons between DNS with and without condensation and with and without condensate droplets reveal the relevant parameters and mechanisms for condensation in mixed convection. This knowledge improves predictions of condensation in such flows, and might ultimately allow specific modifications of the passenger ventilation to reduce or avoid condensation in critical areas.

To directly address these objectives, this chapter:

- Evaluates the active scalar phase change model as a tool for simulating condensation in cooled channel flow,
- Discusses the influence factors at the intersection of condensation and turbulence and their application to the prediction of heat and mass transfer, and
- Provides a perspective for using the feed-back between flow and phase transition for condensation control.

Application of the active scalar model

The active scalar phase change model provides an approach to add phase transition effects on top of a single-phase simulation. By treating temperature and vapor concentration as interconnected active scalar fields, it includes specific, selected thermodynamic effects without the need to simulate a full second phase.

The coupling between temperature and vapor concentration via the phase change source terms and to the velocity field via the thermal and solutal buoyant forces connects the local change in concentration and the associated release of latent heat to the flow fields.

These active scalar fields allows the classification into pre- and post-interaction based on the momentary values of temperature or vapor concentration compared to the average. For an evolving flow in an aperiodic geometry, this provides a useful way to specifically extract the effects of cooling and phase transition from the overall flow.

The modifications of post-interaction flow in particular, for example in the comparison of the pre-multiplied energy spectra in figure 5.1, show that the active scalar approach is effective in modeling the influence of condensation on turbulent flow.

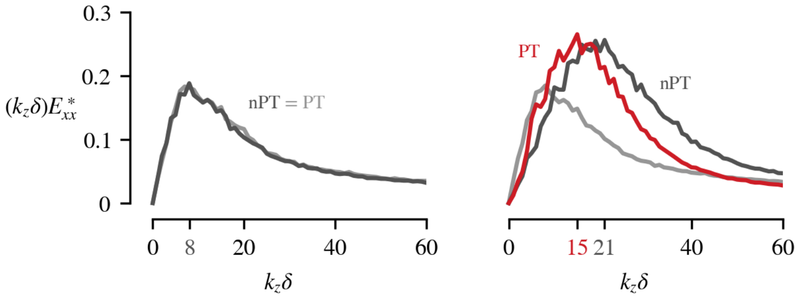

Figure 5.1: The phase change thermodynamics contained in the active scalar model cause the modification of the post-interaction structure of the turbulence.

With the underlying DNS, there are no confounding factors from models in the flow simulation. Any modification of the flow compared to the baseline without phase transition is due to the phase change model. However, the DNS is not integral to the phase change calculations themselves, allowing the combination of the active scalar approach with any time-resolved flow simulation.

The model performs best if the dynamics of the dispersed phase of liquid water are negligible compared to those of the carrier phase of humid air. At ambient conditions, where low absolute vapor content and moderate subcooling restrict condensation to the immediate vicinity of cooled surfaces, this assumption holds.

Figure 5.2 shows the comparison between the active scalar model and a two-way coupled multi-phase DNS with dispersed droplet.[1] The dimensionless temperature results of the active scalar model are within 0.05 across the central 94 % of the channel. Only for the shaded wall-near regions where the droplet concentration in the volume becomes non-negligible does the discrepancy increase up to 0.09. Even here, where conditions are maximally unfavorable for the active scalar approach, it still captures 77 % of the temperature shift between the baseline and the multi-phase DNS. In comparison, a DNS including inert particles, but no phase change, only accounts for 41 %.

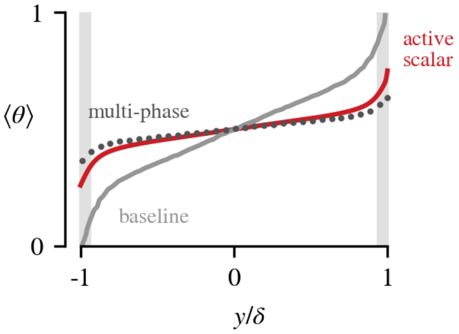

Figure 5.2: Large concentrations of dispersed droplets near the walls reduce the accuracy of the active scalar phase change model compared to a two-way coupled multi-phase DNS.

While the simulations in chapter 4 only include the release and absorption of latent heat as well as the solutal buoyancy as explicit results of the phase transition, additional phenomena can be included in the active scalar condensation model.

One of these effects is the modification of the phase transition mass flux due to the curved liquid–gas interface at the surface of condensate droplets. The radius of static, sessile droplets at the cooled wall is known and constant. Together with the Kelvin equation,[2]

$$\Delta T_{dew} = \frac{2\sigma T_{sat}}{\rho_l h_v R}, \tag{5.1}$$

this allows the calculation of the modified phase transition source term (3.8), taking into account the increased saturation pressure corresponding to the decreased dew point.

[1] Russo et al., *Water droplet condensation and evaporation in turbulent channel flow*, 2014.

[2] Rose, *Dropwise condensation theory and experiment: A review*, 2002.

Evaluation of the active scalar model

The active scalar phase change model is a viable approach to including phase transition effects in a single-phase DNS.

The application of the model in the investigation of the interaction between condensation and turbulent channel flow confirms it as a reliable and efficient approach to the simulation of condensation for ventilation applications.

Treating humidity as an active scalar coupled to the temperature and velocity fields means that computational costs are only marginally increased compared to single-phase DNS of differentially cooled flows.

The model closely reproduces results from two-way coupled multiphase DNS of dispersed droplets in channel flow with condensation and evaporation. In setups with primarily surface condensation, the reliability of the results is even higher due to the negligible effects of droplets in the fluid volume.

The model is flexible in its connection to the underlying flow simulation, allowing the inclusion of more or different aspects of phase transitions as the specific applications demand.

Interactions between condensation and turbulence

The results of the DNS for cooled channel flow with phase transitions show a strong connection between the convective transport processes and condensation. In particular the wall-normal transport via turbulent sweeps directly determines the most active condensation sites.

In turn, this means that to accurately predict condensation, all parameters that influence the flow and turbulence need to be considered.

Reynolds number influence

The total amount of condensation scales with the residence time of the humid air over the cooled surface. The thermal and concentration boundary layers grow along the channel, allowing more and more vapor to condense.

Using the thermal channel length $L_{th} = x/(\delta Re Pr)$ normalizes the streamwise coordinate with respect to the effect of the reduced residence time for faster flows, as well as the influence of faster or slower conduction of heat inside the fluid.[3] This scaling makes the

[3] Eldridge, *Parallel Plate Heat Transfer*, 2014.

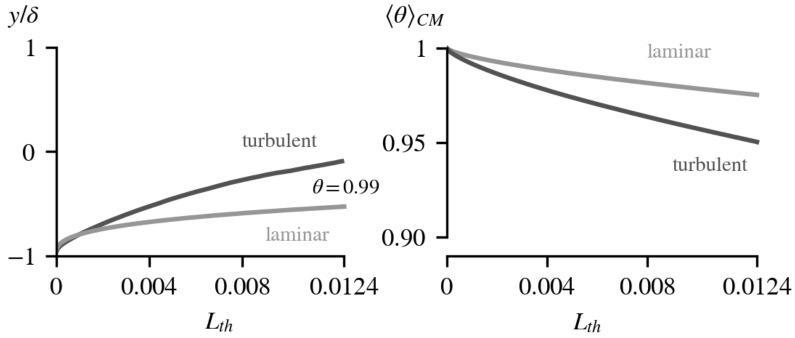

Figure 5.3: As the thermal boundary layer grows with the normalized thermal length, the bulk temperature decreases accordingly.

heat transfer comparable across different channel lengths, flow rates, and fluid properties, as long as the overall flow regime is the same. Between laminar and turbulent channel flow, there are qualitative differences beyond the simple normalization with the Reynolds number.

Figure 5.3 illustrates the growth of the thermal boundary layer and the bulk average temperature in the turbulent channel from DNS and the analytical solution for a theoretical laminar flow.

The $\langle\theta\rangle = 0.99$ isotherm grows with $L_{th}^{1/3}$ in laminar conditions, resulting in a $L_{th}^{2/3}$ dependence for $1 - \langle\theta\rangle_{CM}$ along the channel.

For turbulent flow, the boundary layer growth is closer to $L_{th}^{1/2}$, but not precisely described by a simple power law. The faster growth leads to the faster cooling at equivalent L_{th} shown in the right-hand panel.

Taking into account the dynamics within the flow itself, the transport of vapor towards the cooled wall depends on the turbulent mixing in the flow, again with the bulk Reynolds number as the characteristic quantity.[4] In addition to the global effect of the turbulence intensity on condensation, the friction Reynolds number determines the scales of turbulent channel flow and consequently the spacing of high- and low-speed streaks, with $\lambda_z^+ \simeq 100$. The connection between turbulent transport and condensation causes similar periodicity for regions of increased and decreased condensation. Figure 5.4 shows this periodic structure of the instantaneous condensation rates at the cooled wall along the spanwise direction.

[4] Eimann et al., *Convective dropwise condensation out of humid air inside a horizontal channel – Experimental investigation of the condensate heat transfer resistance*, 2018.

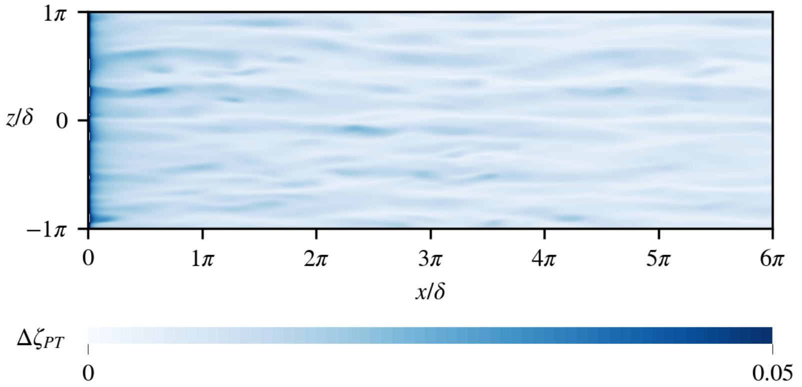

Figure 5.4: The connection of condensation to the wall-normal transport by the turbulent sweeps imprints the streak structure and its spanwise periodicity onto the instantaneous condensation rates shown here.

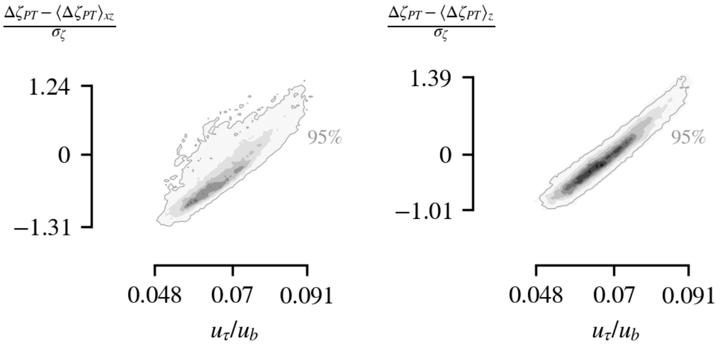

Figure 5.5: Removing the streamwise variation from the condensation rate at the wall increases the correlation with the friction velocity by isolating the spanwise variation (right panel), compared to the correlation with the untouched rates (left panel).

The strong correlation between the streak structure and condensation as shown in figure 5.5 means that the variation in the friction velocity determines the variation in phase change intensity. Removing the streamwise evolution of the vapor concentration results in near perfect correlation with $R = 0.95$, illustrated by in the right panel.

Together, the Reynolds number influences both the global amount of condensation across the whole channel as well as the local distribution at the wall.

Buoyancy and condensation

Since condensation necessitates subcooling and therefore a temperature difference, thermal buoyancy is a part of any flow with phase transition. Alongside this thermal contribution, the change in vapor concentration changes the density of the mixture of vapor and air, causing solutal buoyancy.

The role of aiding and opposing buoyant forces in differentially heated vertical channel flow is a well-studied phenomenon.[5] On one hand, buoyancy accelerates and decelerates the mean flow, respectively. The resulting velocity profile is asymmetric, biased towards the aiding side of the channel.

This asymmetry increases the friction velocity at the wall of the aiding side, changing the friction Reynolds number and therefore the flow structure as discussed above. On a global level, the change in mean flow near the cooled surface changes the replenishment of vapor near the wall. Consequently, acceleration near the cooled wall increases condensation, and vice versa for deceleration by opposing buoyancy.

Additionally, the aiding and opposing forces affect the turbulence of the flow. As turbulent transport redistributes warm and cold fluid within the channel, the aiding buoyancy at the cooled wall reduces the relative velocity between impinging sweeps and adjacent, slow-moving streaks. This reduces the interaction between the turbulent flow structures and damps the velocity fluctuations.[6] With respect to condensation, this means that aiding flow decreases the wall-normal turbulent transport of vapor, reducing condensation.

When compared to isothermal flow, the modifications of the mean velocity and its turbulent fluctuations at the same Reynolds number scale with the Grashof number, leading to an overall dependence on the Richardson number, $Ri = Gr/Re^2$. Figure 5.6 shows these changes in the mean streamwise velocity and the associated fluctuations in a differentially heated periodic channel.[7] Both phenomena scale with the relative influence of buoyancy on the flow.

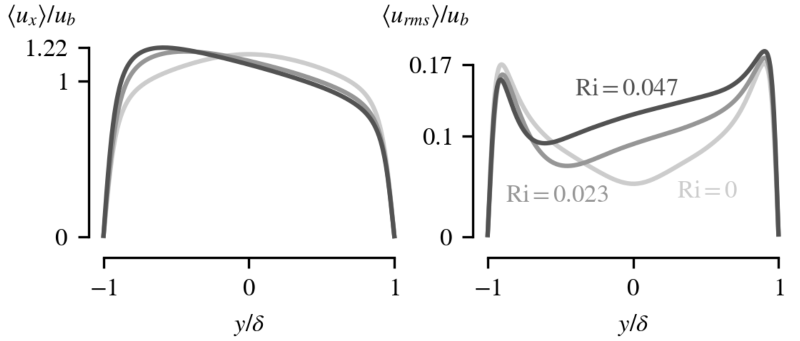

Figure 5.6: As Ri increases, the higher flow velocity from the aiding force at $y/\delta = -1$ (left panel) goes along with reduced velocity fluctuations, shown on the right.

These two effects act opposed to each other. For sufficient subcooling, condensation is fast compared to the convective transport of vapor.

[5] Kasagi and Nishimura, *Direct numerical simulation of combined forced and natural turbulent convection in a vertical plane channel*, 1997.

[6] Wetzel and Wagner, *Buoyancy-induced effects on large-scale motions in differentially heated vertical channel flows studied in direct numerical simulations*, 2019.

[7] Bahavar and Wagner, *Direct Numerical Simulation of Convective Turbulent Channel Flow of Fluid Mixtures*, 2019.

In this case, the availability of vapor dominates the phase transition rates, and aiding buoyancy increases condensation due to the increased global convective flux of vapor near the cooled wall. Accounting for this influence of natural convection increases the accuracy of models predicting the heat and mass transfer across the phase boundary.[8]

Apart from the buoyant forces from the temperature difference between the fluid and the external cooling of the channel, both the changing vapor concentration and the release and absorption of latent heat during condensation cause local density changes and, consequently, buoyancy.

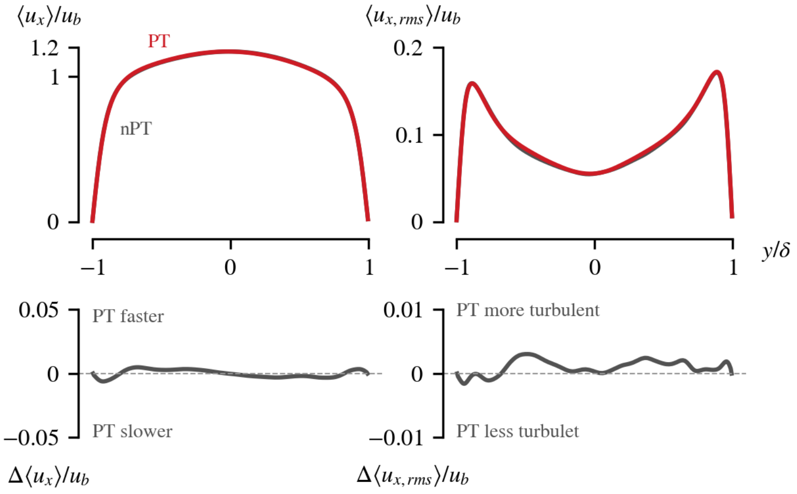

Figure 5.7: The released latent heat partially counteracts the buoyancy caused by the cooling at the wall. This results in less acceleration of the flow near the cooled wall (left panels), along with less damping of the velocity fluctuations (right panel).

Figure 5.7 shows the effect of this buoyancy contribution on the mean streamwise velocity and the associated fluctuations. With condensation, the flow near the wall is slower, and more turbulent throughout the channel. Because of the negative leverage ratio (4.11) of $L = -23$ for humid air, the buoyancy due to the temperature change from the release of latent heat acts opposite to the buoyancy from the drying of the fluid. With $|L| \gg 1$, this thermal contribution outweighs the solutal buoyancy. The resulting opposing buoyant force reduces the overall aiding buoyancy at the cooled wall.

Consequently, there is less damping of the turbulence, and turbulent kinetic energy increases by 1.8 % over nPT.

Constructing the Grashof number for this process using $\Delta T = \Delta c\, h_v / c_p$ gives

$$Gr_{PT} = 34\,500 = |L|\, Gr_c, \tag{5.2}$$

[8] Brückner et al., *Modelling of Heat Transfer for Droplet Condensation in Mixed Convective Duct Flow*, 2021.

similar in magnitude to $Gr_T = 38\,000$.

Even though this potential buoyancy contribution is comparable to that of the cooled wall itself, the overall effect on the flow visible in figure 5.7 is small. If the maximum heat flux at the cooled wall is large compared to the released latent heat, the cooling quickly removes the released latent heat from the channel, and no large-scale motion develops.

For a perfectly isothermal wall, the natural convection caused by the phase transition itself only slightly damps the overall buoyancy from the global cooling of the channel.

However, in situations where the local heat flux from the release of latent heat overcomes the heat flux at the cooled wall, this correction becomes significant to the total influence of buoyancy on the flow. Including this correction in a model would then be essential for accurate predictions of heat and mass transfer.

Roughness from condensate droplets

The condensate droplets on the cooled surface have the largest impact on the flow fields of all phase transition effects investigated here.

An immediate effect of the droplets is the effective increase of cooled surface area at the channel wall. Assuming constant heat flux, this results in a proportional increase of the heat transfer out of the fluid. For hemispherical droplets, the ratio between the wetted area and the new, curved surface is 2, meaning that individually, the largest droplets contribute most to the overall surface increase. However, as there are many more smaller than larger droplets, their overall contribution is significant. Including only the largest droplets in the simulation accounts for the a part of this effect. The presence of additional smaller droplets in-between the larger ones would further increase the cooling surface.

Constraining the generation algorithm for the droplet pattern such that the resulting droplet distribution satisfies a realistic size distribution,[9]

$$N(r) = \frac{1}{3\pi r^2 R_{max}} \left(\frac{r}{R_{max}} \right)^{-2/3}, \qquad (5.3)$$

in addition to local mass conservation would allow precise estimation of the additional surface not accounted for in the simulated pattern.

[9] Le Fevre and Rose, *A theory of heat transfer by dropwise condensation*, 1966.

Figure 5.8 shows the comparison between these two size distributions. The total number of droplets is the same, as is the resulting mean radius, but while the simulated distribution on the left peaks near this mean value and drops for larger and smaller droplet sizes, the theoretical distribution on the right reflects the power law given by (5.3).

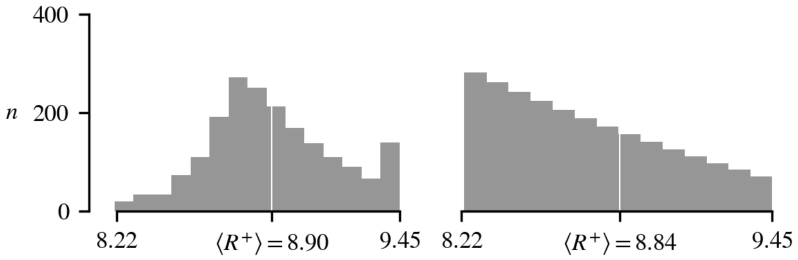

Figure 5.8: The theoretical distribution of the droplet radii shown on the right follows a power law with exponent $-2/3$, instead of of the approximately symmetrical distribution generated by the grid-based algorithm on the left.

In addition to the increased wall surface, the droplets at the cooled surface transform the channel as a whole into a channel with a rough wall.

For fully developed rough channel flow, the dimensionless velocity in the log-law region differs from the smooth case of (2.31) by[10]

$$\Delta u^+ = \frac{1}{\kappa_{vK}} \log k_s^+ + B - C, \tag{5.4}$$

where $B = 5.2$ as in the original law of the wall and $C \approx 8.5$. k_s^+ is the *equivalent sand roughness* — the the length scale of sand grains that would create the same velocity shift when covering the channel walls.

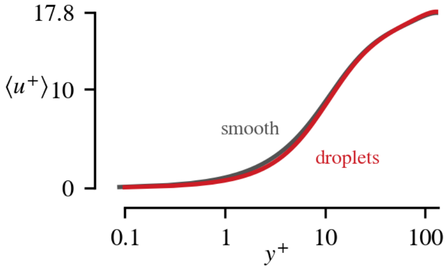

Figure 5.9: The velocity drops directly above the droplet peaks when compared to a smooth surface, but the shift does not reach into the logarithmic region.

Figure 5.9 shows the profiles of the average dimensionless velocity with and without droplets.

At wall distances on the order of the droplet heights, there is a clear reduction of the streamwise velocity, but the difference diminishes towards the channel centerline. Critically, the velocity shift in the log-law region expected from (5.4) does not exist.

[10] Krogstad et al., *An experimental and numerical study of channel flow with rough walls*, 2005.

Because of the relatively low Reynolds number in this investigation, there is no clear separation of the log-law region and the outer layer. The overlap of the scales means that outside of the buffer layer, the flow already starts to behave independently of the conditions at the wall, removing the influence of the roughness. Additionally, the flow through the inlet–outlet geometry is not fully developed rough channel flow, as the droplets are not present in the precursor domain.

For longer channels or at higher Reynolds numbers, the overall effect of the surface roughness on the phase transition follows the same arguments as for the buoyancy: Due to the strong coupling between convective transport of humidity and condensation, any modification of the velocity field affects the condensation rates. On a global scale, for the streamwise velocity, reduced flow velocities as predicted by (5.4) lead to less available vapor, but at the same time increase the residence time and provide additional opportunity for condensation.

Near the wall, the length scale of the droplets is similar or larger than the length scales of the flow. The obstacles presented by the droplets reaching out of the viscous sublayer interact with the mean flow as well as with the individual flow structures. This interaction leads to increased velocity fluctuations, as the droplets deflect fluid upwards, redistributing kinetic energy between the streamwise and wall-normal component. Overall, the turbulent kinetic energy increases by 3.6 % compared to the smooth case.

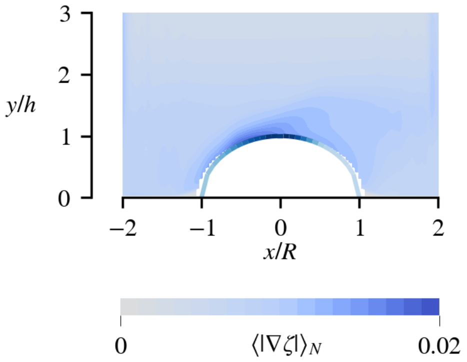

Figure 5.10: The droplets change the flow in a way that increases the concentration gradients at the upwind flank and the crest of the droplets, increasing condensation and depleting the vapor in the wake.

The droplets completely break the uniformity of the surface. Figure 5.10 shows the asymmetry of the ensemble-averaged concentration gradient around the droplets. Impacting on the upwind flank of the droplets, the turbulent sweeps deposit greater amounts of vapor at the droplet surface compared to the smooth wall. The strong mixing steepens the concentration gradients and leads to peak condensation slightly in front of the droplet crests.

In the recovery region in the wake of the droplets, the combination of reduced wall-normal transport and the high condensation activity immediately upstream reduces the available vapor, inhibiting condensation on the downwind flank and in close vicinity around a droplet.

This concentration of the phase transition on the surface of existing droplets leads to accelerated growth of larger droplets at the expense of smaller droplets. The effect mimics the phenomenon of *Ostwald ripening*.[11] In this case, condensation favors larger droplets due to the smaller curvature and consequently lower vapor pressure, as shown by the Kelvin equation (5.1).

Because the DNS with the active scalar model does not include this purely thermodynamic phenomenon, it instead reveals how fluid mechanics cause a similar effect. The modification of the flow field and associated vapor transport towards the wall alone further increase the tendency for the largest droplets to grow faster still.

The interplay between condensation and turbulence

Summarizing the discussion above, the investigation of turbulent channel flow with condensation identified a strong connection between condensation and turbulent flow structures.

The correlation between turbulent sweeps and the condensation intensity at the wall is so strong that the structure of the sweeps in form of the friction velocity streaks is sufficient to completely predict the spanwise variation of the condensation.

Inversely, the large amount of latent heat released during condensation causes a significant buoyancy contribution acting on the flow. Overall, the heat transferred across the cooled wall increases by 50 %. In the specific downward-flowing setup discussed here, the additional buoyancy partially counteracts the buoyancy caused by the cooled wall, increasing the turbulence intensity by reducing the damping effect.

Condensate droplets have an even larger effect on the flow. They markedly increase the turbulence in the channel due to the surface roughness introduced at the wall.

[11] Madras and McCoy, *Distribution kinetics theory of Ostwald ripening*, 2001.

Condensation control

The discussion above reveals the following influence factors for controlling condensation in turbulent mixed convection:

First, the supply of vapor via convective transport determines the amount of condensation. Consequently, any change to the global convective flow directly impacts the phase transition and the accumulation of condensate.

The solutal and thermal buoyant forces act directly on the mean velocity field. Importantly, the connection between a deceleration along the main flow direction and an increase in turbulence and therefore wall-normal mixing means that an opposing buoyant force reduces the vapor flux along the main flow direction, but increases the amount of vapor available in the subcooled region near the cool surface.

During condensation, the parallel cooling and drying of the humid air results in parallel buoyancy contributions. However, the leveraged thermal buoyancy from the released latent heat acts in the opposite direction.

Condensation and buoyancy form a negative feed-back loop: If the primary solutal and thermal buoyancy favor condensation, the leveraged buoyant force attenuates the effect, and vice versa.

Second, the interaction between flow, condensation, and condensate droplets creates an additional feed-back loop. The droplets present obstacles to the flow of humid air and increase the wall-normal transport of heat and vapor. Droplets grow largest where the condensation rates are high, and the changed flow around large droplets causes additional condensation at the droplet surfaces. On top of that, the depletion of available vapor in the wake of the droplets further concentrates condensation at the surface of already existing droplets. Consequently, this is a positive feed-back loop: Condensation favors droplet growth, and large droplets favor condensation. Further considering Ostwald ripening adds to the favorable conditions for condensation on larger droplets.

Potential control of the amount or specific location of condensation inside a passenger compartments will need to take these mechanisms into account. Critically, the buoyancy interaction is always active, while the interaction with the droplets becomes significant only after the droplets reach sufficient height from the surface.

Both the positive and the negative feed-back loop provide opportunities for condensation control.

Accepting that condensation in general is inevitable and promoting condensation and condensate accumulation at specific surfaces can utilize the positive feed-back mechanism originating from the condensate droplets, concentrating further condensation in the same area and away from critical surfaces.

In contrast, adjusting the balance between the buoyancy of the cooling and drying air, the leveraged buoyancy from the latent heat of condensation, and the convection inside the passenger compartment can limit the potential for runaway accumulation of condensate before the formation of macroscopic droplets.

The direct numerical simulations with the active scalar phase change model allowed the identification of these interactions between condensation and turbulent channel flow.

Based on the results of this investigation, future work using a variety of different numerical and experimental approaches can give more specific insight into the possibilities for condensation control in passenger compartments.

Bibliography

Alduchov, Oleg A. and Robert E. Eskridge

1996 Improved Magnus Form Approximation of Saturation Vapor Pressure, *Journal of Applied Meteorology*, 35, 4 (Apr. 1996), pp. 601–609, DOI: `10.1175/1520-0450(1996)035<0601:imfaos>2.0.co;2`.

Aurenhammer, Franz and Rolf Klein

2000 Voronoi Diagrams, *Handbook of computational geometry*, 5, 10, pp. 201–290.

Bahavar, Philipp and Claus Wagner

2017 Direct Numerical Simulation of Convective Channel Flow with Temperature and Concentration Gradients, in *Notes on Numerical Fluid Mechanics and Multidisciplinary Design*, Springer International Publishing, pp. 445–453, DOI: `10.1007/978-3-319-64519-3_40`.

2019 Direct Numerical Simulation of Convective Turbulent Channel Flow of Fluid Mixtures, in *Direct and Large Eddy Simulations XI*, ed. by Maria Vittoria Salvetti, Vincenzo Armenio, Jochen Fröhlich, Bernard J. Geurts, and Hans Kuerten, Direct and Large Eddy Simulations XI, 38, Electronic ISBN: 978-3-030-04915-7, Springer, Cham, vol. 25, pp. 285–290, DOI: `10.1007/978-3-030-04915-7_38`.

2020 Condensation-induced flow structure modifications in turbulent channel flow investigated in direct numerical simulations, *Physics of Fluids*, 32, 1, p. 015115, DOI: `10.1063/1.5128976`.

2020 Direct Numerical Simulation of Turbulent Channel Flow with Condensation Using a Cluster-Based Droplet Deposition Model, in *ERCOFTAC Series*, Springer International Publishing, pp. 111–117, DOI: `10.1007/978-3-030-42822-8_15`.

2022 Sessile condensate droplets as quasi-static wall deformations in direct numerical simulations of channel flow with condensation, *International Journal of Multiphase Flow*.

Balachandar, Sivaramakrishnan and John K. Eaton

2010 Turbulent Dispersed Multiphase Flow, *Annual Review of Fluid Mechanics*, 42, 1 (Jan. 2010), pp. 111–133, DOI: `10.1146/annurev.fluid.010908.165243`.

Belden, Otto

2010 *Schlieren Photo of a Candle Burning*, used under CC BY-NC-SA 3.0, `https://creativecommons.org/licenses/by-nc-sa/3.0/`, `https://4.bp.blogspot.com/_gCM75VJbPw0/TEykUvlnavI/AAAAAAAAAXE/n2p8d2qv_3I/s1600/Schlieren+Candle+2.JPG` (visited on 09/08/2021).

Bellec, Morgane, Adrien Toutant, and Gabriel Olalde

2017 Large Eddy Simulations of thermal boundary layer developments in a turbulent channel flow under asymmetrical heating, *Computers and Fluids*, 151 (July 2017), pp. 159–176, DOI: `10.1016/j.compfluid.2016.07.001`.

Bird, R. Byron, Warren E. Stewart, Edwin N. Lightfoot, and Daniel J. Klingenberg

2014 *Introductory Transport Phenomena*, John Wiley & Sons Inc, 784 pp., ISBN: 111877552X.

Brückner, Christian, Andreas Westhoff, and Claus Wagner

2021 Modelling of Heat Transfer for Droplet Condensation in Mixed Convective Duct Flow, in *Notes on Numerical Fluid Mechanics and Multidisciplinary Design*, Springer International Publishing, pp. 461–471, DOI: `10.1007/978-3-030-79561-0_44`.

Buaria, Dhawal, Alain Pumir, and Eberhard Bodenschatz

2020 Self-attenuation of extreme events in Navier–Stokes turbulence, *Nature Communications*, 11, 1 (Nov. 2020), DOI: `10.1038/s41467-020-19530-1`.

Buckingham, Edgar

1914 On Physically Similar Systems; Illustrations of the Use of Dimensional Equations, *Physical Review*, 4, 4 (Oct. 1914), pp. 345–376, DOI: `10.1103/PhysRev.4.345`.

Callen, Herbert

1985 *Thermodynamics and an introduction to thermostatistics*, Wiley, New York, ISBN: 9780471862567.

Chahine, Moustafa T.

1992 The hydrological cycle and its influence on climate, *Nature*, 359, 6394 (Oct. 1992), pp. 373–380, DOI: `10.1038/359373a0`.

Chan-Braun, Clemens, Manuel García-Villalba, and Markus Uhlmann

2011 Force and torque acting on particles in a transitionally rough open-channel flow, *Journal of Fluid Mechanics*, 684 (Sept. 2011), pp. 441–474, DOI: `10.1017/jfm.2011.311`.

Charette, Matthew and Walter Smith

2010 The Volume of Earth's Ocean, *Oceanography*, 23, 2 (June 2010), pp. 112–114, DOI: `10.5670/oceanog.2010.51`.

Chorin, Alexandre Joel

1968 Numerical solution of the Navier–Stokes equations, *Mathematics of Computation*, 22, 104, pp. 745–745, DOI: `10.1090/S0025-5718-1968-0242392-2`.

Coleman, Gary and Richard Sandberg

2010 A Primer on Direct Numerical Simulation of Turbulence – Methods, Procedures and Guidelines, *Technical Report AFM-09/01a* (Mar. 2010).

DIN EN 1946-2:1999-04, Wärmetechnisches Verhalten von Bauprodukten und Bauteilen

1999 *DIN EN 1946-2:1999-04, Wärmetechnisches Verhalten von Bauprodukten und Bauteilen - Technische Kriterien zur Begutachtung von Laboratorien bei der Durchführung der Messungen von Wärmeübertragungseigenschaften - Teil 2: Messung nach Verfahren mit dem Plattengerät; Deutsche Fassung EN 1946-2:1999- Technische Kriterien zur Begutachtung von Laboratorien bei der Durchführung der Messungen von Wärmeübertragungseigenschaften - Teil 2: Messung nach Verfahren mit dem Plattengerät; Deutsche Fassung EN 1946-2:1999*, DOI: `10.31030/8099321`.

Doumont, Jean-luc

2009 *Trees, maps, and theorems*, Principiæ, ISBN: 978-9081367707.

Dussan V., Elizabeth B. and Robert Tao-Ping Chow

1983 On the ability of drops or bubbles to stick to non-horizontal surfaces of solids, *Journal of Fluid Mechanics*, 137 (Dec. 1983), pp. 1–29, DOI: `10.1017/s002211208300227x`.

Eggels, Jacobus G. M., Friedemann Unger, M. H. Weiss, Jerry Westerweel, Ronald J. Adrian, R. Friedrich, and F. T. M. Nieuwstadt

1994 Fully developed turbulent pipe flow: a comparison between direct numerical simulation and experiment, *Journal of Fluid Mechanics*, 268 (June 1994), pp. 175–210, DOI: `10.1017/s002211209400131x`.

Eimann, Ferdinand, Shaofei Zheng, Christian Philipp, Tobias Fieback, and Ulrich Gross

2018 Convective dropwise condensation out of humid air inside a horizontal channel – Experimental investigation of the condensate heat transfer resistance, *International Journal of Heat and Mass Transfer*, 127 (Dec. 2018), pp. 448–464, DOI: `10.1016/j.ijheatmasstransfer.2018.08.015`.

Eldridge, R. Bruce

2014 *Parallel Plate Heat Transfer*, Lecture Notes, `http://www.cchem.berkeley.edu/cbe150a/Parallel%20Plate%20Heat%20Transfer.pdf` (visited on 03/24/2020).

Engineering ToolBox

2010 *Water - Heat of Vaporization.* `https://www.engineeringtoolbox.com/water-properties-d_1573.html` (visited on 07/21/2021).

Fefferman, Charles L.

2006 Existence and smoothness of the Navier–Stokes equation, *The millennium prize problems*, 57, 67, p. 22.

Ferrus, Lydia, Daniel Commenges, Janie Gire, and Pierre Varène

1984 Respiratory water loss as a function of ventilatory or environmental factors, *Respiration Physiology*, 56, 1 (Apr. 1984), pp. 11–20, DOI: `10.1016/0034-5687(84)90125-7`.

Ferziger, Joel H., Milovan Perić, and Robert L. Street

2020 *Computational Methods for Fluid Dynamics*, Springer International Publishing, DOI: `10.1007/978-3-319-99693-6`.

Grass, Anthony J.

1971 Structural features of turbulent flow over smooth and rough boundaries, *Journal of Fluid Mechanics*, 50, 2 (Nov. 1971), pp. 233–255, DOI: `10.1017/s0022112071002556`.

Gray, Donald D. and Aldo Giorgini

1976 The Validity of the Boussinesq Approximation for Liquids and Gases, *International Journal of Heat and Mass Transfer*, 19, 5, pp. 545–551, DOI: `10.1016/0017-9310(76)90168-X`.

Grötzbach, Günther

1983 Spatial resolution requirements for direct numerical simulation of the Rayleigh-Bénard convection, *Journal of Computational Physics*, 49, 2 (Feb. 1983), pp. 241–264, DOI: `10.1016/0021-9991(83)90125-0`.

Hammou, Zouhair Ait, Brahim Benhamou, Nicolas Galanis, and Jamel Orfi

2004 Laminar mixed convection of humid air in a vertical channel with evaporation or condensation at the wall, *International Journal of Thermal Sciences*, 43, 6 (June 2004), pp. 531–539, DOI: `10.1016/j.ijthermalsci.2003.10.010`.

Hussain, A. K. M. Fazle and William C. Reynolds

1975 Measurements in Fully Developed Turbulent Channel Flow, *Journal of Fluids Engineering*, 97, 4 (Dec. 1975), pp. 568–578, DOI: `10.1115/1.3448125`.

Jorge, Luiz Mario De Matos, Cláudio Vinicius Barbosa Monteiro, Aderson Roberto Righetto, Leonardo César de Souza, and Paulo Roberto Paraíso

2010 Heat and mass transfer during the warming of a bottle of beer, *Acta Scientiarum. Technology*, 32, 2 (July 2010), DOI: `10.4025/actascitechnol.v32i2.8273`.

Kasagi, Nobuhide and Mitsugu Nishimura

1997 Direct numerical simulation of combined forced and natural turbulent convection in a vertical plane channel, *International Journal of Heat and Fluid Flow*, 18, 1, pp. 88–99, DOI: `10.1016/S0142-727X(96)00148-8`.

Kath, Christian and Claus Wagner

2016 Highly Resolved Simulations of Turbulent Mixed Convection in a Vertical Plane Channel, in *Notes on Numerical Fluid Mechanics and Multidisciplinary Design*, Springer International Publishing, pp. 515–524, DOI: `10.1007/978-3-319-27279-5_45`.

Ketcheson, David I., Mikael Mortensen, Matteo Parsani, and Nathanael Schilling

2019 More efficient time integration for Fourier pseudospectral DNS of incompressible turbulence, *International Journal for Numerical Methods in Fluids*, 92, 2 (Oct. 2019), pp. 79–93, DOI: `10.1002/fld.4773`.

Kim, John, Parviz Moin, and Robert Moser

1987 Turbulence statistics in fully developed channel flow at low Reynolds number, *Journal of Fluid Mechanics*, 177 (Apr. 1987), pp. 133–166, DOI: `10.1017/s0022112087000892`.

Kim, Sunwoo and Kwang J. Kim

2011 Dropwise Condensation Modeling Suitable for Superhydrophobic Surfaces, *Journal of Heat Transfer*, 133, 8 (May 2011), DOI: `10.1115/1.4003742`.

Kimura, Satoshi and William Smyth

2007 Direct numerical simulation of salt sheets and turbulence in a double-diffusive shear layer, *Geophysical Research Letters*, 34, 21 (Nov. 2007), DOI: `10.1029/2007gl031935`.

Köthe, Thomas, Sebastian Herzog, and Claus Wagner

2014 Shape optimization of aircraft cabin ventilation components using adjoint CFD, in *Engineering Optimization 2014*, CRC Press, pp. 675–680, DOI: `10.1201/b17488-120`.

Krogstad, Per-Åge, Helge I. Andersson, Ole M. Bakken, and Alireza Ashrafian

2005 An experimental and numerical study of channel flow with rough walls, *Journal of Fluid Mechanics*, 530 (May 2005), pp. 327–352, DOI: `10.1017/S0022112005003824`.

Le Fevre, Edwin J. and John W. Rose

1966 A theory of heat transfer by dropwise condensation, in *International Heat Transfer Conference Digital Library*, Begel House Inc., DOI: `10.1615/ihtc3.180`.

Lorenz, Manuel

2015 Reduction of heating loads and interior window fogging in vehicles, PhD thesis, Technische Universität München, ISBN: 978-3-8439-2421-4.

Lund, Thomas S., Xiaohua Wu, and Kyle D. Squires

1998 Generation of Turbulent Inflow Data for Spatially-Developing Boundary Layer Simulations, *Journal of Computational Physics*, 140, pp. 233–258, DOI: `10.1006/jcph.1998.5882`.

Madras, Giridhar and Benjamin J. McCoy

2001 Distribution kinetics theory of Ostwald ripening, *The Journal of Chemical Physics*, 115, 14 (Oct. 2001), pp. 6699–6706, DOI: `10.1063/1.1403687`.

Manhart, Michael

2004 A zonal grid algorithm for DNS of turbulent boundary layers, *Computers & Fluids*, 33, 3 (Mar. 2004), pp. 435–461, DOI: `10.1016/s0045-7930(03)00061-6`.

Marek, Rudi and Johannes Straub

2001 Analysis of the evaporation coeffcient and the condensation coeffcient of water, *International Journal of Heat and Mass Transfer*, 44, pp. 39–53, DOI: `10.1016/S0017-9310(00)00086-7`.

Maschkio, Thorsten

2006 CFD-Simulation der Be- und Enttauungsprozesse in Kfz-Scheinwerfern, PhD thesis, Universität Paderborn, ISBN: 9783736921986.

Medici, Marie-Gabrielle, Anne Mongruel, Laurent Royon, and Daniel Beysens

2014 Edge effects on water droplet condensation, *Phys. Rev. E*, 90 (6 Dec. 2014), p. 062403, DOI: `10.1103/PhysRevE.90.062403`.

Mei Maofei, Yu Boming, Cai Jianchao, and Luo Liang

2009 A fractal analysis of dropwise condensation heat transfer, *International Journal of Heat and Mass Transfer*, 52, 21-22 (Oct. 2009), pp. 4823–4828, DOI: `10.1016/j.ijheatmasstransfer.2009.06.013`.

Newport Corporation

2020 *Introduction to Solar Radiation*, `http://www.newport.com/t/introduction-to-solar-radiation` (visited on 07/28/2020).

Oberlack, Martin, Sergio Hoyas, Stefanie V. Kraheberger, Francisco Alcántara-Ávila, and Jonathan Laux

2022 Turbulence Statistics of Arbitrary Moments of Wall-Bounded Shear Flows: A Symmetry Approach, *Physical Review Letters*, 128, 2 (Jan. 2022), p. 024502, DOI: `10.1103/physrevlett.128.024502`.

Oberli, Linda, Dean Caruso, Colin Hall, Manrico Fabretto, Peter J. Murphy, and Drew Evans

2014 Condensation and freezing of droplets on superhydrophobic surfaces, *Advances in Colloid and Interface Science*, 210 (Aug. 2014), pp. 47–57, DOI: `10.1016/j.cis.2013.10.018`.

Pope, Stephen B.

2000 *Turbulent flows*, Cambridge University Press, Cambridge New York, ISBN: 9780521598866.

Prosperetti, Andrea and Grétar Tryggvason

2007 *Computational Methods for Multiphase Flow*, ed. by Andrea Prosperetti and Grétar Tryggvason, Cambridge University Press, DOI: `10.1017/cbo9780511607486`.

Reinikainen, Leena M., Jouni J. K. Jaakkola, and Olli P. Heinonen

1991 The effect of air humidification on different symptoms in office workers — An epidemiologic study, *Environment International*, 17, 4 (Jan. 1991), pp. 243–250, DOI: `10.1016/0160-4120(91)90009-f`.

Robinson, Stephen K.

1991 Coherent Motions in the Turbulent Boundary Layer, *Annual Review of Fluid Mechanics*, 23, 1 (Jan. 1991), pp. 601–639, DOI: `10.1146/annurev.fl.23.010191.003125`.

Rose, John W.

2002 Dropwise condensation theory and experiment: A review, *Proceedings of the Institution of Mechanical Engineers, Part A: Journal of Power and Energy*, 216, 2 (Jan. 2002), pp. 115–128, DOI: `10.1243/09576500260049034`.

Russo, Emanuele, J. G. M. Kuerten, Cees W. M. van der Geld, and Bernard J. Geurts

2014 Water droplet condensation and evaporation in turbulent channel flow, *Journal of Fluid Mechanics*, 749 (May 2014), pp. 666–700, DOI: `10.1017/jfm.2014.239`.

Shishkina, Olga and Claus Wagner

2004 Stability conditions for the Leapfrog-Euler scheme with central spatial discretization of any order, *Applied Numerical Analysis & Computational Mathematics*, 1, 1 (Mar. 2004), pp. 315–326, DOI: `10.1002/anac.200310028`.

Smith, Charles R. and Steven. P. Metzler

1983 The characteristics of low-speed streaks in the near-wall region of a turbulent boundary layer, *Journal of Fluid Mechanics*, 129 (Apr. 1983), p. 27, DOI: `10.1017/s0022112083000634`.

Sundqvist, Hilding and George Veronis

1970 A simple finite-difference grid with non-constant intervals, *Tellus*, 22, 1 (Jan. 1970), pp. 26–31, DOI: `10.3402/tellusa.v22i1.10155`.

Tennekes, Henk and John L. Lumley

1972 *A First Course in Turbulence*, The MIT Press, DOI: `10.7551/mitpress/3014.001.0001`.

The OpenFOAM Foundation

2021 *www.openfoam.org*, `www.openfoam.org` (visited on 04/16/2021).

Tryggvason, Grétar, Asghar Esmaeeli, and Nabeel Al-Rawahi

2005 Direct numerical simulations of flows with phase change, *Computers & Structures*, 83, 6-7 (Feb. 2005), pp. 445–453, DOI: `10.1016/j.compstruc.2004.05.021`.

Tu, Jiyuan, Guan-Heng Yeoh, and Chaoqun Liu

2018 *Computational Fluid Dynamics A Practical Approach*, ed. by Chaoqun Liu Jiyuan Tu Guan-Heng Yeoh, Butterworth-Heinemann, DOI: `10.1016/B978-0-08-101127-0.09993-1`.

Tufte, Edward

2001 *The visual display of quantitative information*, Graphics Press, Cheshire, Conn, ISBN: 9781930824133.

Uhlmann, Markus

2008 Interface-resolved direct numerical simulation of vertical particulate channel flow in the turbulent regime, *Physics of Fluids*, 20, 053305 (May 2008), DOI: `10.1063/1.2912459`.

Versteeg, Henk Kaarle and Weeratunge Malalasekera

2007 *An Introduction to Computational Fluid Dynamics*, Second, Prentice Hall, 503 pp., ISBN: 9780131274983.

de Villiers, Eugene

2006 The Potential of Large Eddy Simulation for the Modelling of Wall Bounded Flows, PhD thesis, Imperial College London.

Vinokur, Marcel

1983 On One-Dimensional Stretching Functions for Finite-Difference Calculations, *Journal of Computational Physics*, 50, pp. 215–234, DOI: `10.1016/0021-9991(83)90065-7`.

Vinuesa, Ricardo, Azad Noorani, Adrián Lozano-Durán, George K. El Khoury, Philipp Schlatter, Paul F. Fischer, and Hassan M. Nagib

2014 Aspect ratio effects in turbulent duct flows studied through direct numerical simulation, *Journal of Turbulence*, 15, 10 (July 2014), pp. 677–706, DOI: `10.1080/14685248.2014.925623`.

Wagner, Claus

1996 *Direkte numerische Simulation turbulenter Strömungen in einer Rohrerweiterung*, VDI-Verlag, Düsseldorf.

Wagner, Claus and Rainer Friedrich

1998 On the turbulence structure in solid and permeable pipes, *International Journal of Heat and Fluid Flow*, 19, 5 (Oct. 1998), pp. 459–469, DOI: `10.1016/s0142-727x(98)10027-9`.

Wang Shutao and Lei Jiang

2007 Definition of Superhydrophobic States, *Advanced Materials*, 19, 21 (Nov. 2007), pp. 3423–3424, DOI: `10.1002/adma.200700934`.

Wetzel, Tim and Claus Wagner

2019 Buoyancy-induced effects on large-scale motions in differentially heated vertical channel flows studied in direct numerical simulations, *International Journal of Heat and Fluid Flow*, 75 (Feb. 2019), pp. 14–26, DOI: `10.1016/j.ijheatfluidflow.2018.09.005`.

Zhang Tengfei, Tian Linlin, Lin Chao-Hsin, and Wang Shugang

2012 Insulation of commercial aircraft with an air stream barrier along fuselage, *Building and Environment*, 57 (Nov. 2012), pp. 97–109, DOI: `10.1016/j.buildenv.2012.04.013`.

Zuurbier, Moniek, Gerard Hoek, Peter van den Hazel, and Bert Brunekreef

2009 Minute ventilation of cyclists, car and bus passengers: an experimental study, *Environmental Health*, 8, 1 (Oct. 2009), DOI: `10.1186/1476-069x-8-48`.